Eindhoven University of Technology

MASTER

Optimizing scintillator and fiber optic performance with Monte Carlo simulations

Vogelaar, Tom J.

Award date:
2018

Optimizing Scintillator and Fiber Optic Performance with Monte Carlo Simulations

Master Thesis

Author:
Tom Vogelaar

Supervisors:
Gerald van Hoften, Erik Bakkers

Eindhoven University of Technology
Department of Applied Physics

Thermo Fisher Scientific

February 5, 2018

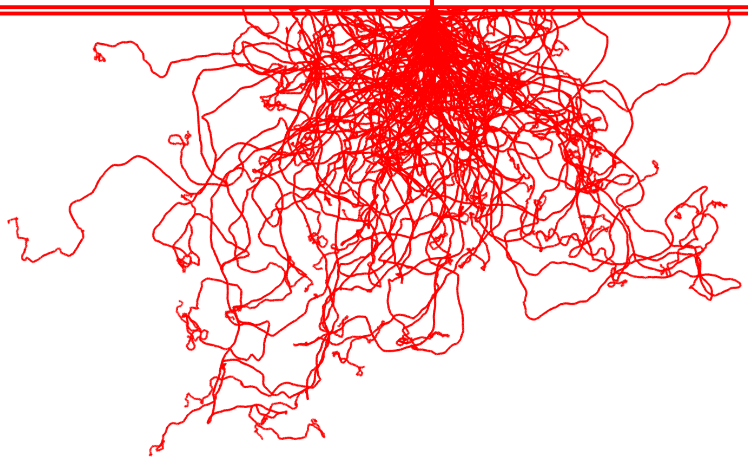

Abstract

Over the past two decades important advancements have been made in the development of electron detectors in transmission electron microscopes. The introduction of the direct electron detector had a large impact within the field and gained lots of attention. This type of detector made high resolution imaging possible at a low electron dose, which is an important requirement for cryo-TEM. However, the indirect detector has not yet reached the level of flexibility and robustness of the indirect electron detector. This is why the indirect detection camera is still interesting for various users. This raises the question whether this camera design can be further improved.

The indirect detector is based on the scintillation principle where electrons are converted in visible light which is subsequently transmitted through a fiber optic plate (FOP) and detected by a CMOS sensor. In this report the relation between the camera performance and various design parameters are studied. This is done with Monte Carlo simulation software developed by Meyer & Kirkland (1998) [1]. The most promising results have been found in the simulation of the FOP material. The FOP contains a significant fraction ($\sim 20\%$) of lead in the current detector design, the other 80% is mostly glass. Simulations have shown that omitting lead in the FOP would give a detector performance improvement of $40 - 60\%$.

During experiments, the imaging performance of six different FOP's were measured. These results gave strong indications that FOP's without lead indeed give a better imaging performance.

Simulations of the scintillator showed that the camera performance is correlated to the ratio of the atomic number and the mass density of the scintillator, Z_{scint}/ρ_{scint}. The detector performs best for a low Z_{scint}/ρ_{scint} ratio. Furthermore, simulations showed that the optimal scintillator thickness is independent of the chemical composition of the fiber optic.

Acknowledgements

I would like to thank Gerald van Hoften, my supervisor at Thermo Fisher Scientific for giving me the opportunity to do my graduation project at this company, and for his feedback and guidance during the project. I would like to thank Bart and Maarten for their valuable insights during the project meetings. Furthermore, I would like to thank Erik Bakkers for his input and feedback during the project.

Contents

Chapter 1

Introduction

1.1 Electron microscopy

On October 4th 2017 the importance of electron microscopy for science and society was underlined when the three founders of cryo electron microscopy (cryo-EM) where rewarded with the Nobel Prize for chemistry. Their work meant a break-through in high resolution imaging of organic samples. This has lead to an unprecedented growth of publications of studies that made 3D images of proteins. Cryo-EM is these days capable of resolving structures with a resolution of ~ 0.4 nm. Being able to produce images of proteins on this scale can help to understand a variety of diseases like Alzheimer.

Several innovations were essential to come to this point. One of the most important was on the field of sample preparation. In order to make an image of an organic structure like a protein, it is important to have the protein in an aquas environment. Otherwise that natural structure of the protein can get lost. This was done by dissolving the sample in a thin film of a water-like solvent. This film is placed on a grid and is rapidly frozen to prevent crystallization of the water molecules. This process is called vitrification. This sample then placed in the transmission electron microscope (TEM), that makes an image of the sample.

In the TEM, an electron source called a field-emission electron gun (FEG) generates an electron beam that is made parallel by magnetic lenses. This parallel electron beam is accelerated after which it penetrates the sample. The beam is subsequently magnified by additional magnetic lenses. This magnification can be a hundred to a million times, which allows to make images on the atomic scale. At the bottom of the TEM, the electrons are eventually detected by the camera.

Organic samples impose several requirements for the electron microscope. One of them is a restriction of the dose. If the number of electrons per area that expose the sample is too high, the radiation will damage the sample. As a result, the camera should be able to resolve images at a very low dose. The efficiency by which a camera is able to detect electrons is therefore a very important figure of merit in the development of cameras [2].

1.2 Developments in the camera

For many years a scintillator-CCD camera was the standard. This type of camera detects the electron indirectly: the scintillator converts the electrons in photons that are subsequently detected by the CCD. One of the disadvantages of indirect detection is that the electron scatters in the scintillator, causing blur in the image. As a result, more electrons were needed to realize a certain image quality, but this was not possible due to the requirements imposed by the organic sample.

Advances were made with the development of the direct detector. In this type of detector the

electron is directly detected by a CMOS sensor. This allows to gather information from single electron events. The direct detector is able to resolve details at a higher spatial resolution and is more suitable to detect at low dose. This makes direct detectors perfect for imaging organic samples. FEI (now Thermo Fisher Scientific) launched their first direct electron detector in 2011.
The direct detector is not perfect though. It rightfully gained a lot of attention and the technique has already resulted in many research publications all over the world. But it still lacks the versatility of the indirect detector, which is coupled to a CMOS sensor these days. The indirect detector is more robust and flexible in terms of dose rates and therefore is still the best option for certain users. This makes it worthwhile to study the possibilities of improving the latest indirect electron detector [3].

1.3 This study

This study aims to find possibilities to improve the current design of the indirect electron detector. This includes the scintillator and the support of the scintillator, which is the fiber optic plate. This makes the research question: Which design parameters can be changed in order to improve the performance of the indirect electron detector?
Next to finding opportunities to improve the detector, this study aims to develop a deeper understanding of the underlying physics that is involved in scintillation and electron and photon scattering.
Design aspects that could be possibly changed in order to improve the detector performance are for example the scintillator material and its thickness and the fiber optic material and its numerical aperture. These design parameters are studied using Monte Carlo simulations. A software package developed by Meyer & Kirkland (1998) is used [1]. Their model is based on the single scattering model developed by Joy (1995) [4]. In addition, a few experiments have been done to draw a comparison between simulations and experiments. In these experiments the chemical composition of various fiber optics are measured after which their performance is measured in an actual detector.
This translates to the following sub-questions:

1. How is the chemical composition of the support related to the camera performance? Changing the effective atomic number of the support has an effect on electron scattering in the support. This determines the fraction of electrons that scatter back from the support to the scintillator.
2. How is the chemical composition of the scintillator related to the camera performance? This question focuses on electron scattering in the scintillator.
3. How is the thickness of the scintillator related to the camera performance? An increased thickness of the scintillator gives the electrons more space to generate more photons. However, electrons are enabled to travel larger lateral distances inside the scintillator, increasing the size of the photon blob. This is recognized as blur in the output image. Goal is to find the optimal thickness and to study the relationship between camera performance and scintillator thickness.
4. What is the relationship between the optical properties of the fiber optic and the camera performance?
5. How is scintillator grain size and fill factor, also known as packing density, related to the camera performance?
6. How do these results compare to experimental results?

The following three chapters will introduce theoretical background information on the scintillator detector, signal and noise properties and the simulation model. Chapter five will explain the experimental methods that are used. It will also how the simulations are set up. Chapter six combines the results and the discussion of the results. Chapter seven gives the conclusions that can be drawn from the results, along with the implications for the camera design. Additional data and information can be found in the appendix.

Chapter 2

The scintillator detector

The theoretical background for the study of camera performance ranges from the working principle of scintillator detectors to the quantitative description of image quality. First the underlying physics of a scintillator detector will be described by systematically covering each of its three main parts. Then the idea of a Monte Carlo simulation will be described in order to let the reader understand why it is suited for the study of electron scattering. Then the single scattering model for electron trajectories developed by Joy (1995) will be described, followed by the extension to this model to describe the emission of photons, developed by Meyer and Kirkland (1998). At the end of this chapter, the ways to quantitatively describe image quality in terms of frequency depended signal and noise properties will be explained.

2.1 Basic principles of a scintillator detector

A scintillator detector is designed to detect a variety of particles, such as x-ray, γ-ray and electrons. It is widely used in medical applications to detect x-rays. In the case of electron microscopy, it is designed to detect electrons and convert them into a digital signal. Since this report is about electron microscopy, the detection of electrons will be used as an example to illustrate the working principle of a scintillator detector, although it is conceptually very similar to that of x-ray detection [5].

A scintillator detector consists of essentially three main parts: the scintillator, an optical element and a photo detector, see figure 2.1. In the scintillator, incoming electrons, often referred to as the primary electrons, create photons through inelastic collisions. This process is called cathodoluminescence and will be covered in more detail in the next section.

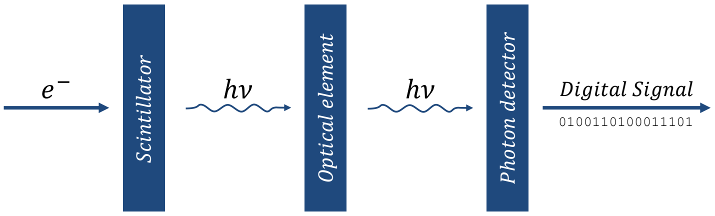

Figure 2.1: Basic working principle of a scintillator detector. Incoming particles, in this case electrons, enter the scintillator where they are converted into photons. Photons are transported through the optical element to the photon detector, which converts them into a digital signal.

These photons are transferred to the optical element. Such an element can be a certain combination of lenses and mirrors, or an array of optical fibers called a fiber optic. This optical element can serve different goals, e.g. it can be used to focus or amplify the signal. In the case of the fiber optic it is meant to shield the photon detector from electrons that might have penetrated the scintillator and could damage the detector and influence the signal.
After having traveled through the optical element, the photons reach the photon detector. Such a detector can be a charge coupled device sensor (CCD sensor) or a complimentary metal oxide semiconductor sensor (CMOS sensor). The sensor converts the photons into a digital signal, which can be interpreted by complimentary software.
This stack of components converting electrons to a digital signal, is often referred to as the camera. The subject of this study is the CETA camera which, from top to bottom, consists of a thin (8 μm) scintillator coated with an aluminum layer to prevent charge build up, a fiber optic plate (FOP) and a CMOS sensor. See figure 2.2.

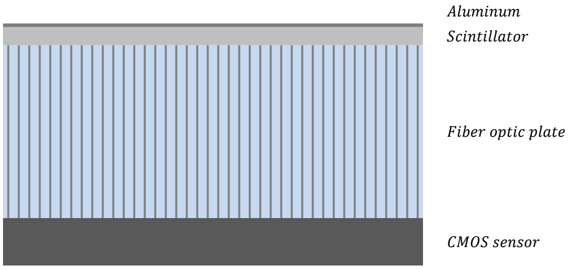

Figure 2.2: Overview of the CETA camera with from top to bottom: aluminum coating, scintillator, fiber optic plate and the CMOS sensor.

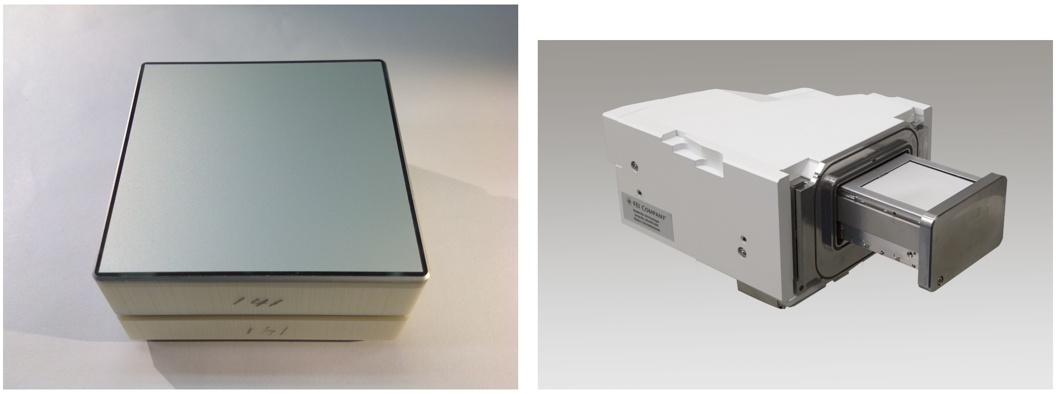

(a) A fiber optic with a scintillator coated on top of the fiber optic.

(b) The camera module. The white square is the detector area.

Figure 2.3: Pictures of the indirect detector.

2.2 Scintillator material structures

Various media can show scintillating properties: solids, gases and liquid materials. In the field of electron micropscopes, the solid scintillators are of interest. Solid scintillators can be further subcategorized in organic and inorganic crystalline media. Polymeric compounds can also show luminescence when ionizing radiation propagates through the medium [6]. For the detection of electrons as well as x-rays, inorganic scintillators are most widely used. These scintillators can be either a very fine powder or a bulky single crystal. When the grains are large, i.e. in the order of tens of micrometers, the properties of the scintillator fall in between that of a powder and a single crystal. This class of scintillators is referred to as optical ceramics. For x-ray detection, a columnar microstructure is also among the options. The various material structures can be found in figure 2.4.

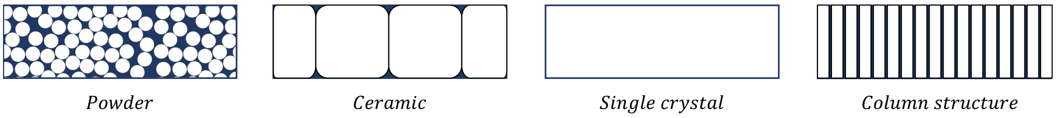

Figure 2.4: Overview of the various material structures of scintillators. White represents the scintillating material.

2.2.1 Powders

Powdered (or granulated) scintillators and single crystal scintillators are used for different applications. However, the distinction between the two is starting to extinct, since it became possible to use a single type of scintillator for different detection modes. The individual grains of a powdered scintillator, often modeled as spheres, typically have a diameter of several micrometers. The micro-grain structure introduces scattering and absorption at the grain boundary, limiting the optical path length. This decreases the scintillation yield, but improves the spatial resolution of the image. This makes scintillator powders ideal for steady state integrating mode detection [5]. In this detection mode, the sensor has a low framerate and the signal is integrated in a single image. The counterpart is counting mode, in which single events are isolated by using a high framerate.

Depending on the application, the properties of a granular scintillator can be tuned by varying the grain size, packing density and fill material. Previous studies show that for high resolution imaging a high packing density and small grain size provides the best performance. A larger grain size results in a faster imaging process, which can be a requirement for certain applications [7, 8].

2.2.2 Single crystal

Bulk scintillator is referred to as single crystal. Due to the lack of grain boundaries, photons can travel larges distances before being scattered or absorbed. As a result, single crystals have a large scintillation yield, which is an important requirement for counting mode detectors. However, since the photons have the freedom to travel large lateral distances, a single crystal scintillator has a relatively poor spatial resolution.

2.2.3 Optical ceramics

Optical ceramics emerged from the need to have an affordable alternative for single crystals, which are expensive to produce. Compressed large grains of scintilating material constitute an optical ceramic. Due to the compression, an optical ceramic achieves an overall density that is 99.9% of the density of a single crystal. The average grain size is typically 30 μm [6]. Apart from the costs to produce this type of scintillator, optical ceramics have proven to have another advantage over single crystals. Recent developments allowed to impose higher and more homogeneous dopant concentrations in the scintillator [5].

2.2.4 Columnar microstructures

A columnar scintillator screen is particularly suited for x-ray detectors. Apart from converting incoming radiation into visible photons, the scintillator and fiber optic also serve as a shield for the photon sensor. To properly shield this detector, the scintillator and fiber optic need to have sufficient stopping power. With a columnar structure, a scintillator pillar acts as a wave guide. Photons created in the scintillator are prohibited to travel from one column to the other and hence, the spatial frequency is conserved, regardless the height of the column. This allows to produce thicker scintillators that offer a higher stopping power and signal output.

2.3 Conversion mechanism in a scintillator

In this section, background information is provided to help understand what causes the scintillation effect, and how this differs in various materials. Furthermore, the relation between the electron energy and photon yield is assessed.

In a scintillator, an incoming particle excites an electron from the valence band to the conduction band, leaving behind a positively charged hole in the valence band. After a certain time the electron-hole (e-h) pair recombines, thereby emitting a photon.

When the incoming particle is a photon, that could be an x-ray or γ-ray, the process is called photo-luminescence. Depending on the photon energy, the photon excites an electron by the photo-electric effect, Compton effect or electron-positron pair production.

When the incoming particles are electrons, the process is called cathodoluminescence. High energetic, incoming electrons excite electrons in the scintillator through electron-electron (e-e) scattering.

To study the scintillation process in more detail, it is convenient to identify three stages, also displayed schematically in figure 2.5:

1. Conversion: interaction of the incoming particles with the scintillator, creating e-h pairs that migrate and thermalize towards the band gap.
2. Transport: further relaxation and transport to the luminescence center.
3. Luminescence: recombination and emission of the photon.

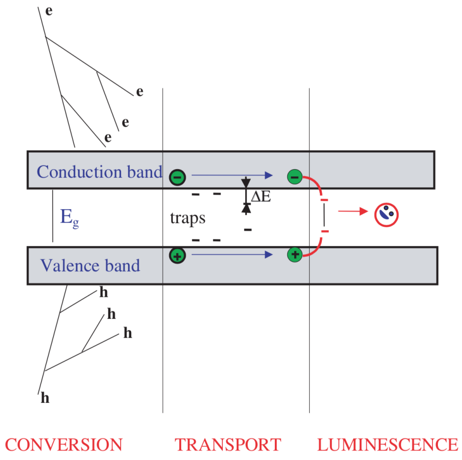

Figure 2.5: Schematic overview of the three stages of scintillation. Image retrieved from Nikl (2005) [9].

Photoluminescence and cathodoluminescence only differ in the type of particles that interacts with the scintillator. Both primary interactions result in the creation of an e-h pair and the subsequent process is identical for both types of luminescence.
Although the general concept of scintillation, as described above, is valid for every type of scintillator, the details differ from one type of material to another. This is due to the differences in band structure, as will follow soon. Here, three types of inorganic scintillators will be discussed:

1. Crystals with a narrow band gap, E_g, and a wide valence band, ΔE_v, (e.g. semiconductors).
2. Ionic compounds for which the the valence band is comparable or smaller than the band gap ($\Delta E_v \leq E_g$). Such materials have mainly covalent bonds (e.g. oxides).
3. Ionic crystals with a valence band much smaller than the band gap ($\Delta E_v \ll E_g$), typically insulating materials (e.g. fluorides and chlorides).

The two extremes, ionic crystals and semiconductors, will be discussed explicitly, while the intermediate case of ionic compounds will be mentioned briefly.
Sometimes, impurities are grown in the scintillator to introduce available states in the band gap that can temporarily capture electrons and holes, making the luminescence process more efficient. These impurities are called activators [10, 11]. Activators become increasingly important for wider bandgaps, since the bandgap corresponds to the energy of the emitted photons. For very wide bandgaps (insulators), the energy of the photons shifts towards the UV or invisible part of the spectrum, where photo detectors are usually less sensitive. Activators make the energy transitions smaller and hence the emitted photon has a lower frequency. There is an upper limit though. When the activator density becomes too high, the energy transitions become too small, and the e-h pair tends to recombine through nonradiative phonon emission [11].
Before covering the scintillation process in the different types of inorganic scintillators, some basic formulas will be introduced. Suppose an incoming particle, e.g. an electron, has energy E, and assume this energy is completely deposited in the scintillator material. One can define the following expression for the number of photons created [10]:

$$N_{ph} = N_{eh} S Q = \frac{E}{E_{eh}} S Q. \tag{2.1}$$

In this equation, N_{eh} is the number of e-h pairs created, with E_{eh} the energy needed to create such a pair. The parameter S is related to the transport and transfer efficiency of the e-h pair energy to the luminescence center. Q is the quantum efficiency of the final luminescence process, which for example can be influenced by the use of an activator.
It is convenient to define a so-called ionization efficiency:

$$Y = \frac{E_g}{E_{eh}}. \tag{2.2}$$

The parameter β is generally used in literature and is defined as the reciprocal value of the ionization efficiency. It is a measure for the yield of e-h pairs of a scintillator:

$$\beta = \frac{1}{Y}. \tag{2.3}$$

Ideally, the energy needed create an e-h pair is simply the energy of the band gap, E_g, which would result in a perfect efficiency, $Y = 1$. However, usually $E_{eh} > E_g$ and the e-h pair loses energy as the electron moves towards the bottom of the conduction band and the hole towards the top of the valence band. Because of this, the ionization efficiency is usually smaller than unity, $Y < 1$. The electron dissipates its excess energy through different loss mechanisms, creating secondary electrons (SE), Auger electrons, x-rays and phonons (heat). The nature and occurrence of each type of loss mechanism will be discussed in more detail in the next section.

Given equations 2.1 and 2.2, one can write a definition of the scintillator efficiency that incorporates every loss mechanism in the process. The scintillation efficiency is labeled ϱ, and is defined as the ratio of the energy of the photons emitted by the scintillator and the energy of the primary electron absorbed by the scintillator. Note that not every photon emitted by the scintillator actually reaches the photo detector, this will be discussed in more detail soon. The scintillator efficiency is then given by

$$\varrho = \frac{N_{ph}\langle h\nu\rangle}{E} = \frac{\langle h\nu\rangle}{E_g} YSQ, \tag{2.4}$$

with $\langle h\nu\rangle$ the average energy of the photons emitted. This formula covers the entire process. Y is related to the first stage, conversion, that describes the efficiency of the e-h pair creation and transport towards the band gap. It has been measured for various semiconductors with high precision. The second stage is covered by the parameter S, which is rather hard to determine. In this stage the e-h pair is transported to the luminescence center, often the activator. In this process, e-h pairs can be lost by nonradiative recombination, e.g. by the emission of a phonon. The quantity $1 - S$ is often referred to as the migration loss. This stage is reported to be the main source of energy loss. Once the luminescence center is reached, the process of the actual emission of the photon, stage three, is described by the quantum efficiency Q, which for many activators can be measured by direct photoexcitation, and is often close to unity [10].

2.3.1 Ionic crystals

Figure 2.6 shows the band structure of an ionic crystal, where $\Delta E_v \ll E_g$. Incident electrons excite electrons from the valence band and core levels to the conduction band, leaving holes behind. By making interband transitions, holes migrate from the core levels towards the valence band. Or equivalently: electrons, which are the majority carriers in the valence band and the core bands, fill up vacant levels (holes) that are lower in energy. During these transitions, the atom releases energy which results in the emission of x-rays or the emission of an Auger electron. This is schematically illustrated in figure 2.6.

These Auger electrons and x-rays again interact with other atoms in the scintillator, creating secondary e-h pairs, this results in an Avalanch effect. Similar wise, electrons in the conduction band excite other electrons through e-e scattering, creating new e-h pairs. The Avalanche process continues until the carriers exit the scintillator or until their energy reaches a value below the ionization threshold, E_t. For ionic crystals $E_t \approx E_g$, i.e. below E_t an electron does not have enough energy to ionize another atom, for which it needs to excite another electron by at least E_g. Above E_t an electron can create new e-h pairs through direct ionization or indirect via the creation of a plasmon. Earlier studies have indeed reported photoluminescence experiments where for an incident photon energy $h\nu > 2E_g$, the quantum yield of luminescence exceeds unity, which means an incident photon created two e-h pairs [10].
It is at $E < E_t$ where most of the energy loss occurs. At this point the electron dissipates its energy by electron-phonon scattering, effectively heating up the scintillator. This process is called thermalization and is also illustrated in figure 2.6. For ionic crystals, thermalization of holes is negligible since the valence band is very narrow compared to E_t over which the electron thermalizes.
Measurements have shown that the timescale on which e-e scattering occurs is $10^{-15} - 10^{-13}$ s. Electron-phonon scattering takes place $10^{-12} - 10^{-11}$ s after initial excitation, followed by the lifetime of the luminescence centers which is $\tau > 10^{-9}$ s. This confirms the conceptual idea that these events take place in this specific order.

2.3.2 Semiconductors

The scintillation process for semiconductors is very similar to that of ionic crystals, although a little less complicated. This is due to the fact that the valence band is much wider than the band gap, and so no interband transitions take place between core bands and the valence bands. As a consequence,

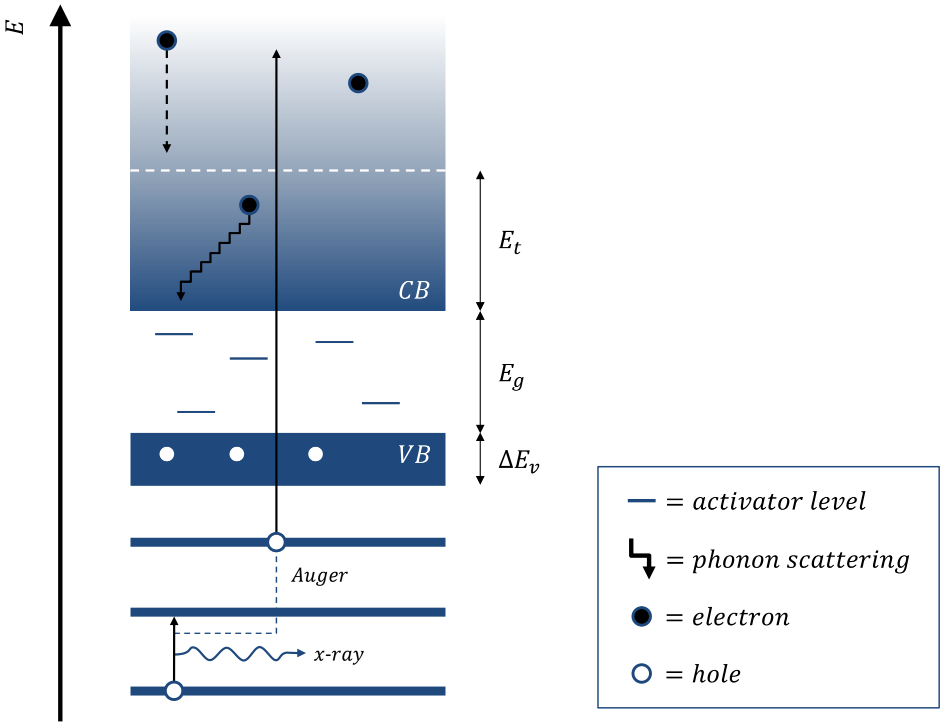

Figure 2.6: Band structure of an ionic crystal, from top to bottom: the conduction band, valence band and core bands. The energy loss mechanisms are e-e scattering and the emission of phonons, x-rays and Auger electrons.

the relaxation process of the holes is very similar to that of the electrons in the conduction band, see figure 2.7.

With a wide valence band compared to the band gap, thermalization in the valence band becomes a significant loss mechanism. Next to the ionization threshold for electrons, $E_{t(e)}$, an ionization threshold for the holes is introduced, $E_{t(h)}$.

2.3.3 Shockley and Klein model

Shockley and Klein developed a phenomenological model that describes the formation of e-h pairs in semiconductors [12]. This model turned out to be also applicable to large band gap materials like ionic crystals.

Above the threshold, carriers lose their energy either by exciting other carriers or by optical phonon emission. Secondary carriers can end up in a recombination process creating a photon. In this case the energy is not considered lost. Only the optical phonon collisions, that result in an energy penalty E_l, should be considered as actual energy loss above the threshold. Through these collisions, the carrier ends up below the energy threshold with a certain amount of kinetic energy, which is the energy involved in the thermalization process. The average amount of this kinetic energy is $\langle E_e \rangle$ and $\langle E_h \rangle$ for electrons and holes respectively.

According to this model, the energy needed to create an e-h pair can be written as

$$E_{eh} = E_g + \langle E_e \rangle + \langle E_h \rangle + E_l. \tag{2.5}$$

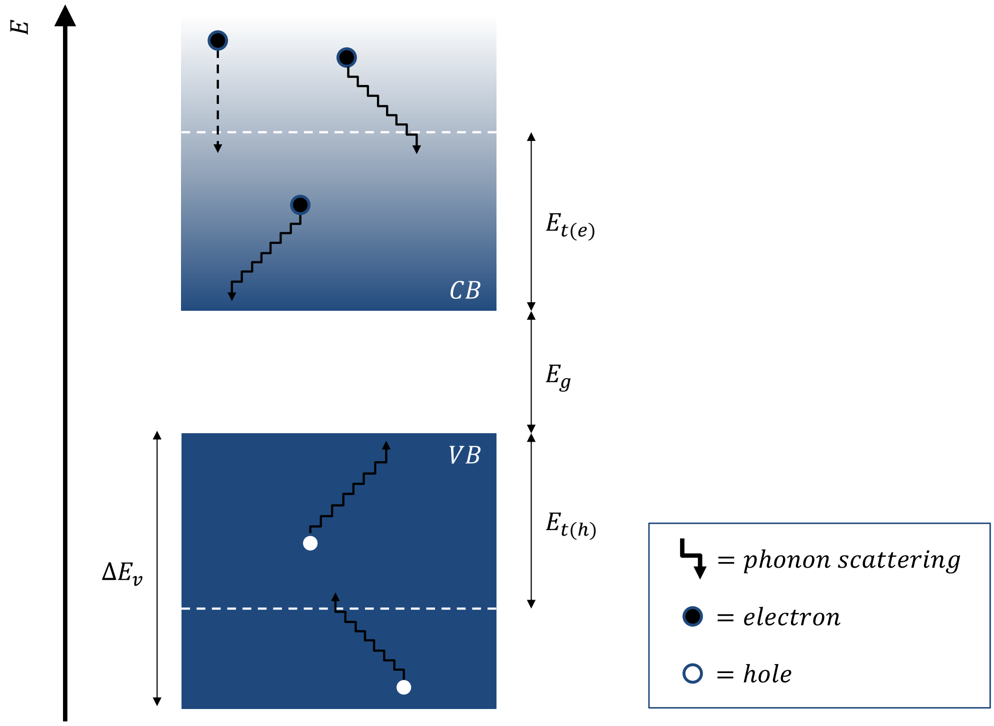

Figure 2.7: Band structure of a semiconductor. The energy loss mechanisms are e-e scattering and the emission of phonons.

Assuming the bands are parabolically shaped and the carriers are uniformly distributed over the available states, one can write the average kinetic energy in terms of the threshold energies, $\langle E_e \rangle = 0.6E_t$ and $\langle E_h \rangle = 0.6E_t$ according to Rodnyi (1995) and Shockley (1961) [10, 12]. Elango (2011) then used the principles of energy and mass conservation during the production of an e-h pair to derive

$$E_t = \frac{9E_g}{7 - m_e^*/m_h^*}, \tag{2.6}$$

where m_e^* and m_h^* are the effective masses of electrons and holes respectively [13]. For semiconductors, these effective masses are approximately equal, $m_e^* \approx m_h^*$, since the primary electron transfers its momentum equally to the secondary electron and hole. And so $E_t = 1.5E_g$, which is confirmed by experimental results [10]. With this information, equation 2.5 can be written in terms of E_g and E_l for semiconductors, since $\langle E_e \rangle + \langle E_h \rangle = 1.8E_g$ and so

$$E_{eh} = 2.8E_g + E_l. \tag{2.7}$$

In ionic crystals the valence band is very small, so the thermalization of holes can be neglected and $\langle E_h \rangle = 0$. Furthermore, in ionic crystals the momentum of the primary electron is almost completely transferred to the electron in the creation of an e-h pair, and $m_h^* \gg m_e^*$, which gives $E_t = (9/7)E_g$. Combining this with the fact that $\langle E_e \rangle = 0.6E_t$ and substitute this in equation 2.5 gives

$$E_{eh} = 1.8E_g + E_l. \tag{2.8}$$

Equations 2.7 and 2.8 show that there is a linear dependence of the energy needed to create an e-h pair on the bandgap of the material. Also, this energy does not seem to depend on the type of radiation that excites the carriers, which confirms that the process of photoluminescence and cathodoluminescence is identical after the initial excitation. These equations allow to write E_{eh} in a more general form:

$$\frac{E_{eh}}{E_g} = \frac{1}{Y} = \beta = k + K, \tag{2.9}$$

where k reflects the energy losses due to the thermalization process and K the energy loss due to the optical phonon scattering above the ionization threshold. Values for k, K and β for semiconductors have been measured with high accuracy and show good agreement with the theoretical values. E.g. a measurement of ten different semiconductors gave $k = 2.73$ and $E_l = 0.55$ eV. The energy loss due to thermalization dominates the energy loss above the ionization threshold, E_l. Measurements also show that E_l is approximately the same for all semiconductors [10]. Comparing theory and experimental data turns out to be more difficult for ionic crystals.
Given the definition of β, the scintillation efficiency as defined by 2.4 can be written as:

$$\varrho = \frac{\langle h\nu \rangle}{\beta E_g} SQ. \tag{2.10}$$

The number of photons created in the scintillator, assuming all energy is deposited in the scintillator is then given by

$$N_{ph} = \frac{E}{\beta E_g} SQ. \tag{2.11}$$

It might seem odd that the photon energy $\langle h\nu \rangle$ is not part of this equation. But $\langle h\nu \rangle$ is in fact a function of the E_g. If the scintillator is modified with for example dopants, the band gap changes. Suppose the bandgap effectively decreases, than the average energy of the emitted photons $\langle h\nu \rangle$ will decrease as well, and hence N_{ph} will increase. However the bandgap should not only be optimized to emit as many photons as possible. It should also emit photons with an energy that can be efficiently detected by the photon sensor.
The Shockley and Klein model gives for semiconductors $\beta \approx 3$, for ionic crystals $\beta \approx 2$ and for ionic compounds $2 < \beta < 3$. This difference is due to the fact that in the semiconductor the carriers thermalize in the conduction band as well as in the valence band, while in the ionic crystal only the electrons thermalize, which limits k and thus β. Measurements have shown that this model is most accurate for semiconductors, but usually overestimates β for ionic crystals. The plasmon model is proven to do a better job in predicting β, and gives $\beta < 2$ for ionic crystals [10].
In practice, one is mainly interested in the scintillator efficiency ϱ, rather than efficiency parameter of each individual loss mechanism. The scintillator efficiency is often known and can be found in literature. When the energy that the electron deposits in the scintillator is known, and the average photon energy $\langle h\nu \rangle$ can be derived from the emission spectrum, the number of emitted photons can be calculated by $N_{ph} = \varrho E / \langle h\nu \rangle$. For example, suppose a 300 keV electron loses 5 keV in a GdO_2O_2:Tb scintillator. This type of scintillator has an efficiency of $\varrho = 13\%$, and an emission peak at 540 nm, which resembles a 2.3 eV photon. In that case the scintillator emits $N_{ph} \approx 280$ photons.

2.4 Fiber optic plate

A FOP is designed to wave guide incoming photons towards the photon sensor lying underneath the FOP (see figure 2.2). It is an array of optical fibers with cladding in between the cores to separate them from one another, see figure 2.8. The reason why the fiber can act as a wave guide is because the refractive index of the core is larger than the one of the cladding, $n_{core} > n_{clad}$, such that when the incident photon has an angle larger than a critical angle θ_r relative to the normal of the interface, the photon is internally reflected at the core-cladding interface by total internal reflection. This guides the photon through the fiber.

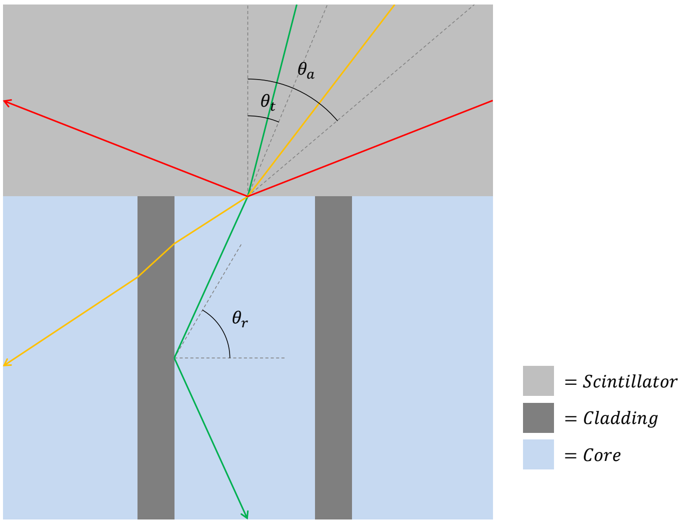

Figure 2.8: At the scintillator-FOP interface three ranges of angles can be identified: $0 < \theta < \theta_t$ at which the photons are accepted and transmitted by the FOP (green ray), $\theta_t < \theta < \theta_a$ at which the photon is accepted by the FOP but not transmitted through the optical waveguide (yellow ray) and $\theta_a < \theta < \pi$ at which the photon is reflected at the scintillator-FOP interface (red ray).

There are two critical angles for a photon at the scintillator-FOP interface, related to the indexes of refraction. The first one is the angle that determines whether the photon is reflected through total internal reflection or accepted at the scintillator-FOP interface, θ_a. See figure 2.8. This critical angle only exists when $N_{scint} > n_{core}$, but this is usually the case.
Assuming the top surface area made up by the cores of the FOP is much larger than the area of the cladding, θ_a can be calculated using Snell's law, giving:

$$\theta_a = \arcsin \frac{n_{core}}{n_{scin}}, \tag{2.12}$$

with n_{scin} the refractive index of the scintillator. The other critical angle, θ_t, determines at which angles the photon is transmitted by the FOP. For this to happen, internal reflection has to take place at the core-cladding interface. This imposes the following condition for the incident angle θ relative to the normal of the core-cladding interface: $\theta > \theta_r$. With θ_r given by

$$\theta_r = \arcsin \frac{n_{clad}}{n_{core}}. \tag{2.13}$$

The refracted angle at the scintillator-core interface is then given by $\pi/2 - \theta_r$. Using Snell's law, this results in the following equation:

$$\begin{aligned} n_{scin} \sin \theta_t &= n_{core} \sin(\pi/2 - \theta_r) \\ &= n_{core} \cos \theta_r, \end{aligned}$$

squaring both sides gives

$$\begin{aligned} n_{scin}^2 \sin^2\theta_t &= n_{core}^2 \cos^2\theta_r \\ &= n_{core}^2(1-\sin^2\theta_r) \\ &= n_{core}^2\left(1-\left(\frac{n_{clad}}{n_{core}}\right)^2\right) \\ &= n_{core}^2 - n_{clad}^2. \end{aligned}$$

So the numerical aperture of the FOP is given by

$$\text{NA} = n_{scin}\sin\theta_t = \sqrt{n_{core}^2 - n_{clad}^2}. \tag{2.14}$$

And the critical transmission angle equals

$$\theta_t = \arcsin\left(\frac{\sqrt{n_{core}^2 - n_{clad}^2}}{n_{scin}}\right). \tag{2.15}$$

Suppliers often calculate the numerical aperture of a fiber optic relative to air. In that case $\text{NA} = \sin\theta_t$, and the numerical aperture has a maximum value of 1.

The critical angles given by equations 2.12 and 2.15, allow to identify three distinct ranges of angles, see also figure 2.8. The three ranges are:

1. $0 < \theta < \theta_t$ at which the photons are accepted and transmitted by the FOP (green ray),
2. $\theta_t < \theta < \theta_a$ at which the photon is accepted by the FOP but not transmitted through the optical waveguide (yellow ray),
3. $\theta_a < \theta < \pi$ at which the photon is reflected at the scintillator-FOP interface (red ray).

Chapter 3

Signal and noise properties

To improve the performance of any type of imaging system, one has to develop ways to quantitatively describe image quality. The quanta composing the input signal diffuse through the detector and are subjected to a certain conversion efficiency. This affects the noise and the signal strength of the original signal. Ultimately, it is the ratio between the signal and the noise (signal-to-noise ratio, SNR) that determines the resolvability of an object [14].

The groundwork of the analysis of image quality was developed by Albert Rose in 1948. His theoretical model, often referred to as the Rose Model, pioneered the idea that the quality of an image is fundamentally limited by the stochastic nature of photons [15]. His model is simplistic in the sense that it treats the detector as an ideal detector. Additive noise is neglected and the absorption of the incident quanta is assumed to be perfect. In spite of these simplifications, his model is still meaningful today and useful to make estimating calculations [16]. Based on the fundamental work of Rose, the analysis of images progressed in the decades that followed. The progression that has been made can be divided in two steps.

First, one continued to treat the system as an ideal system. This allowed for the application of transfer theory, inspired by communication theory [17, 18]. In this field of science, Fourier analysis is applied to signals in the time domain, enabling analysis in the frequency domain. With transfer theory, signals in the spatial domain (images), can be analyzed in the spatial frequency domain, which lead to significant advancements in the analysis of images[17]. This approach has two main advantages. First of all, one measurement can give information of the behavior of the detector for all frequency components. This enables to predict the behavior of the detector for any object, since every object can be decomposed in sine waves of various frequencies, amplitudes and phases. Secondly, computations in the frequency domain are far less complicated than in the spatial domain. Calculations in the spatial domain require convolution products, whereas in the frequency domain these calculations are simple products.

Next, various noise contributions due to stochastic processes are included to develop a more realistic model of detectors. This lead to the most important figure of merit for imaging systems: the detective quantum efficiency (DQE).

In the following pages, a quantitative description of each of these models will be given. Starting with the original model from Rose, to transfer theory, to detective quantum efficiency.

3.1 Rose Model

The Rose model can be illustrated by the example of an object with area A and an average number of quanta per unit area $\langle n_o \rangle$. The object is surrounded by a uniform background with an average of $\langle n_b \rangle$ quanta per unit area, see figure 3.1a.

In literature, various definitions of contrast can be found depending on the application. In general the contrast is given by the maximum deviation from the average signal divided by the average signal. The Michelson contrast is commonly used for periodic signals where the bright and dark fringes compose an equal area, see figure 3.1b. It is defined as the amplitude of the periodic signal, $(\langle n_o \rangle - \langle n_b \rangle)/2$ divided by the average signal, $(\langle n_o \rangle + \langle n_b \rangle)/2$. This results in the following definition:

$$C_M = \frac{\langle n_o \rangle - \langle n_b \rangle}{\langle n_o \rangle + \langle n_b \rangle}. \tag{3.1}$$

The Michelson contrast is also known as the visibility or modulation [19].
The Weber contrast is commonly used for small objects in a large background, as in figure 3.1a. Since in this case the background dominates the image, the average signal is equal to the background signal. The maximum deviation from this average is $\langle n_o \rangle - \langle n_b \rangle$. From this follows the definition:

$$C_W = \frac{\langle n_o \rangle - \langle n_b \rangle}{\langle n_b \rangle}. \tag{3.2}$$

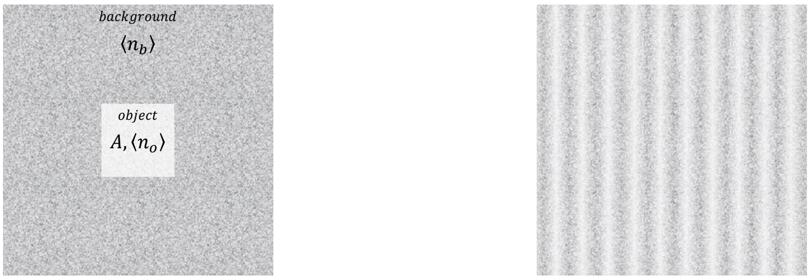

(a) A square object with area A surrounded by background quanta. The object is relatively small which allows to approximate the average signal as the background signal. This configuration is used to derive Rose's signal-to-noise ratio.

(b) An image that contains a periodic signal. At the brightest points the quantum density is $\langle n_o \rangle$ and at the darkest points $\langle n_b \rangle$. Defining contrast for this image leads to the Michelson contrast, also known as modulation or visibility.

Figure 3.1: Two different images both with their own definition of contrast. Image (a) results in the Weber contrast and image (b) in the Michelson contrast.

To derive an expression for the signal-to-noise ratio, signal and noise have to be defined. Rose chose the incremental change in image quanta composing the object to be the signal, $A(\langle n_o \rangle - \langle n_b \rangle)$. The noise is defined as the standard deviation in the number of background quanta in an area equal to that of the object, A. Rose makes the important assumption that the background noise is uncorrelated, allowing to use Poisson statistics. The standard deviation is then given by $\sigma_b = \sqrt{A\langle n_b \rangle}$. This results in the following expression for the signal-to-noise ratio [16]:

$$\mathrm{SNR}_{Rose} = \frac{A(\langle n_o \rangle - \langle n_b \rangle)}{\sqrt{A\langle n_b \rangle}} = C_W\sqrt{A\langle n_b \rangle} = C_W\sqrt{N_b}, \tag{3.3}$$

with N_b the number of background quanta in an area A. According to Rose, this ratio should be at least five in order for the human eye to detect the object. He was therefore the first one to relate dose to image quality [14].
One should note that Rose implicitly makes and important assumption here. The model does not make a distinction between the variance in quanta in the object area with or without the presence of the object. When the object is present, the noise term should read $\sigma = \sqrt{A\langle n_o \rangle}$. As a result, the Rose model can only be used when $\langle n_b \rangle \approx \langle n_o \rangle$, i.e. in the low contrast limit [16]. This allows to write equation 3.3 in terms of number of quanta, N_q, rather than background or object quanta specifically. This gives $\mathrm{SNR}_{Rose} = C_W\sqrt{N_q}$. This formula illuminates an important consequence of the statistic nature of image quanta. As the number of quanta composing the image increases,

so does the signal strength and the noise. However, the noise increases more slowly, as it increases with $\sqrt{N_q}$. And hence, the SNR increases for increasing N_q.
As mentioned, Rose assumed the background noise to be uncorrelated, allowing to use Poisson statistics. This assumption is actually true for ideal detectors, but in realistic detectors there is a certain amount of correlation in the noise due to the fact that the noise is transferred by the imaging system. It is this assumption that imposes the largest limitation on the use of the Rose model [17]. The model therefore received appropriate extensions in successive studies to incorporate correlated noise.

3.2 Transfer theory

The way in which the camera system changes the signal can be described by transfer theory. This approach assumes an ideal and noise free system. This results in an operator that describes the relation between the input and the output of the system. Knowing this operator, one can reproduce the original signal by applying the inverse operator to the output.
Transfer theory can be used if and only if the system can be approximated as a linear shift-invariant (LSI) system. The well known equivalent in the time domain is the linear time-invariant (LTI) system.

Linearity

If the operator T defines the output of the system for a certain input, a system is said to be linear if the output for a weighed sum of inputs is equal to the weighed sum of outputs for separate inputs, i.e.

$$T[\alpha x_1 + \beta x_2] = \alpha T[x_1] + \beta T[x_2]. \tag{3.4}$$

Shift-invariance

A system is shift-invariant if the output for a shifted input is simply the output of the original input, shifted by the same translation. In other words, the operator T is position invariant. In mathematical terms the property reads

$$y(x) = T[x] \longleftrightarrow y(x-a) = T[x-a]. \tag{3.5}$$

It will soon become evident why both properties are relevant.

3.2.1 Point spread function

When the operator T defines the output of the system for a certain input, the impulse response is given by

$$h(x,y) = T[\delta(x,y)]. \tag{3.6}$$

Shift-invariance allows to write

$$h(x-\xi, y-\eta) = T[\delta(x-\xi, y-\eta)]. \tag{3.7}$$

One of the most important features of an LSI system is that the output can be expressed in terms of the impulse response and the input. In order to do so, the input, $f(x,y)$, has to be written in terms of the delta function:

$$f(x,y) = \iint_{-\infty}^{\infty} f(\xi,\eta)\delta(x-\xi, y-\eta)\mathrm{d}\xi\mathrm{d}\eta. \tag{3.8}$$

This expression is only allowed when $f(x,y)$ obeys compact support, i.e. $f(x,y) \to 0$ for $(x,y) \to \pm\infty$. The output, $g(x,y)$, of an operator T can now be written as

$$g(x,y) = T[f(x,y)] = T\left[\iint_{-\infty}^{\infty} f(\xi,\eta)\delta(x-\xi,y-\eta)\mathrm{d}\xi\mathrm{d}\eta\right]. \tag{3.9}$$

Since T is a linear operator, it can be brought inside the integral. Furthermore, T only works on (x,y), and $f(\xi,\eta)$ can be taken outside the operator. This results in

$$g(x,y) = \iint_{-\infty}^{\infty} f(\xi,\eta)T\left[\delta(x-\xi,y-\eta)\right]\mathrm{d}\xi\mathrm{d}\eta, \tag{3.10}$$

where $T\left[\delta(x-\xi,y-\eta)\right]$ is equal to the shifted impulse response of the system (equation 3.7). Finally, the output can be written in terms of the input and the impulse response:

$$g(x,y) = \iint_{-\infty}^{\infty} f(\xi,\eta)h(x-\xi,y-\eta)\mathrm{d}\xi\mathrm{d}\eta, \tag{3.11}$$

which is simply the two dimensional convolution product of the input and the impulse response,

$$g(x,y) = f(x,y) ** h(x,y). \tag{3.12}$$

In the analysis of images, the point spread function (PSF) is defined as the normalized impulse response:

$$\mathrm{PSF}(x,y) = \frac{1}{\Lambda}h(x,y), \tag{3.13}$$

where Λ is the gain of the imaging system, defined as

$$\Lambda = \iint_{-\infty}^{\infty} h(\xi,\eta)\mathrm{d}\xi\mathrm{d}\eta. \tag{3.14}$$

The normalization implies

$$\iint_{-\infty}^{\infty} \mathrm{PSF}(\xi,\eta)\mathrm{d}\xi\mathrm{d}\eta = 1. \tag{3.15}$$

And hence, the output image of a system is given by [18]

$$g(x,y) = \Lambda\left(f(x,y) ** \mathrm{PSF}(x,y)\right). \tag{3.16}$$

The physical picture of the PSF can be understood by considering a beam of electrons entering the scintillator at a certain position (x_0,y_0). This is the input signal. The detected photons are then located at various positions, spread around the original input position (x_0,y_0). This is the output, which apart from a factor Λ is the point spread function. See also figure 3.2.

One should note that the factor $1/\Lambda$ in equation 3.13 is not always explicitly mentioned in literature, and there does not seem to be a strict convention about whether to include this normalization factor in the PSF. The user is free to incorporate the normalization further down the analysis.

3.2.2 Line spread function

The one-dimensional counterpart of the PSF is the line spread function (LSF), which can be achieved by taking one of the two dimensions constant, e.g. the y-direction. The output image of a one-dimensional input is then given by the convolution of the input and the LSF:

$$g(x) = \Lambda\int_{-\infty}^{\infty} f(x-\xi)\mathrm{LSF}(\xi)\mathrm{d}\xi, \tag{3.17}$$

where the LSF is nothing more than the PSF integrated over the y-direction:

$$\mathrm{LSF} = \int_{-\infty}^{\infty} \mathrm{PSF}(x,y)\mathrm{d}y. \tag{3.18}$$

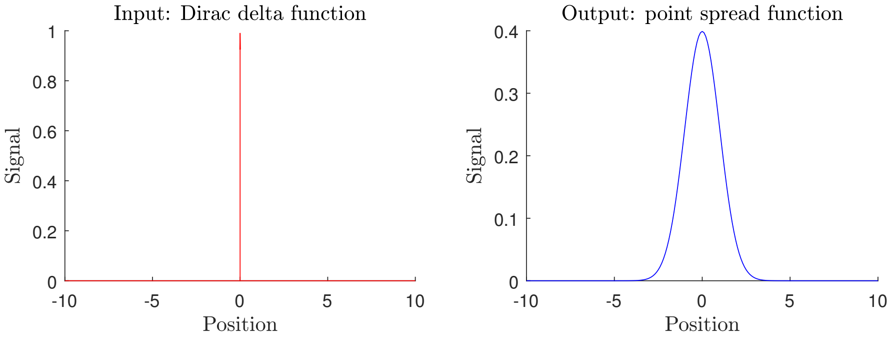

Figure 3.2: The point spread function (right) is defined as the normalized response of the imaging system to an impuls, i.e. a delta function.

3.2.3 Modulation transfer function

The Fourier transform of the convolution of two functions, is simply the product of the Fourier transforms of those functions. For more information on the Fourier transform and convolution theory, see appendix A.1. This allows to write the Fourier transform of equation 3.16:

$$\frac{1}{\Lambda}\hat{g}(u,v) = \mathcal{F}\{f(x,y) ** \mathrm{PSF}(x,y)\} = \hat{f}(u,v)\mathrm{MTF}(u,v), \tag{3.19}$$

where the hat denotes the Fourier transform of a function. (u, v) are the spatial frequency components in the x- and y-direction respectively. MTF is the modulation transfer function, which will be defined as the Fourier transform of the point spread function. It gives the fraction of modulation (equation 3.1) that is transferred by the system at a particular frequency.

Formally, the Fourier transform of the PSF is defined as the optical transfer function, OSF(u, v), which is the product of the MTF and the phase transfer function, PTF(u, v). The OSF is complex valued with MTF$(u, v) = |\mathrm{OTF}(u, v)|$ its absolute value and PTF$(u, v) = \phi_{\mathrm{OTF}}(u, v)$ its phase angle. However, a camera system does not give a phase shift, and only the MTF is of interest. In addition, the OTF is real valued for all u and v, since the PSF is even, i.e. PSF$(x, y) =$ PSF$(-x, -y)$. This allows to write the MTF as

$$\mathrm{MTF}(u,v) = \widehat{\mathrm{PSF}}(u,v). \tag{3.20}$$

The modulation transfer function is defined as the ratio of the output and input signal in reciprocal space, normalized with respect to the gain [1]. By definition, the modulation transfer function is equal to one at zero frequency, MTF$(0, 0) = 1$. In practice, often a rotational average is taken to express the MTF in one dimension.

Usually in transfer theory the transfer function is simply the Fourier transform of the impulse response, and the transfer function gives the frequency dependent fraction of the original signal that is transferred. However, in imaging it is the contrast relative to the total amount of detected light that determines the image quality, which is why the PSF and MTF are normalized functions with respect to the gain of the system.

With an ideal camera system, an input signal would not be affected by the system. This would mean that for a delta function as an input signal, the system would give the same delta function as output. This would yield a MTF that is equal to unity at every frequency, i.e. every detail is completely transferred by the system. In reality, the MTF tends to zero at high frequencies, this means that the smallest details are lost by the camera system, which is the same as saying that the contrast goes to zero at those frequencies.

3.3 Quantifying system performance

3.3.1 Noise power spectrum

An important assumption within Rose's model is that the noise is uncorrelated. In that case, noise can simply be described with a single parameter, the standard deviation, σ. However, imaging systems often do introduce correlated noise. As a result, the standard deviation does not provide all the information about the nature of the noise. For example, both images in figure 3.3 have the same σ, while they obviously have different textures. To quantify these textures, the autocovariance of the image has to be determined. The autocovariance of the image gives information about the periodic density fluctuations in the image. These periodic fluctuations can have different frequencies, which will be shown by the Fourier transform of the autocovariance, the noise power spectrum (NPS). The NPS is also commonly known as the Wiener spectrum. The remainder of this section will be devoted to the derivation of the NPS, based on the calculations of Cunningham (1999) and Saleh (1991) [17, 21].

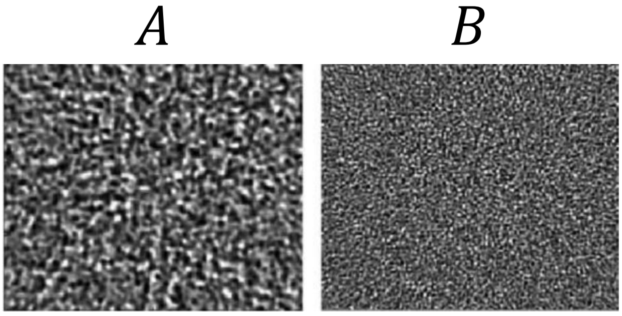

Figure 3.3: Figures A and B both have the same standard deviation, σ, although they have different textures. Image retrieved from: *http://www.ctug.org.uk/index.html*

The density fluctuation at a given position (x, y) is defined as the deviation relative to the expected value at that position, $\Delta n(x, y) = n(x, y) - \langle n(x, y)\rangle$. It has units of one over unit area, m^{-2}. Formally, one should refer to a sampling function that samples the actual distribution $n(x, y)$. For simplicity, this step will be omitted, since the analysis shown here will not suffer from this simplification. The average autocovariance is then given by

$$G(\xi, \eta) = \langle \Delta n(x + \xi, y + \eta)\Delta n(x, y)\rangle \,. \tag{3.21}$$

To continue from here, a few important conditions have to be fulfilled. First of all, the system has to be stationary. This means that the expected values of the variables have to be shift invariant. The instant values may fluctuate, but the average has to be constant throughout space. Secondly, the system should be ergodic. This means that the ensemble average, determined by many images (or an infinitely large image), is equal to the average of a finite sized single image. The first condition is usually fulfilled, particularly in low contrast images. Ergodicity is rather hard to prove, but most important systems are approximately ergodic [17].

For periodic or random variables, the expected value does not converge, which for example implies for the autocovariance of a periodic variable $x(t)$:

$$\left\langle [x(t)]^2 \right\rangle = \int_{-\infty}^{+\infty} [x(t)]^2 \mathrm{d}t \;\rightarrow\; \infty. \tag{3.22}$$

Because of this, approximating truncated integrals have to be used, which is justified by the ergodic nature of the system.

Based on the assumptions mentioned above, equation 3.21 can be written as

$$G(\xi,\eta) = \lim_{X,Y\to\infty} \frac{1}{2X}\frac{1}{2Y}\int_{-X}^{+X}\int_{-Y}^{+Y} \Delta n(x+\xi, y+\eta)\Delta n(x,y)\mathrm{d}x\mathrm{d}y. \tag{3.23}$$

For $(\xi,\eta) = (0,0)$, the autocovariance function is simply equal to the average variance of the quanta distribution:

$$G(0,0) = \left\langle |\Delta n(x,y)|^2 \right\rangle = \sigma^2. \tag{3.24}$$

Now, a different approach is used to calculate the NPS. The result will turn out to be equivalent to the Fourier transform of the autocovariance function defined by equation 3.21. To do so, the Fourier transform of the density fluctuation is taken:

$$\widehat{\Delta n}(u,v) = \iint_{-\infty}^{+\infty} \Delta n(x,y)\exp\left[-i2\pi(ux+vy)\right]\mathrm{d}x\mathrm{d}y. \tag{3.25}$$

However, as mentioned before, this integral goes to infinity, and it has to be approximated by a truncated Fourier transform over an area of $2X \times 2Y$:

$$\widehat{\Delta n}_{XY}(u,v) = \int_{-X}^{+X}\int_{-Y}^{+Y} \Delta n(x,y)\exp\left[-i2\pi(ux+vy)\right]\mathrm{d}x\mathrm{d}y. \tag{3.26}$$

The noise spectrum is now given by $\left\langle \left|\widehat{\Delta n}_{XY}(u,v)\right|^2 \right\rangle$. This spectrum and the one given by equation 3.26 are dimensionless. The NPS is given by the noise spectrum per unit area. As a result, the NPS has the same dimensions as $\Delta n(x,y)$.

The word power in this context refers to the science of photonics, where power is defined as energy per unit time. In photonics, the NPS equivalent is the power spectral density, which is the energy spectral density per unit time.

To finalize the truncated approximation, the limit $X, Y \to \infty$ is taken. This gives the following expression for NPS:

$$\mathrm{NPS}(u,v) = \lim_{X,Y\to\infty} \left\langle \frac{1}{2X}\frac{1}{2Y}\left|\int_{-X}^{+X}\int_{-Y}^{+Y} \Delta n(x,y)\exp\left[-i2\pi(ux+vy)\right]\mathrm{d}x\mathrm{d}y\right|^2 \right\rangle, \tag{3.27}$$

with units of m^{-2}. The NPS gives the variance per spatial frequency squared (squared since the system is two dimensional). This means that $\mathrm{NPS}(u,v)\mathrm{d}u\mathrm{d}v$ gives the average variance of the components with frequencies between (u,v) and $(u+\mathrm{d}u, v+\mathrm{d}v)$. Given this property the following relation can be derived:

$$\sigma^2 = \iint_{-\infty}^{+\infty} \mathrm{NPS}(u,v)\mathrm{d}u\mathrm{d}v, \tag{3.28}$$

with units of m^{-4}. This result is also obtained when applying Parseval's theorem (see appendix A.2).

When the noise is uniformly distributed and uncorrelated, the NPS is constant with respect to frequency and the variance given by equation 3.28 is then equal to the variance defined by Rose. Although one should pay attention to the details when making the comparison with the Rose model. In this section, the variance refers to the variance in the quantum density, while Rose derived an expression for the variance of the absolute number of particles in a certain area A. For convenience, this variance will now be referred to as σ_N, and the variance in quantum density will be denoted as σ_n. The connection between the two, given that the system is stationary, is $\sigma_N = A\sigma_n$, which follows from the definition of the variance:

$$\begin{aligned}\sigma_n^2 &= \left\langle (n - \langle n\rangle)^2 \right\rangle \\ &= \left\langle (N/A - \langle N/A\rangle)^2 \right\rangle \\ &= (1/A)^2 \left\langle (N - \langle N\rangle)^2 \right\rangle \\ &= (1/A)^2 \sigma_N^2.\end{aligned}$$

So far, the theoretical case is considered in which frequencies can be infinitely large. However, in reality the frequency is limited by the sample frequency. Suppose the sample frequency is $1/a_x$ and $1/a_y$ in the x- and y-direction respectively, such that the sample area is $a_x a_y = A$. When the noise is uniformly distributed and uncorrelated, i.e. white noise, the NPS is constant with respect to frequency. According to equation 3.28, the variance in the quantum density is then equal to the NPS times the entire frequency range in both dimensions:

$$\sigma_n^2 = \iint_{-\infty}^{+\infty} \text{NPS}(u,v)\text{d}u\text{d}v = \text{NPS} \int_0^{1/a_x} \int_0^{1/a_y} \text{d}u\text{d}v \tag{3.29}$$

$$= \text{NPS}\frac{1}{a_x}\frac{1}{a_y} = \frac{\text{NPS}}{A}, \tag{3.30}$$

which, according to the derivation on the previous page, is equal to σ_N^2/A^2. According to Rose's model, $\sigma_N^2 = N$ for uncorrelated quanta. Using this property and multiplying equation 3.30 by A gives

$$\text{NPS} = \frac{\sigma_N^2}{A} = \frac{N}{A} = n. \tag{3.31}$$

So for uncorrelated quanta, the NPS is equal to the quantum density, which is constant throughout the image. Since the input signal in an imaging device is often uncorrelated, one can use $\text{NPS}_{in} = n$.

Finally, a connection between the NPS and the autocovariance, $G(\xi,\eta)$, can be made. According to the Wiener-Khinchin theorem, NPS(u,v) and $G(\xi,\eta)$ form a Fourier transform pair. Thus their relation is given by

$$\text{NPS}(u,v) = \iint_{-\infty}^{+\infty} G(\xi,\eta)\exp\left[-i2\pi(u\xi + v\eta)\right]\text{d}\xi\text{d}\eta. \tag{3.32}$$

Equation 3.27 and 3.32 are in fact equivalent [20].

3.3.2 Noise equivalent quanta

The noise equivalent quanta, NEQ(u,v), is another way to describe image quality. It gives the number of input quanta needed to realize a specific SNR(u,v) if the detector where an ideal detector. In other words, NEQ(u,v) is the absolute minimum number of input quanta needed to establish a certain SNR(u,v). A high NEQ(u,v) means a high SNR(u,v), and thus a high quality image.

For an ideal detector, the Rose model is valid. This allows to write $\text{SNR}(u,v) = \sqrt{\text{NEQ}(u,v)}$, since within Rose's model $\text{SNR}_{Rose} = \sqrt{N}$. The signal of the output image is the average number of output quanta per unit area, $\bar{g}$, times the MTF(u,v). The output noise is given by the square root of the NPS(u,v). Hence

$$\text{NEQ}(u,v) = \text{SNR}^2(u,v) = \frac{\bar{g}^2\text{MTF}^2(u,v)}{\text{NPS}(u,v)} = \frac{\bar{q}^2\Lambda^2\text{MTF}^2(u,v)}{\text{NPS}(u,v)}, \tag{3.33}$$

where Λ is the gain that relates the density in output quanta to the density in input quanta, q [17, 22].

3.3.3 Detective quantum efficiency

The NEQ provides a way to describe the quality of an image. However, it does not give any information about the performance of the detector. This is where the detective quantum efficiency, DQE(u,v), comes in. The DQE(u,v) is the ratio between the number of quanta an image is ideally worth if the detector were ideal, NEQ(u,v), and the number of input quanta the image has actually cost, $\bar{q}$. Using equation 3.33, this gives

$$\text{DQE}(u,v) = \frac{\text{NEQ}(u,v)}{\bar{q}} = \frac{\bar{q}\Lambda^2\text{MTF}^2(u,v)}{\text{NPS}(u,v)}. \tag{3.34}$$

Where $0 \leq \text{DQE}(u,v) \leq 1$. The DQE is a quantitative measure to what extend the detector approaches an ideal detector. When $\text{DQE}(u,v) = 1$, the detector behaves as an ideal detector where the only noise contribution is due to Poison noise.
Another way of looking at it is saying the DQE describes how efficiently the detector uses the input quanta. Say an ideal detector uses NEQ quanta to establish a certain image quality. A non-ideal detector uses N quanta to provide the same image quality. The efficiency by which the non-ideal detector uses its photons is $\text{NEQ}/N = \text{DQE}$. Hence, if $\text{DQE} = 0.5$, the non-ideal detector needs twice the amount of input quanta to provide the same image quality as an ideal detector.
Another common expression for the DQE can be derived by realizing that if the input quanta are Poison distributed, the relation $\text{SNR}_{in}^2 = \bar{q}$ holds. And since the NEQ is the SNR_{out}^2, the DQE can be written as [22]

$$\text{DQE}(u,v) = \frac{\text{SNR}_{out}^2}{\text{SNR}_{in}^2}. \tag{3.35}$$

3.4 Sampling theory

3.4.1 Shannon's sampling theorem

Another technique that image processing adopted from signal processing is sampling theory. Shannon's sampling theory quantifies the minimum sampling frequency, and is applicable to signals with a finite bandwidth, i.e. with a maximum frequency component. Suppose the bandwidth of the signal is ω_b. Shannon's sampling theory then states that the sample frequency should be at least $\omega_s > 2\omega_b$, in order to be able to fully reconstruct the original signal. This critical value is called the Nyquist frequency. When the sampling frequency is lower than two times the bandwidth, high resolution information is lost. This is due to overlapping in the periodic spectrum of the sampled signal. This is called aliasing [23].
CMOS and CCD sensors are digital sampling devices. Each pixel bins the number of photons that enter the pixel, and effectively samples the original image in pixels of size a. Image features smaller than two times the size of a pixel cannot be detected or even cause aliasing. The pixels effectively impose a low-pass filter that results in additional blurring.
The pixels in a sensor are squares with length a and area a^2. Figure 3.4 shows the cross section of two adjacent pixels.

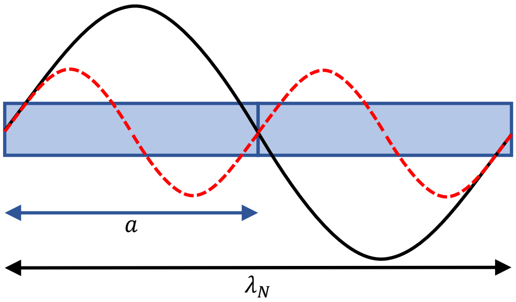

Figure 3.4: Two adjacent pixels, each of size a, and a signal (black curve) with wavelength λ_N. Higher frequencies, such as the red dotted curve, cannot be detected by the sensor due to the finite pixel size.

A signal of wavelength $\lambda_N = 2a$ is the highest frequency component that can be detected by a sensor with pixel size a. Higher frequencies, such as the red dotted signal with $\lambda = a$, can no longer be detected by the sensor. This introduces the following Nyquist frequency

$$f_N = \frac{1}{2a}. \tag{3.36}$$

Chapter 4

Simulating camera performance

The model that is used to simulate the camera performance under various conditions can be divided in two steps. In the first step, the interaction of the electron with the scintillator and the FOP is modeled. This is done with the single scattering model that allows to simulate the electron trajectory through the specimen while it loses energy through inelastic collisions. The theoretical framework for this step was developed by Joy (1995) [4].

In the second step, the behavior of the photons that are emitted through the inelastic collisions are modeled. The resulting data is used to calculate the figures of merit that are of interest. This approach was developed by Meyer and Kirkland (1998) [1].

At the heart of each simulation step lies the Monte Carlo method. First, the conceptual idea behind the Monte Carlo method will be briefly explained.

4.1 Monte Carlo simulation technique

The Monte Carlo Method is a statistical technique first published by Metropolis and Ulam in 1949 [24]. It is used to model the behavior of a large sample by making use of random sampling. This sample could be an ensemble of particles, but the technique is also used in social sciences where the sample could be the population of a country.

The idea behind the technique is the following. Suppose a game of chance is played with a probability P of having success. When the game is played N times of which X times the result was successful, the ratio X/N is an estimation of P. In this example the game of chance is the physical problem at hand. The stochastic nature of the problem is simulated by random sampling. The randomness is introduced by generating a uniformly distributed random number, usually between 0 and 1.

In the context of electron scattering the Monte Carlo method could be used in the following way. When the probability of the next scatter event being elastic or inelastic is P_e and P_i respectively, such that their sum yields unity. Then at each scatter event a random number R is generated. When $R < P_e$, the scatter event is elastic, and it is inelastic otherwise. If the simulation is repeated a sufficient number of times, the elastic/inelastic scatter ratio will approach P_e/P_i.

4.2 Electrons

4.2.1 Single scattering model

The interaction of electrons with the solid is described by the single scattering model [4]. This model is based on two assumptions.

The first assumption is that the electron trajectory is solely determined by elastic scattering events.

Elastic scatter events are Coulomb interactions between the electron and the positively charged nuclei of the solid or the negatively charged electrons orbiting the nuclei. These interactions cause a scattering angle typically between 5^{o} and 180^{o}, depending on the screened Rutherford cross section. Inelastic scatter events, like inner shell ionization, cause a deflection with a magnitude of the order of $\Delta E/E$, where ΔE is the energy lost during the inelastic scatter event, and E the energy of the electron. For example, when a $E = 100$ keV electron loses $\Delta E = 15$ eV through an inelastic collision, its deflection is $15/10^5$ radians, which is approximately 0.01^{o}. This illustrates that it is reasonable to assume that inelastic scattering events can be neglected when calculating the electron trajectory, in particular when $\Delta E \ll E$.

The second assumption involves the energy loss of the electron. The electron loses its energy through mechanisms that can be either continuous, like Bremsstrahlung, or discrete, like ionization. The single scattering model approximates these energy loss mechanisms by a single continuous energy loss equation, the Bethe equation. Instead of calculating each individual inelastic scatter event, the Bethe equation is used to approximate this behavior with continuous energy loss along the electron trajectory.

Elastic collisions

To calculate the electron trajectory, only the elastic scatter events have to be considered. The geometry is shown in figure 4.1, it is chosen such that the positive Z-axis points into the scintillator, with the XY-plane parallel to the scintillator surface. Directional cosines are abbreviated as cx, cy and cz. For example, cx is the cosine of the angle between the X-axis and the vector pointing from scatter event P_{n-1} to P_n.

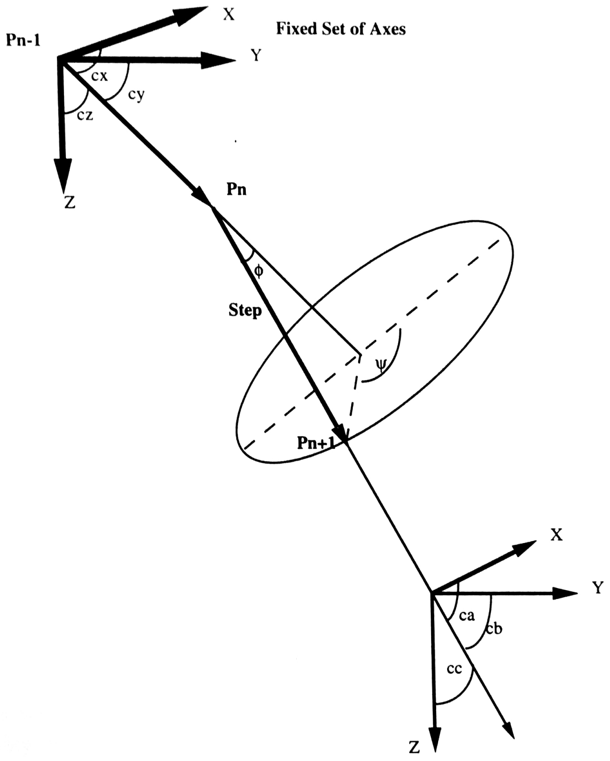

Figure 4.1: Geometry of the single scattering model. Image retrieved from Joy (1995) [4].

Suppose an electron reaches scatter event P_n after it was scattered at P_{n-1}. The question that has to be answered by the simulation is where scatter event P_{n+1} will be. To answer this question, three parameters have to be calculated: the step length, s, the polar scattering angle, ϕ, and the azimuthal scattering angle, ψ. The scattering angles are used to derive the directional cosines.

The step length is random in nature, since the scattering itself is a Poison process. However, for a given electron energy, the mean free path between two successive elastic scatter events is a material property. This mean free path, λ, can be used to determine the distribution of step lengths. The mean free path depends on the screened Rutherford cross section, σ_E, and is given by

$$\sigma_E = 5.21 \times 10^{-21} \frac{Z^2}{E^2} \frac{4\pi}{\alpha(1+\alpha)} \left(\frac{E+511}{E+1024} \right)^2 \qquad \mathrm{cm}^2/\mathrm{atom}, \tag{4.1}$$

where Z is the atomic number, E is the electron energy in keV and α the screening factor that accounts for the screening effect of the electrons orbiting the nucleus. The analytic expression for the screening factor reads

$$\alpha = 3.4 \times 10^{-3} \frac{Z^{0.67}}{E}. \tag{4.2}$$

The mean free path is then given by

$$\lambda = \frac{A}{\rho \sigma_E N_A} = \frac{1}{n \sigma_E} \qquad \mathrm{cm}, \tag{4.3}$$

where A is the atomic mass, ρ the mass density in g/cm^3 and N_A Avogadro's number. n is the particle density in number of particles per unit volume and is given by $n = \rho N_A / A$. Equation 4.1 in combination with equation 4.3 show that the number of scattering events increase with Z and ρ, while high electron energies result in a long mean free path. To give an example, an electron penetrating a Gd_2O_2S sample at 300 keV has a mean free path of a few hundreds of nanometers, while it is only a few tenths of nanometers at 10 keV.

The elastic scattering of electrons is a Poison process, and the distance or time between Poison events is typically exponentially distributed. The probability that an electron travels a distance s before an elastic scatter event takes place is given by

$$p(s) = \exp\left(-\frac{s}{\lambda}\right). \tag{4.4}$$

The goal is now to generate a random distance such that after many iterations, the distribution of distances approaches $p(s)$. This can be done by generating a random number R between 0 and 1 and solving the following equation

$$R = \frac{\int_0^s \exp(-s/\lambda)\mathrm{d}s}{\int_0^\infty \exp(-s/\lambda)\mathrm{d}s} = 1 - \exp(-s/\lambda). \tag{4.5}$$

This results in

$$s = -\lambda \ln(1-R) = -\lambda \ln(R). \tag{4.6}$$

The last expression is valid since if R is a random number between 0 and 1, so is $1-R$, which allows to make the substitution $1 - R \rightarrow R$.

A similar expression for the polar scattering angle can be derived by considering the differential form of the Rutherford cross section:

$$\sigma' = \frac{\mathrm{d}\sigma}{\mathrm{d}\Omega} = 5.21 \times 10^{-21} \frac{Z^2}{E^2} \left(\frac{E+511}{E+1024} \right)^2 \left(\sin^2(\phi/2) + \alpha \right)^{-2} \tag{4.7}$$

A scattering angle can be obtained by solving

$$R = \int_\Omega \frac{\sigma'(\phi)}{\sigma_E} \mathrm{d}\Omega, \tag{4.8}$$

which results in

$$\cos\phi = 1 - \frac{2\alpha R}{(1+\alpha-R)}. \tag{4.9}$$

Where the resulting scattering angle satisfies the condition $0 \leq \phi \leq \pi$. The distribution of angles generated by equation 4.9 matches the one obtained experimentally [4].
The azimuthal scattering angle is isotropically distributed. Therefore, it can be simply generated by the relation

$$\psi = 2\pi R. \tag{4.10}$$

With s, ϕ and ψ given by equation 4.6, 4.9 and 4.10 respectively, all the relevant parameters are at hand to calculate the position of P_{n+1}. The position of P_n is defined by the coordinates (x, y, z). The directional cosines that define the direction of the step towards P_{n+1} are labeled ca, cb and cc. See figure 4.1. The position of P_{n+1} is defined by the coordinates (xn, yn, zn). These coordinates are given by

$$xn = x + s \cdot ca \tag{4.11}$$
$$yn = y + s \cdot cb \tag{4.12}$$
$$zn = z + s \cdot cc. \tag{4.13}$$

To keep the frame of reference fixed, the directional cosines at P_{n+1} are relative to the X-, Y- and Z-axis of the previous step P_n. To make this translation, the directional cosines cx, cy and cz are needed to define ca, cb and cc. Their derivation can be found in Myklebust (1976) [25]. The resulting relations are

$$ca = cx\cos\phi + V_1V_3 + cyV_2V_4 \tag{4.14}$$
$$cb = cy\cos\phi + V_4(czV_1 - cxV_2) \tag{4.15}$$
$$cc = cz\cos\phi + V_2V_3 - cyV_1V_4, \tag{4.16}$$

where the parameters V are given by

$$V_1 = \frac{1}{\sqrt{1+(cx/cz)^2}}\sin\phi \tag{4.17}$$
$$V_2 = -\frac{(cx/cz)}{\sqrt{1+(cx/cz)^2}}\sin\phi \tag{4.18}$$
$$V_3 = \cos\psi \tag{4.19}$$
$$V_4 = \sin\psi. \tag{4.20}$$

The frame of reference can remain fixed throughout the simulation by substituting (cx, cy, cz) by (ca, cb, cc) at the end of each iteration.

Inelastic collisions

An electron can lose its energy through a large variety of mechanisms, both continuous like electrostatic drag, and discrete like the ionization of an atom. The single scattering model approximates the energy loss by a continuous energy loss as a function of displacement. The rate at which the electron loses its energy is given by the differential $\mathrm{d}E/\rho\mathrm{d}s$ and is known as the stopping power. It is often written as $\mathrm{d}E/\mathrm{d}S$ with $S = \rho s$. However, this notation will be omitted since the letter S is already used for the transport efficiency coefficient, introduced in section 2.3. The stopping power is given by the modified Bethe equation, suggested by Joy and Luo (1989) [26], and is usually written as

$$\frac{\mathrm{d}E}{\mathrm{d}s} = -7.85 \times 10^4 \frac{\rho Z}{AE} \ln\left(\frac{1.166(E+0.85J)}{J}\right) \text{ (keV/cm)}. \tag{4.21}$$

Where Z is the atomic number, A the atomic weight, E the electron energy and J the mean ionization potential given by

$$J = \left[9.76Z + \frac{58.5}{Z^{0.19}} \right] 10^{-3} \text{ (keV)}. \tag{4.22}$$

In the original Monte Carlo program written by Joy (1995), the mean ionization potential for compounds is approximated by using a weighed average value for Z. For example, Z for a compound AB_2 is approximated by $Z_{av} = (Z_A + 2Z_B)/3$.
Joy and Luo (1989) slightly modified the original Bethe equation because it was inaccurate at low energies ($E < 5$ keV), with their adjustment the equation remains valid at low energies, and converges to the original Bethe equation at high energies.

Simulation scheme

The first step into the sample will be at the angle of incidence, which is the angle relative to the normal of the sample surface. The electron trajectory can now be determined by the following simulation scheme:

1. Calculate initial penetration depth with equation 4.3 and 4.6

   Repeat the following steps:

2. Determine the electron energy at the start of the step, E_n
3. Determine the initial coordinates of this step, (x, y, z)
4. Find the directional cosines cx, cy and cz of the previous step, relative to the axes
5. Calculate the mean free path λ_n for this electron energy with equation 4.3
6. Using this mean free path, generate a step length s_n using equation 4.6
7. Generate the scattering angles, ϕ_n, ψ_n, using equations 4.9 and 4.10
8. Calculate the coordinates (xn, yn, zn) of the end position of the step with equations 4.11, 4.12 and 4.13
9. Calculate the stopping power $(\mathrm{d}E/\mathrm{d}s)_n$ for this electron energy using equation 4.21
10. Compute the electron energy at the end of the step with $E_{n+1} = E_n - s_n(\mathrm{d}E/\mathrm{d}s)_n$
11. Reset coordinates, directional cosines and energy: $(x, y, z) = (xn, yn, zn)$, $cx = ca$, $cy = cb$, $cz = cc$, $E_n = E_{n+1}$

    When the electron energy is larger than the energy threshold and it did not leave the sample
    Return to step 2
    Else
    End

4.3 Photons

4.3.1 Emission

In section 2.3.3 an equation for the number of photons was derived, $N_{ph} = (ESQ)/(\beta E_g)$. This equation gives the number of photons emitted in the scintillator (not the ones actually reaching the detector), given that all the electron energy E is deposited in the material. However, in the Monte Carlo program, one would like to know how many electrons are emitted along a step length s between two elastic scattering events. This is given by

$$n_{ph} = \frac{SQ}{\beta E_g} \frac{\mathrm{d}E}{\mathrm{d}s} s = \frac{\varrho}{E_{ph}} \frac{\mathrm{d}E}{\mathrm{d}s} s. \tag{4.23}$$

Where $(\mathrm{d}E/\mathrm{d}s)s$ is the amount of energy that the electron lost due to inelastic scattering while traveling a step length s. It can be calculated using the expression for the stopping power given by equation 4.21. A plot of the modified Bethe equation, shown in figure 4.2, shows an important property of the luminescence process. The stopping power is significantly higher at low electron energies. Since the efficiency by which the electron energy is used to emit photons is held constant, the conclusion can be drawn that according to this model, most photons are emitted at the tail of an electron trajectory where its energy is the lowest.

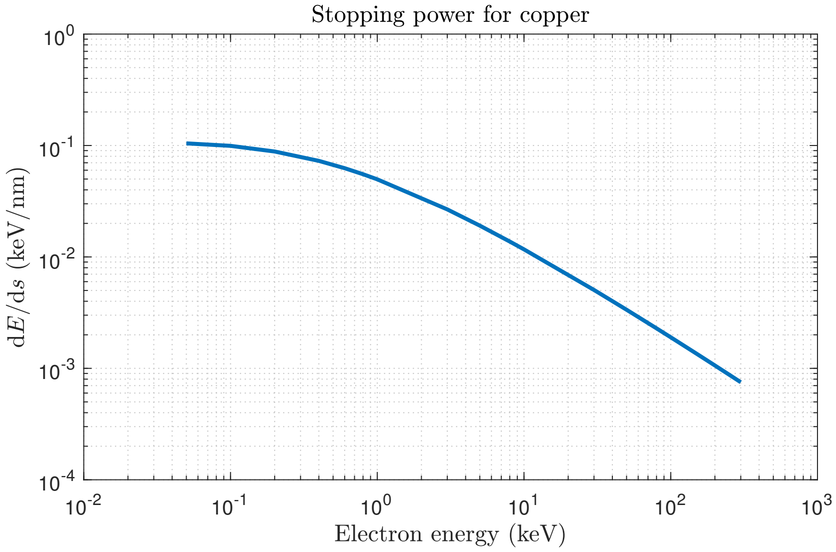

Figure 4.2: Plot of the modified Bethe equation by Joy and Luo (1989) [26] for copper.

To get an exact solution for equation 4.23, one would have to solve the differential equation 4.21 to find $E(s)$, substitute this in equation 4.23 and integrate along the step s over infinitesimal steps $\mathrm{d}s$. This is computationally very demanding and is likely to slow down the simulation significantly. The alternative is to compute E, the energy that is left of the primary electron, and the stopping power $(\mathrm{d}E)/(\rho \mathrm{d}s)$ at every iteration (i.e. every step), and assume it to be constant along the step. This is a good approximation when the step length is very small, which is the case in the simulation. This assumption is readily implemented in the simulation scheme for the electron trajectory, described in the previous section.

The original Monte Carlo program developed by Joy (1995) solely simulated the electron behavior, as described by the single scattering model. Meyer and Kirkland (1998) extended the model to include the emission of photons [1]. They treated the emission of photons as a stochastic process that is Poisson distributed, similar to the process of inelastic scattering events. To generate a random number of emitted photons, the value given by equation 4.23 is used as the mean number of photons, $\overline{n}$, emitted over a step length s. The probability that n photons are emitted during a step of length s is then given by

$$p(n) = \frac{\overline{n}^n}{n!}\exp(-\overline{n}). \tag{4.24}$$

Where $\overline{n}$ is calculated at every step, since it varies with the length of the step and the energy of the electron prior to the step. Given the distribution and the mean, a random number of Poisson distributed photons can be calculated for every step. With this addition the MC-scheme for the emission of photons can be defined. For simplicity, the steps defining the exact trajectory of the electron in terms of ϕ and ψ are left out. Those were defined in the previous section. The MC-program can be constructed by combining the electron and photon simulation scheme, which is rather straightforward. The photon scheme reads:

1. Get E_n from the previous step, which equals the starting energy for the current step, and use to calculate $(\mathrm{d}E/\mathrm{d}s)_n$
2. Calculate the mean free path for this step, λ_n
3. With λ_n, calculate the step length, s_n
4. With E_n, $(\mathrm{d}E/\mathrm{d}s)_n$ and s_n, calculate $\overline{n}_n$
5. Calculate the number of photons emitted along the step, n_n
6. Assign the photon emissions to random locations on the trajectory of the step
7. The resulting energy is calculated, which is an input parameter for the next step: $E_{n+1} = E_n - s_n(\mathrm{d}E/\mathrm{d}s)_n$
8. Set $E_n = E_{n+1}$ and return to step 1.

The photons are emitted isotropically at a certain angle α with respect to the z-axis. It depends on α relative to a critical angle θ_a whether the photon is accepted or reflected by the fiber optic. Note that accepted does not necessarily mean it is also transmitted by the FOP, see section 2.4. The probability of being emitted inside the acceptance aperture of the FOP-scintillator interface is $p(\alpha < \theta_a) = p_1$ and the probability of being emitted at an angle outside the acceptance aperture is $p(\alpha > \theta_a) = p_2 = 1 - p_1$. See figure 4.3. Details of the various possibilities for α will be discussed in the next section.

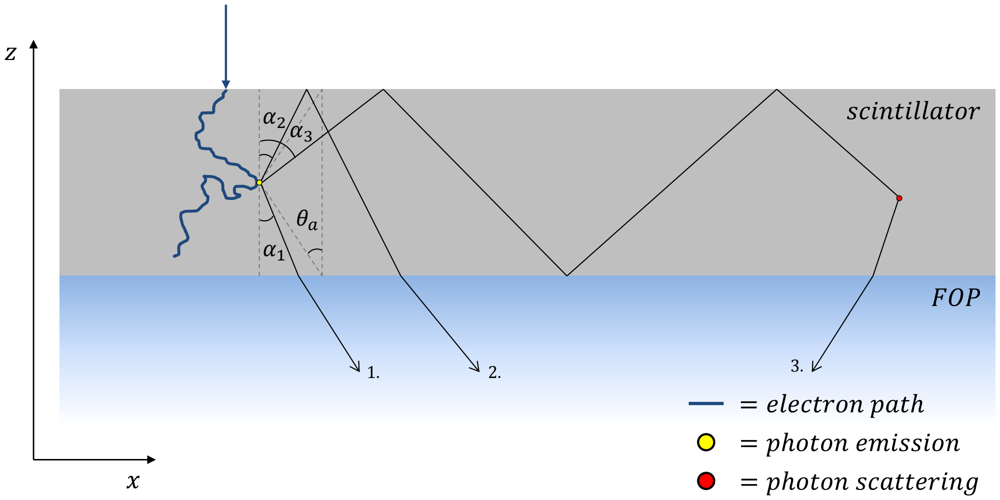

Figure 4.3: Graphical representation of the emission possibilities of a photon in the scintillator, which is (1.) straight acceptance by the fiber optic ($\alpha_1 < \theta_a$), (2.) reflection at the upper surface ($\alpha_2 < \theta_a$) or (3.) reflection at both surfaces until the photon is scattered ($\alpha_3 > \theta_a$).

The probability p_1 is defined as the solid angle fraction of the acceptance aperture. The solid angle of the acceptance cone with apex angle $2\theta_a$ is defined as the area A of the spherical cap that is formed by the intersection of the cone and the unit sphere. See figure 4.4. Hence, the probability equals the area of the spherical cap divided by the total surface area of the unit sphere.

The area A can be calculated by the following integral:

$$A = \int_0^{2\pi} \int_0^{\theta_a} \sin\theta \mathrm{d}\theta \mathrm{d}\psi = 2\pi(1 - \cos\theta_a). \tag{4.25}$$

If the photon is emitted towards the upper surface of the scintillator with an angle $\alpha < \theta_a$ relative to the z-axis, it is reflected at the upper surface and subsequently accepted by the lower surface (ray 2 in figure 4.3). As a consequence, the effective solid angle is $2A = 4\pi(1 - \cos\theta_a)$. This makes the acceptance and reflection probability respectively:

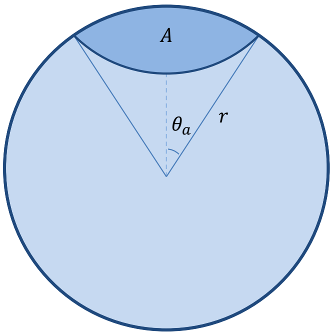

Figure 4.4: The solid angle of a cone with apex angle $2\theta_a$ and $r = 1$ is the area A of the spherical cap.

$$p_1 = 2A/4\pi = 1 - \cos\theta_a \tag{4.26}$$

$$p_2 = \cos\theta_a. \tag{4.27}$$

The fraction of the accepted photons that is actually transmitted through the FOP wave guide is given by the ratio of the solid angle of the transmission cone with semi-angle θ_t and the solid angle of the acceptance cone with semi-angle θ_a:

$$\frac{A_t}{A_a} = \frac{1 - \cos\theta_t}{1 - \cos\theta_a}. \tag{4.28}$$

4.3.2 Scattering

In their extension of the original MC-program, Meyer and Kirkland (1998) modeled the photon to emit in three possible ways, each shown in figure 4.3. Either the photon is emitted at an angle $\alpha_1 < \theta_a$ and is directly accepted by the fiber optic, ray 1. Or the photon is emitted towards the top surface of the scintillator at an angle $\alpha_2 < \theta_a$, is reflected at the top surface and subsequently accepted by the fiber optic, ray 2. Or the photon is emitted at an angle $\alpha_3 > \theta_a$ an gets trapped in the scintillator wave guide until it gets scattered at an angle $\alpha < \theta_a$.
This model makes two important assumptions. First, the model assumes the top surface of the scintillator to be reflective, although the reflection ratio can be manually chosen in the program. Secondly, it assumes that photon scattering is sufficiently rare such that the model only accounts for scattering of photons that are trapped in the wave guide and thus travel a long distance in the scintillator. The probability of a photon scattering n times, is given by $p(n) = p_1 p_2^n$. The ratio of photons that are accepted by the fiber optic with and without scattering, f_s, is one of the input parameters of the MC-program, and is given by

$$f_s = \frac{p(0 < n < \infty)}{p(n = 0)} = \frac{\sum_{n=1}^{\infty} p_1 p_2^n}{p_1} = \sum_{n=1}^{\infty} p_2^n = \frac{p_2}{1 - p_2}. \tag{4.29}$$

The fraction of photons that is scattered diffuse before accepted by the FOP are displaced by a lateral distance d relative to the position where the photon was emitted. d is exponentially distributed with mean $\overline{d}$, a user definable parameter.

4.4 Calculating figures of merit

This section gives the equations used by the MC-software to calculate the DQE. The equations and its derivations are provided by papers written by Meyer and Kirkland [1, 27].
Let μ be the label of a specific electron trajectory along which photons are emitted that reach the focal plane at a certain position. All possible trajectories compose the probability space M. The probability of a trajectory μ is given by $\mathrm{d}\mu$.
The number of photons per unit area in the focal plane at position (x, y) is given by $g_\mu(x, y)$. The Fourier transform is $\hat{g}_\mu(u, v)$, where (u, v) are the spatial frequency components in the (x, y) directions respectively.
The probability density that an electron hits the scintillator is proportional to its wave function squared:

$$p(x,y) \propto |\Psi(x,y)|^2, \tag{4.30}$$

such that the probability that an electron hits the scintillator in a infinitesimal but finite area $\mathrm{d}A$ centered at (x, y), is $p(x, y)\mathrm{d}A$. The total output signal at (x, y) is the sum of the photons reaching that position integrated over the probability space of all possible trajectories. The total output signal is written as $I_{ph}(x, y)$, its Fourier transform, $\hat{I}_{ph}(u, v)$, is a random variable with an expected value $E(u, v)$ and a variance $V(u, v)$. The expected value is used to describe the output signal of the system, while the variance describes the noise. Their expressions can be derived in the following way. When an electron enters the scintillator at position (x, y), after which it scatters its way through the scintillator along a trajectory μ, its contribution to the output spectrum is

$$\Delta\hat{I}_{ph}(u,v) = \exp\left[-2\pi i(ux+vy)\right]\hat{g}_\mu(u,v). \tag{4.31}$$

The contribution of an infinitesimal scintillator area $\mathrm{d}A$ to the expected value and variance of the output spectrum, integrated over all possible trajectories, is written as

$$\begin{aligned}
\mathrm{d}E(u,v) &= (1-p(x,y)\mathrm{d}A)\cdot 0 + p(x,y)\mathrm{d}A\int \exp\left[-2\pi i(ux+vy)\right]\hat{g}_\mu(u,v)\mathrm{d}\mu \\
&= p(x,y)\exp\left[-2\pi i(ux+vy)\right]\int \hat{g}_\mu(u,v)\mathrm{d}\mu\mathrm{d}A \\
\mathrm{d}V(u,v) &= (1-p(x,y)\mathrm{d}A)\cdot|0-\mathrm{d}E(u,v)|^2 \\
&\qquad + p(x,y)\mathrm{d}A\int \left|\exp\left[-2\pi i(ux+vy)\right]\hat{g}_\mu(u,v) - \mathrm{d}E(u,v)\right|^2\mathrm{d}\mu \\
&= p(x,y)\int |\hat{g}_\mu(u,v)|^2\mathrm{d}\mu\mathrm{d}A + \mathcal{O}(\mathrm{d}A^2).
\end{aligned}$$

Both the expected value and the variance are additive, which allows to integrate over the complete scintillator area. This results in the following expressions:

$$E(u,v) = \hat{p}(u,v)\int \hat{g}_\mu(u,v)\mathrm{d}\mu \tag{4.32}$$

$$V(u,v) = \hat{p}(0,0)\int |\hat{g}_\mu(u,v)|^2\mathrm{d}\mu. \tag{4.33}$$

The MTF is given by the ratio between the output and the input image in spatial frequency space, with a normalization factor such that $\mathrm{MTF}(0, 0) = 1$. The normalization factor is the reciprocal value of the gain, as described in section 3.2.3. The output signal is the expectation value of $\hat{I}_{ph}(u, v)$ given by equation 4.32. The input signal is $\hat{p}(u, v)$ and the normalization factor $1/\int \hat{g}_\mu(0, 0)\mathrm{d}\mu$. This gives

$$\mathrm{MTF}(u,v) = \frac{\int \hat{g}_\mu(u,v)\mathrm{d}\mu}{\int \hat{g}_\mu(0,0)\mathrm{d}\mu}. \tag{4.34}$$

So far, signal and Poison noise originating from the electrons are considered to be treated equally by the scintillator. In literature, many models are based on this assumption, like the model developed by De Ruijter in 1995 [28]. However, the assumption that the MTF applies to both signal and noise transfer has been proven to be over simplistic [1]. In practice, this often lead to a discrepancy between MTF corrected experimental results and simulation, since the MTF used to correct the results was obtained by a noise method, resulting in an over optimistic MTF. Because of this, a transfer function particularly for noise needs to be defined, the noise transfer function, NTF.

An analytic expression for the NTF can be derived by defining a transfer function through the noise method, i.e. equally exposing the scintillator surface to electrons such that the input signal has a constant variance with respect to spatial frequency. To define the noise transfer, one has to compare the input and output variance. Technically, the noise is defined as the standard deviation, thus to calculate the output variance, the input variance has to be multiplied by the NTF squared. Similar to the MTF, the NTF is defined as the square root of the ratio between the input and output variance, normalized at zero frequency. This can be written as

$$V_{out}(u,v) = [\mathrm{NTF}(u,v)]^2 V_{in}(u,v)\frac{V_{out}(0,0)}{V_{in}(0,0)}, \tag{4.35}$$

such that $\mathrm{NTF}(0,0) = 1$. Suppose the detector is ideal, this would yield $\hat{g}_\mu(u,v) = 1$ since every frequency component is perfectly transferred. Using equation 4.33, this gives $V_{out} = \hat{p}(0,0)$. Since for an ideal detector $V_{out} = V_{in}$, the following relation holds too: $V_{in} = \hat{p}(0,0)$. And since any definition of input noise or signal is independent of the type detector, whether it is ideal or not, $V_{in}(u,v) = V_{in}(0,0) = \hat{p}(0,0)$ can be used as a general expression, given that the input noise is merely Poison noise. This leads to

$$\mathrm{NTF}(u,v) = \sqrt{\frac{V_{out}(u,v)}{V_{out}(0,0)}}. \tag{4.36}$$

Again using equation 4.33, this can be written as

$$\mathrm{NTF}(u,v) = \sqrt{\frac{\int |\hat{g}_\mu(u,v)|^2 \mathrm{d}\mu}{\int |\hat{g}_\mu(0,0)|^2 \mathrm{d}\mu}}. \tag{4.37}$$

In section 3.3.3 the following relation was derived under the condition that the input quanta are Poison distributed: $\mathrm{DQE}(u,v) = (\mathrm{SNR}_{out}(u,v)/\mathrm{SNR}_{in}(u,v))^2$. The output signal squared is simply $(E(u,v))^2$, the output noise squared is $V(u,v)$, which gives $\mathrm{SNR}^2_{out}(u,v) = (E(u,v))^2/V(u,v)$. Where $E(u,v)$ and $V(u,v)$ are given by equation 4.32 and 4.33 respectively. $\mathrm{SNR}^2_{in}(u,v)$ can be derived by again treating the detector as ideal detector, giving $\hat{g}_\mu(u,v) = 1$. This gives $E(u,v) = \hat{p}(u,v)$ and $V(u,v) = \hat{p}(0,0)$, which makes $\mathrm{SNR}^2_{out}(u,v) = (\hat{p}(u,v))^2/\hat{p}(0,0)$. This expression holds for $\mathrm{SNR}^2_{in}(u,v)$ since for an ideal detector $\mathrm{SNR}^2_{in}(u,v) = \mathrm{SNR}^2_{out}(u,v)$. This leads to the following expression for the DQE of a realistic detector

$$\mathrm{DQE}(u,v) = \frac{\mathrm{SNR}^2_{out}}{\mathrm{SNR}^2_{in}} = \frac{\left|\int \hat{g}_\mu(u,v)\mathrm{d}\mu\right|^2}{\int |\hat{g}_\mu(u,v)|^2 \mathrm{d}\mu}. \tag{4.38}$$

Given the expressions for the MTF and the NTF (equation 4.34 and 4.37), the DQE can be rewritten in the following way

$$\mathrm{DQE}(u,v) = \mathrm{DQE}(0,0)\left(\frac{\mathrm{MTF}(u,v)}{\mathrm{NTF}(u,v)}\right)^2, \tag{4.39}$$

where $\mathrm{DQE}(0,0)$ is given by [29, 30]

$$\mathrm{DQE}(0,0) = \frac{\left|\int \hat{g}_\mu(0,0)\mathrm{d}\mu\right|^2}{\int |\hat{g}_\mu(0,0)|^2 \mathrm{d}\mu} = \frac{1}{1 + \frac{\mathrm{variance}(\Lambda)}{\mathrm{mean}(\Lambda)^2}}. \tag{4.40}$$

Where $\Lambda = \int \hat{g}_\mu(0,0)\mathrm{d}\mu$ is the gain.
Equation 4.39 shows that the DQE, as calculated by the MC-software, is the product of a frequency independent factor and a frequency dependent factor. The frequency independent factor, DQE$(0,0)$, depends solely on the average gain in photons per electron, and the variance in the gain. The factor DQE$(0,0)$ is caused by the stochastic nature of the amplification mechanism. If the detector is ideal and the gain is high, DQE$(0,0) \approx 1$ for $\Lambda \gg 1$. This is because in an ideal detector the only noise source is Poison noise, and in that case DQE$(0,0) = \Lambda/(\Lambda+1)$.
The frequency dependent factor is the ratio of MTF and NTF squared. Intrinsically to their transfer nature, MTF $\leq$ NTF. Since if the signal is perfectly transferred, so is the noise. Likewise, if the input signal is amplified, so is the noise in the input signal [30]. NTF can be larger than MTF due to additional noise contributions in the imaging system like electron and photon scattering.
Knowing that the DQE(u,v) is composed of a frequency independent part and a frequency dependent part can help to interpret certain results. For example, it could be that the shape of various DQE curves is very similar, but they differ in magnitude. Then this is probably due to the scaling of DQE$(0,0)$, and the physical explanation is ought to be found in the gain and the variance in the gain.

Chapter 5

Experimental methods

In this section the simulation and experimental methods will be described. The theoretical model behind the simulations was described in the theory section. The goal of these simulations is to make comparisons between various detector designs, and see how the detector performance (DQE) relates to a certain parameter, e.g. thickness. The goal is not to provide absolute numbers, but rather a direction in which improvements can be found. This section describes which parameters are varied and which are held constant to study certain relationships and how these parameters are determined and calculated.

The simulation results ask for further statistical analysis to fully understand their implications. E.g. the quality of a fit should be quantified or the significance of a correlation has to be assessed. This section describes the methods that are used to calculate these statistics. By the end of the chapter, the setup and procedure of the experiments will be described.

5.1 Monte carlo software package

Figure 5.1 shows the graphical user interface of the Monte Carlo software, used for the simulations. These parameters are the input for the simulation. The simulations produce data files that are post-processed with Matlab.

In order to answer the subquestions defined in the introduction, different parameters are varied for different simulations. However, many of the input parameters displayed if figure 5.1 are held constant for every simulation. Most of the input parameters are explained in the paper by Meyer and Kirkland (1998) [1]. However, the software package is updated since then, to include powdered scintillators, next to the already present single crystal scintillators. Unfortunately, this update is lacking literature explaining the model and the parameters that come with it. An elaborate description of every parameter can be found in appendix B.1.

5.2 Simulations

5.2.1 Support material

The first aspect of the camera that is studied is the support material. In the CETA camera design that is studied here, the support of the scintillator is the fiber optic plate. A fiber optic plate is mostly made out of glass (SiO_2), but often heavy materials like Pb are added to shield the photon sensor from x-rays. Such a combination of materials leads to an effective Z that is higher than the Z of pure glass. The effective Z and ρ of the support determines the scattering behavior of the electrons, and thus has an effect on the backscatters.

In this context backscatters are defined as electrons that scatter back from the support to the scintil-

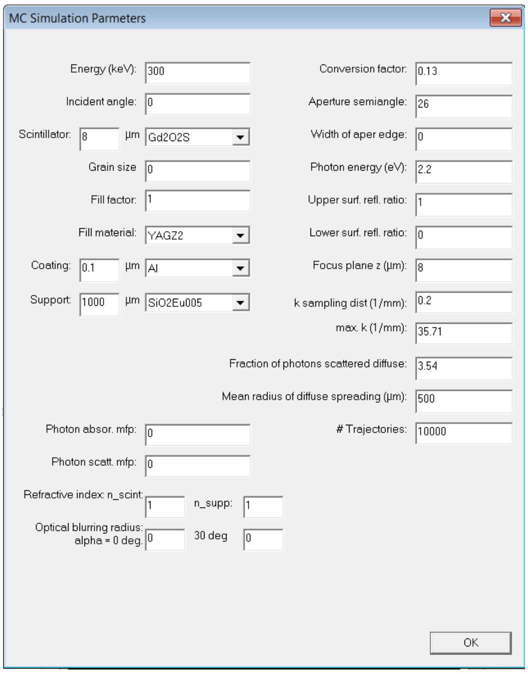

MC Simulation Parmeters

Energy (keV): 300
Incident angle: 0
Scintillator: 8 µm Gd2O2S
Grain size 0
Fill factor: 1
Fill material: YAGZ2
Coating: 0.1 µm Al
Support: 1000 µm SiO2Eu005
Photon absor. mfp: 0
Photon scatt. mfp: 0
Refractive index: n_scint: 1 n_supp: 1
Optical blurring radius: alpha = 0 deg. 0 30 deg 0

Conversion factor: 0.13
Aperture semiangle: 26
Width of aper edge: 0
Photon energy (eV): 2.2
Upper surf. refl. ratio: 1
Lower surf. refl. ratio: 0
Focus plane z (µm): 8
k sampling dist (1/mm): 0.2
max. k (1/mm): 35.71
Fraction of photons scattered diffuse: 3.54
Mean radius of diffuse spreading (µm): 500
Trajectories: 10000

Figure 5.1: Graphical user interface of the monte carlo software, showing the simulation paramters.

lator. This creates a signal at a lateral distance far from the point where the initial beam entered the scintillator, which is observerd as blur in the final image.

It should be noted that the model used by this simulation applies to a single crystal scintillator. The discussion will assess the question to what extend these results apply to granulated scintillators.

Simulations are used to address the question how the atomic number and mass density of the support relates to the number of backscatters and finally the DQE at zero, half and full Nyquist. Again, every other parameter of the camera model is kept constant in order to solely study the support material. The scintillator parameters are chosen according to the current camera design, i.e. an 8 μm thick P43 (Gd_2O_2S) scintillator.

Although the critical angles of the fiber optic are in reality different from one support material to another due to different refractive indexes, these angles are kept constant for these simulations in order to be able to focus on the electron behavior. This means that simulation parameters like the fraction of photons scattering diffuse (f_s, as defined by 4.29) and the aperture semiangle are held constant. The support is chosen to be 1000 μm thick, which in practice means that the electron trajectory will be stopped in the support and will not exit the support at the bottom surface. Again, 10^4 electrons are simulated for the DQE simulations. 13 different materials are chosen as support, ranging from low Z to high Z. All of these materials are elements, except glass. To simulate glass, SiO_2Eu_{005} is chosen, rather than SiO_2. The reason is because SiO_2 showed very unlikely results that were out of line with the other materials. Comparisons with other electron trajectory software showed that this material produced unreliable results. It seems like an error exists in the material parameters of SiO_2 in the software. SiO_2Eu_{005} however, showed trajectories that were nearly identical to the trajectories shown by other software for pure SiO_2. Another argument in favor of the use of SiO_2Eu_{005} is that SiO_2Eu_{010} and SiO_2Eu_{015} showed very similar results, which indicates that 0.5%, 1.0% or 1.5% of Eu in glass does not have a significant influence on the electron scattering.

5.2.2 Scintillator material

The second sub-question introduced in section 1.3 reads: how is the effective atomic number (Z_{eff}) of the scintillator related to the camera perfomance? The simulation software allows to choose from a list of elements to serve as a scintillator material, ranging from light materials like sodium (Na, $Z = 11$) to heavy materials like uranium (U, $Z = 92$). In addition to these elements, one can also select a realistic scintillator material like P43 or YAG. Glass (SiO_2), which is needed to model the support, is also listed.

In order to solely study the effect of the atomic number on electron scattering, the parameters that characterize a scintillator are kept constant, i.e. conversion factor and photon energy. The parameters related to the refractive index of the scintillator are kept constant as well, i.e. aperture semiangle and fraction of photons scattered diffuse. The camera is modeled without support to rule out the effect of backscattering electrons. Other parameters are chosen such that the simulation models the current camera design. E.g. the scintillator thickness is 8 μm, which is equal to the thickness in the current design. For the DQE measurement, 10^4 electrons are simulated. For additional trajectory plots, $10^2 - 10^3$ electrons are simulated.

21 materials are simulated, resulting in a range of atomic numbers between 10 and 92. In order to plot DQE values at a certain frequency versus the atomic number of the scintillator, the atomic number has to be known. Different theoretical methods have been developed to determine the effective atomic number of a compound, e.g. the power law method. Some of them are attractively simple, but Taylor et. al. (2012) [32] demonstrated their inaccuracy and developed software that calculates an energy dependent effective Z curve for compounds. This software is used to calculate an effective Z for the compound materials such as the scintillators listed by the Monte Carlo software. However, Meyer and Kirkland (1998) [1] do not explain how they determined the effective Z for compounds, such as the scintillators and glass. This introduces some uncertainty.

5.2.3 Scintillator thickness

Simulations are run to study how the thickness of the scintillator relates to the DQE at various frequencies. A thick scintillator allows the electrons to generate many photons, which results in a high gain. However, the electrons also have a lot of space in the scintillator to scatter, generating signal at a large lateral distance with respect to the point of impact. This shows up as blur on the final image. When the scintillator is very thin, hardly any signal will be generated since there is very little space available for the electrons to generate photon emission.

The scintillator that is modeled in the simulation shares its properties with the scintillator used in the current CETA design, i.e. a P43 scintillator. First, its thickness is varied without a support underneath the scintillator. This is done to isolate the effect of electron scattering in the scintillator and develop an understanding of this behavior.

Next, the same simulations are done but with two different supports. First, the thickness is varied with a SiO_2Eu_{005} support, and then with an Y support. The idea is that the thickness of the scintillator has an effect on the number of electrons scattering back from the support to the scintillator. The hypothesis is that the number of backscatters will increase as the scintillator thickness increases. The number of backscatters is also expected to be related to the atomic number of the support. The question that this simulation aims to answer is whether the optimal thickness changes when a different support is used. If this is not the case, one would only have to determine the optimal scintillator thickness once, and is free to choose whatever support gives the best performance in terms of DQE.

5.2.4 Numerical aperture

Another property of the support that can be controlled in the camera design is the numerical aperture (NA). The numerical aperture is a measure for the acceptance cone of the fiber optic, explained in section 2.4. A small NA means that the fiber optic has a small acceptance cone, and only photons

are accepted that enter the fiber from a very small angle. A very large NA means that it accepts photons coming at any given angle.
When considering a single crystal scintillator, one would expect to find an optimum DQE at an intermediate NA for the following reasons. When the NA approaches zero, every photon is reflected at the scintillator-support interface and the DQE is zero at every frequency. When the NA has a small but finite value, only a small fraction of the photons is accepted directly. The remaining photons that have an angle outside the acceptance cone of the fiber, are internally reflected and travel through the scintillator until they are scattered at an angle smaller than the acceptance angle, or until they are absorbed by the scintillator. Depending on the absorption mean free path of the scintillator, these photons travel a certain lateral distance before they enter the fiber optic, which has a negative effect on the DQE. When the NA is at its maximum, every photon is accepted by the fiber optic, this includes the ones emitted at a very large angle, at a large lateral distance from the point where it enters the fiber optic. This is also expected to have a negative impact on the DQE. Hence, the DQE is expected to reach a maximum at an intermediate NA where a significant fraction of the photons is directly accepted by the fiber optic, while the remaining fraction scatters diffuse, a part of which will be absorbed by the scintillator.
As the NA becomes smaller, the number of photons that reach the CMOS sensor decreases. As a result, the Poison noise is likely to become more apparent. The hypothesis is that this could be compensated by a higher conversion efficiency, which would shift the maximum DQE(u) to a lower NA. In order to study this behavior, the NA simulations are run for various conversion efficiencies. A small conversion efficiency, $\varrho = 0.05$, an intermediate conversion efficiency used in the other simulations so far, $\varrho = 0.13$, and a high conversion efficiency, $\varrho = 0.50$.

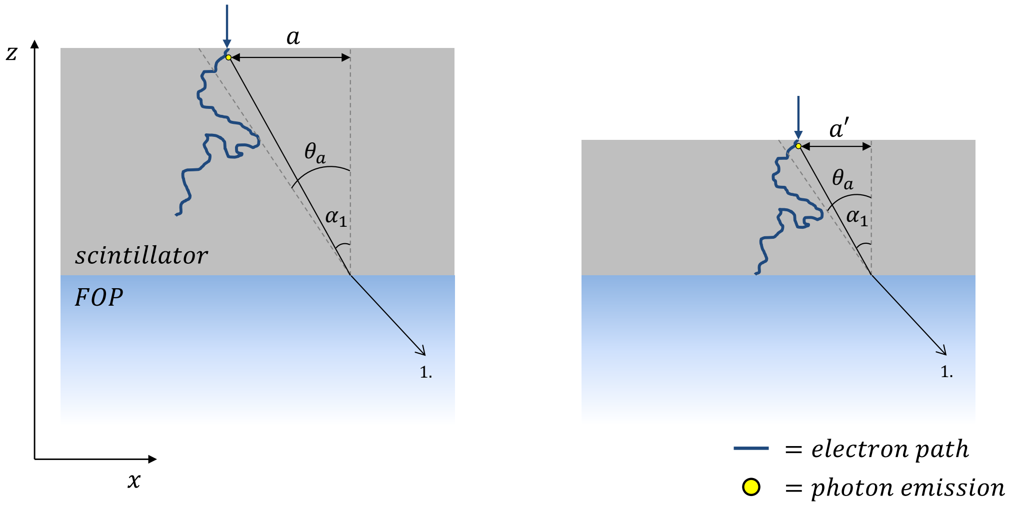

Figure 5.2: Schematic overview of how the optimal NA is expected to depend on the scintillator thickness.

The camera is likely to give a different optimal NA for different scintillator thicknesses. The reason is explained in figure 5.2. This figure shows a schematic representation of two different scintillators, one of them is thick (left), the other one thin (right). The fiber optic beneath each scintillator has an acceptance angle θ_a. When the scintillator is relatively thick, the lateral displacement for a photon emitted at an angle $\alpha_1 < \theta_a$ is a, introducing a certain amount of blur which decreases the DQE at high frequencies. When the scintillator is relatively thin, and a photon is emitted under the same angle $\alpha_1 < \theta_a$, the lateral displacement is $a' < a$, introducing less blur. As such, the relation between DQE and NA is expected to shift when the thickness is varied. This hypothesis is tested by running simulations where the NA is varied for different thicknesses, namely 8 μm, 12 μm, 16 μm and 24 μm.

All these simulations require a variation of the numerical aperture. However, as shown by the user interface in figure 5.1, numerical aperture is not listed among the simulation parameters. The NA can be effectively varied by changing other parameters. The NA is given by equation 2.14, and is a function of the refractive index of the cladding and core of the fiber optic, NA(n_{core}, n_{clad}). This means that the NA can be varied by changing either n_{clad} or n_{core}. However, by changing these variables, other parameters like the aperture semiangle (equation 2.15) and the fraction of photons scattered diffuse (equation 4.29) are also varied. The fraction of photons scattered diffuse neglects the cladding in between the fiber cores, and approximates the upper surface of the fiber optic to be made completely out of cores. Hence, to consistently change the NA through other parameters, only the n_{core} is varied, and the other parameters that depend on n_{core}. The result is shown in table 5.1, where the first column shows n_{core}. Based on the paper written by Meyer & Kirkland (1998) [1], one can calculate through equation 2.14 that for NA$= 1$, given that the support material is glass ($n_{core} = 1.44$), the refractive index of the cladding is $n_{clad} = 1.04$. Combined with the refractive index of a P43 scintillator, $n_{scint} = 2.3$, the values in table 5.1 can be calculated.

Table 5.1: The numerical aperture (second column) is varied by varying n_{core} (first column) and keeping $n_{clad} = 1.04$ constant. As a result, the critical angles in the third and fourth column change, as does the fraction of photons that scatter diffuse in the fifth column. These values are calculated for a P43 scintillator, Gd_2O_2S, $n_{scint} = 2.3$ [5].

n_{core}	NA	θ_t	θ_a	f_s
1.04	0.00	0.00	26.88	8.25
1.06	0.20	5.11	27.44	7.89
1.10	0.36	8.96	28.57	7.21
1.15	0.49	12.32	30.00	6.46
1.22	0.64	16.10	32.03	5.57
1.30	0.78	19.82	34.42	4.71
1.44	1.00	25.66	38.76	3.54
1.60	1.22	31.91	44.08	2.55
1.90	1.59	43.74	55.70	1.29
2.20	1.94	57.45	73.04	0.41
2.52	2.30	86.37	90.00	0

5.2.5 Grain size

As explained in section 2.2, scintillators can have different material structures. In the simulations described so far, the scintillator is modeled as a single crystal. This is because the electron and photon scattering in a single crystal is well understood and well described by literature, while granulated scintillators are still actively being studied. However, the scintillators that are used by the CETA camera system are granulated and the latest version of the simulation software used in this study allows to model grains. This opens the avenue to answer the fifth subquestion mentioned in the introduction: How are the scintillator grain size and fill factor related to the camera performance?

Again, the standard configuration is used for the scintillator and support, i.e. an 8 μm P43 scintallator with a glass support. The numerical aperture is NA$= 1$. First, the fill factor is varied between FF $= 0.1$ and FF $= 1.0$ while keeping the grain size constant at $a = 1$ μm, with a the diameter of the grain.

Next, the grain size is varied between $a = 0.1$ μm and $a = 6$ μm for two different fill factors: FF $= 0.1$ and FF $= 0.7$. Literature suggests a high DQE for small grains. Also, a grain size of

$a = 0$ μm is simulated, together with a finite fill factor, although the physical representation of such a system is a valid point of discussion.
The diffuse scattering in a single crystal is an important effect that has to be considered when studying the relation between DQE and scintillator thickness. However, the introduction of grains suppresses the diffuse spreading of photons. This raises the question whether the relation between DQE and scintillator thickness is different for a granulated scintillator, compared to a single crystal. In order to answer this question, a simulation is run where the thickness of a granulated scintillator is varied. This is compared with the results of the single crystal sintillator.

5.3 Data analysis

For some of the simulations, the question is whether there is a correlation between DQE and a certain parameter. For instance, when varying the support material, the atomic number as well as the mass density is varied. It could be that the DQE is correlated with either one of them, both or none of the two variables. This asks for linear regression analysis that allows to assess the significance of a fit. Fortunately, Matlab allows to do such an analysis. An example of the output of a so-called Goodness-of-fit analysis is shown in figure 5.3.

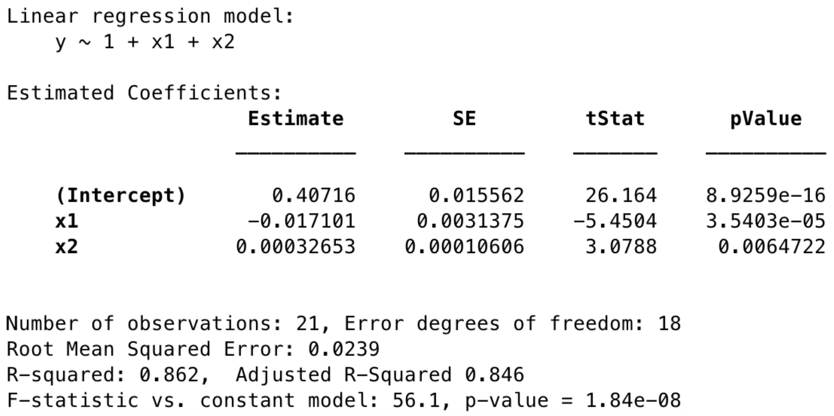

```
Linear regression model:
    y ~ 1 + x1 + x2

Estimated Coefficients:
                    Estimate        SE         tStat       pValue
                   __________    __________    _______    __________

    (Intercept)       0.40716      0.015562     26.164    8.9259e-16
    x1              -0.017101     0.0031375    -5.4504    3.5403e-05
    x2             0.00032653    0.00010606     3.0788     0.0064722


Number of observations: 21, Error degrees of freedom: 18
Root Mean Squared Error: 0.0239
R-squared: 0.862,  Adjusted R-Squared 0.846
F-statistic vs. constant model: 56.1, p-value = 1.84e-08
```

Figure 5.3: An example of the output of a so-called Goodness-of-fit analysis with Matlab. The p-value in the last column indicates the significance of each variable.

Suppose a data set is fitted with a linear model, for example

$$\hat{y} = \beta_0 + \beta_1 x_1 + \beta_2 x_2, \tag{5.1}$$

where β_i are the regression coefficients, $\hat{y}$ is the dependent variable and x_i the independent variable. A t-test or an F-test is done by Matlab to quantify the significance of the correlation. A single variable fit asks for a t-test while a multivariable fit requires an F-test. Each test results in a power value, often abbreviated as p-value. A fit is significant for p-value < 0.05. In figure 5.3 the p-value in the last column tells whether that variable improves the quality of the regression model. If x_1 would have a p-value larger than 0.05, than this variable has no significant contribution to the model and it can be left out. The significance of the overall model is given by the F-test in this case, an results in the p-value at the bottom line of figure 5.3.
The coefficient of determination, R^2, describes the quality of the fit. If $R^2 = 0.86$, it means that 86% of the variance of the data with respect to its mean can be explained by the model that is used to fit the data. A coefficient of determination only makes sense when the correlation is significant, otherwise one would quantify the quality of a correlation that probably does not exist [34].

5.4 Experiments

Experiments have been carried out to measure the DQE of various FOP's. By measuring the DQE of FOP's with varying chemical composition and numerical aperture, the support material and NA simulations can be verified.

First, the chemical composition of each FOP is measured with Energy-dispersive X-ray spectroscopy (EDX). This results in an emission spectrum that reveals the elements that are present in the fiber optic.

Next, each FOP is coated with a P43 scintillator, after which the DQE is measured with 200 keV and 300 keV electrons. The DQE is measured with a so-called beam stop, a device that is integrated in the electron microscope. The beam stop offers an edge that can be used to determine the MTF curve. The camera produces raw image files that are post-processed to determine the MTF, NPS and eventually the DQE curve. Such a raw image file can be found in figure 5.4. The square is the FOP coated by the scintillator, lying on the CMOS sensor. The bright circle is the exposure area, being cut-off by the beam stop.

Equation 3.34 is used to calculate the DQE. In this context, $\overline{q}$ is referred to as the dose in electrons per pixel. The gain, Λ, is called the conversion factor in counts per electron. This is just a matter of convention and the equations express the same relation.

The FOP's that are measured are coming from different suppliers, and each have specific properties. The FOP's are listed in table 5.2. For five out of six FOP's, EDX measurements have been carried out. Half of the FOP's are radiation hard (RH), meaning the FOP will not deteriorate over time. The suppliers calculate the NA of the FOP relative to air. This results in a maximum NA of 1. These numbers can be compared with the simulation results by multiplying the supplier NA with the refractive index of the scintillator ($n_{scint} = 2.3$ for a P43 scintillator). This results in the NA values given in the third column of table 5.2.

Table 5.2: Table of the measured FOP's. The first column reads their label, the second column whether EDX data is available, the third column provides information on the numerical aperture and the fourth on whether the FOP is radiation hard.

Label	EDX data	NA	RH
Eagle	Yes	2.3	No
Supplier 1	Yes	2.3	Yes
Supplier 2	Yes	2.3	No
Supplier 3	Yes	2.3	Yes
Supplier 4	Yes	2.3	Yes
Supplier 5	No	1.5	No

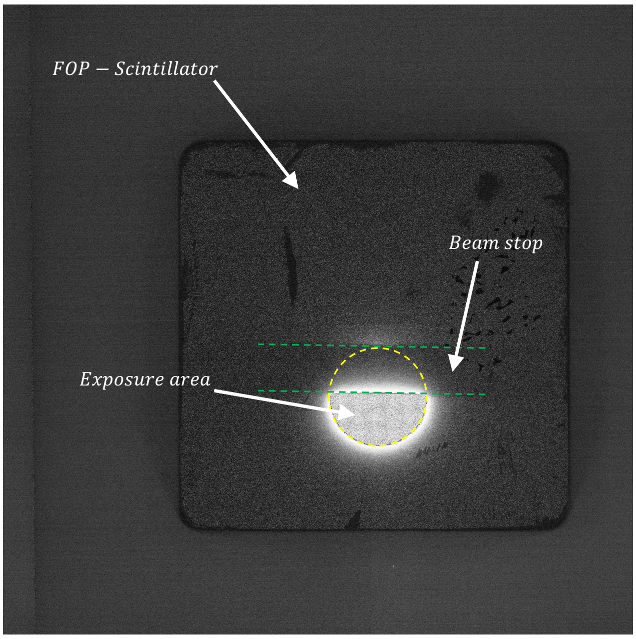

Figure 5.4: Raw image file produced by the camera. The yellow circle indicates the exposure area. The green lines indicate the position of the beam stop.

Chapter 6

Results & discussion

6.1 Support material properties

To study the relation between camera performance, DQE(u), and the atomic number, Z, and mass density, ρ, of the support, 13 different support materials are simulated. These materials are listed in table 6.1. To make the DQE(u) versus frequency plot useful, only 6 out of 13 support materials are plotted. Those materials are chosen such that the entire range of atomic numbers is covered. The materials of which the DQE(u) and MTF(u) curve is plotted in figure 6.1a and 6.1b are glass (SiO_2Eu_{005}, $Z = 10$), Iron (Fe, $Z = 26$), Rubidium (Rb, $Z = 37$), Gadolinium (Gd, $Z = 64$), Tungsten (W, $Z = 74$) and Uranium (U, $Z = 92$). Each curve is plotted from zero frequency to Nyquist frequency.

A few observations can be made when looking at the DQE curve in figure 6.1a. The low and intermediate Z supports (blue and green curves) show a rapid decline in DQE(u) at low frequencies, after which the DQE(u) adopts a constant value. This can be attributed to the electrons that scatter back from the support to the scintillator. High Z supports (red curves), fall off more gradually at increasing frequency. At zero Nyquist, the DQE(0) seems to increase as the atomic number of the support increases. At half Nyquist, this is no longer the case. For increasing atomic number, the DQE(0.5) seems to go down at first, after which it increases again, implicating a parabolic like behavior. This trend seems less pronounced at full Nyquist. These trends will be analyzed more thoroughly shortly, by plotting the DQE(u) at a specific frequency versus the atomic number of the support.

The MTF(u) curves of these materials are plotted in figure 6.1b. Note that the high Z supports result in a better signal transfer low frequencies, while low Z supports (blue curve) perform better at high frequencies, which is in line with the results shown by the DQE(u) curves.

The trajectories of the electrons are plotted for the same six support materials of which the DQE(u) curve was plotted. The plots are shown in figure 6.2. The blue line indicates the scintillator, the area underneath the blue line is the support material. As expected, the electron cloud decreases in size as the mass density increases. After all, a high mass density means a high stopping power.

Next, the DQE(u) at half and full Nyquist is plotted versus the atomic number and mass density of the support material. Each plot is shown as a subfigure of figure 6.3. The first column displays DQE(0.5) and the second column DQE(1). In the first row DQE(u) is plotted versus the atomic number of the support, in the second row versus the mass density and in the third row versus the product of the two. The error bars indicate the variation in DQE of four simulations of 10^4 electrons. The DQE at zero Nyquist can be found in appendix C.1.

The data is fitted with a second order polynomial function. The amount and significance of the correlation is assessed through linear regression analysis. The second order polynomial function

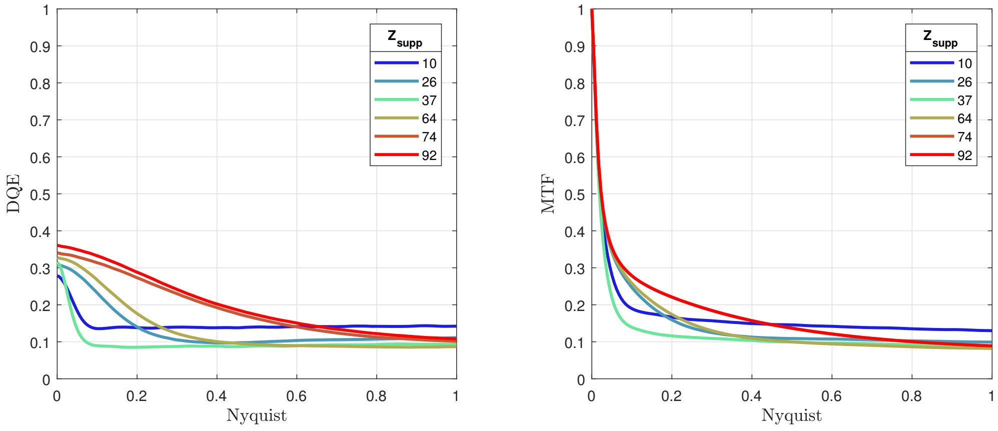

(a) DQE plot.

(b) MTF plot.

Figure 6.1: DQE and MTF vs. spatial frequency in terms of Nyquist frequency. Plotted for an 8 μm P43 scintillator, various supports, 10^4 electrons. Low Z supports are plotted in blue, turning green for intermediate atomic numbers, and red for high Z supports.

used to fit the data is of the following form:

$$\hat{y} = \beta_0 + \beta_1 x_1 + \beta_2 x_1^2, \tag{6.1}$$

where $\hat{y}$ is the dependent variable, in this case the DQE(u), and x_1 the independent variable, either Z of ρ. The regression coefficients are labeled β_i. When applying a significance test to the fitted data, it is important to note that in fact two variables are used to fit the data: x_1 and x_1^2. This asks for an F-test rather than a t-test. The t-test is conventionally used for single variable regression analysis. The results of the significance tests can be found in table 6.2 on the next page.

Table 6.1: Properties support materials, sorted on Z.

Material	Z	ρ (g/cm^3)	$Z \cdot \rho$ (g/cm^3)
SiO$_2$Eu$_{005}$	10	2.65	26.5
Na	11	0.97	10.6
Al	13	2.7	35.1
Si	14	2.33	32.6
Fe	26	7.86	204.4
Rb	37	1.53	56.6
Y	39	4.47	174.3
Sn	50	7.27	363.3
Gd	64	7.9	505.6
W	74	19.25	1424.5
Os	76	22.59	1716.8
Pb	82	11.34	929.9
U	92	19.1	1757.2

At half Nyquist, the DQE(0.5) versus Z plot shows a parabolic trend, see figure 6.3a. The fitted function shows a correlation with a p-value of 0.01 and $R^2 = 0.58$. Although this can be qualified as significant, residual analysis shows two outliers at $Z = 74$ and $Z = 76$. These two materials are tungsten and osmium. The discussion will assess the question what might cause these

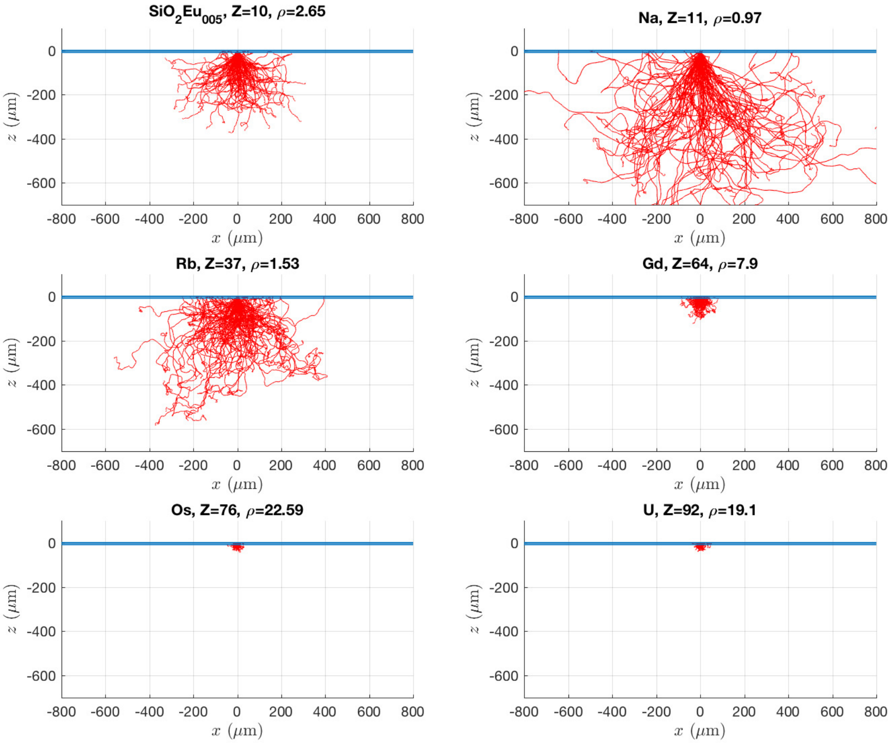

Figure 6.2: Plot of 100 electron trajectories in six different supports. The thick blue line at $z = 0$ μm is an $z = -8$ μm scintillator.

outliers. Excluding them from the data results in a better fit with a p-value of 0.0001 and $R^2 = 0.90$. However, the right arguments to exclude this data are lacking.

The relation between DQE(u) and the mass density of the support is displayed in the second row of figure 6.3. At half Nyquist, shown by figure 6.3c, the parabolic shape can again be observed, and the p-value is 0.0008 with $R^2 = 0.76$. At full Nyquist, the correlation is not significant with a p-value of 0.054 and $R^2 = 0.44$.

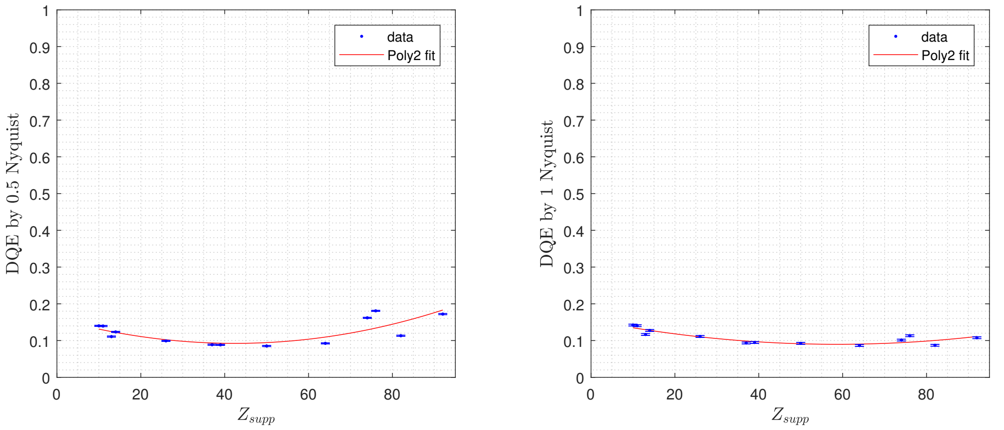

(a) DQE by half Nyquist vs. Z_{supp}. (b) DQE by full Nyquist vs. Z_{supp}.

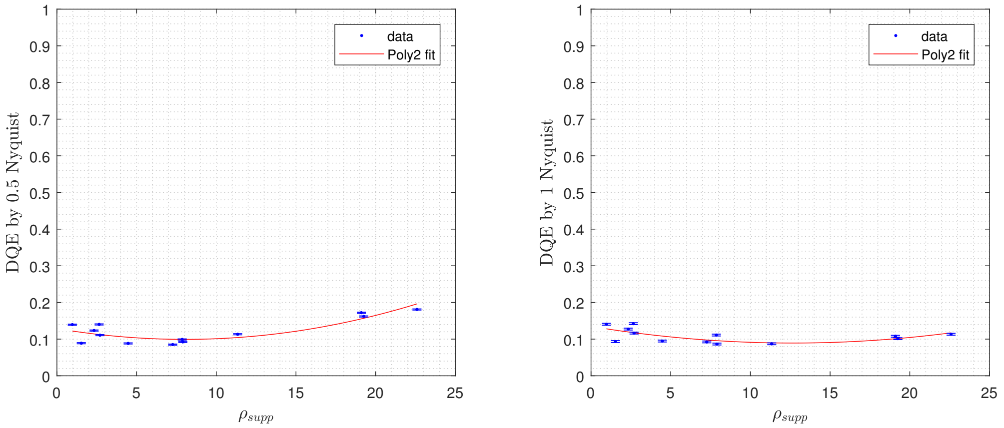

(c) DQE by half Nyquist vs. ρ_{supp}. (d) DQE by full Nyquist vs. ρ_{supp}.

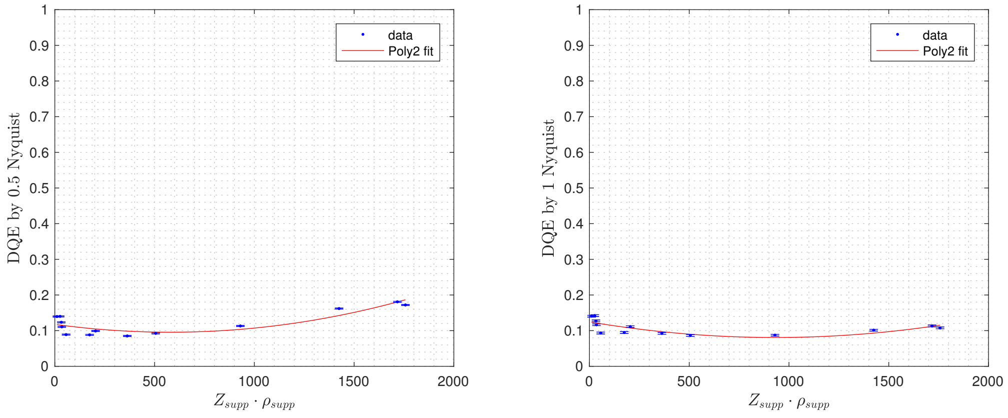

(e) DQE by half Nyquist vs. $(Z/\rho)_{supp}$. (f) DQE by full Nyquist vs. $(Z/\rho)_{supp}$.

Figure 6.3: DQE by half and full Nyquist vs. Z_{supp} (row 1), ρ_{supp} (row 2) and $Z_{supp} \cdot \rho_{supp}$ (row 3). Plotted for an 8 μm Gd_2O_2S (P43) scintillator, various supports, 10^4 electrons.

Another possibility could be that a combined variable like $Z \cdot \rho$ or Z/ρ results in a better fit of the data. Both combinations of variables have been analyzed and the best results were given for the

Table 6.2: Results of the significance tests of the regression analysis expressed in the p-value and the coefficient of determination, R^2. These values correspond to the fitted data in figure 6.3.

	Z		ρ		$Z \cdot \rho$	
	p-value	R^2	p-value	R^2	p-value	R^2
DQE(0)	0.000	0.95	0.001	0.77	0.000	0.82
DQE(0.5)	0.010	0.58	0.001	0.76	0.001	0.77
DQE(1)	0.000	0.80	0.054	-	0.016	0.56

combined variable $Z \cdot \rho$. The data is shown in the figures figures 6.3e and 6.3f. The second order polynomial functions that were used to fit the data showed a significant correlation at zero, half and full Nyquist frequency. The regression model did a particularly better job at half Nyquist. However, at full Nyquist the DQE is best described by the variable Z. An overview of the fit parameters is listed in table 6.2. This table shows that it depends on the spatial frequency which variable does the best job describing the relation between the DQE and the support. However, on average the atomic number has the highest coefficient of determination. When taking into account that the R^2 at half Nyquist versus Z is strongly affected by two outliers, one can conlcude that although mass density certainly plays a role in the electron scattering in the support, the atomic number is the most important variable to describe how the DQE depends on the support material.

6.1.1 Discussion on support material

The simulation of the camera with various support materials showed that the performance has a parabolic relation with the atomic number and the atomic number times the mass density. This section will attempt to explain and understand this trend.

Physical relation between support and DQE

Looking at the trajectories of the electrons in the support in figure 6.2, the first aspect that seems of interest is the size of the electron cloud, also referred to as blob size. The blob size seems to be correlated with the mass density of the support. A large electron cloud in the support is in itself not a problem, the electron does no longer contribute to the signal once it is located in the support. However, there is a finite probability that the electron finds it way back to the scintillator, again generating signal. The larger the size of the electron cloud the larger the distance relative to the point of impact where the backscattering electron generates signal. To make things worse, the electron that re-enters the scintillator has a low energy relative to the electrons that enter the scintillator for the first time at the point of impact. As a result, the scattering cross section is larger, as is the stopping power, allowing the electron to generate photons more efficiently.

The second aspect of the electron trajectories that has an impact on the DQE is the number of backscatters. This number is given by one of the data files that form the output of the simulation software. Knowing the number of electrons that are simulated, the backscatters can be expressed in a percentage of electrons that scattered back to the scintillator.

Quantifying blob size

Both aspects can be examined more closely by looking at a cross section of the electron trajectories at the bottom surface of the scintillator at $z = -8$ μm, shown by figure 6.4. For these plots 1000 electrons are simulated. These scatter plots show every location where the electron enters or leaves the scintillator at $z = -8$ μm, this includes backscatters. This makes it hard to identify which dot represents a backscatter and which one does not. However, for the DQE it does not matter whether a photon stems from a backscatterd electron or not, what does matter is the location where the photon

is emitted.
In order to quantify the average displacement of the electron, the distance of each dot relative to the point of impact is calculated. If the position of electron i at the bottom scintillator surface is $(x_i, y_i, -8)$, its distance to the point of impact in the xy-plane is $r_i = \sqrt{x_i^2 + y_i^2}$. The distribution of r_i for eight different supports can be found in the appendix in figure C.2. The average displacement of n electrons for a certain support can then be calculated with

$$\bar{r} = \frac{1}{n}\sum_{i=1}^{n}\sqrt{x_i^2 + y_i^2}. \tag{6.2}$$

This allows to plot both the percentage of backscatters and average displacement as a function of Z, ρ and $Z \cdot \rho$, shown in figures 6.5 and 6.6.

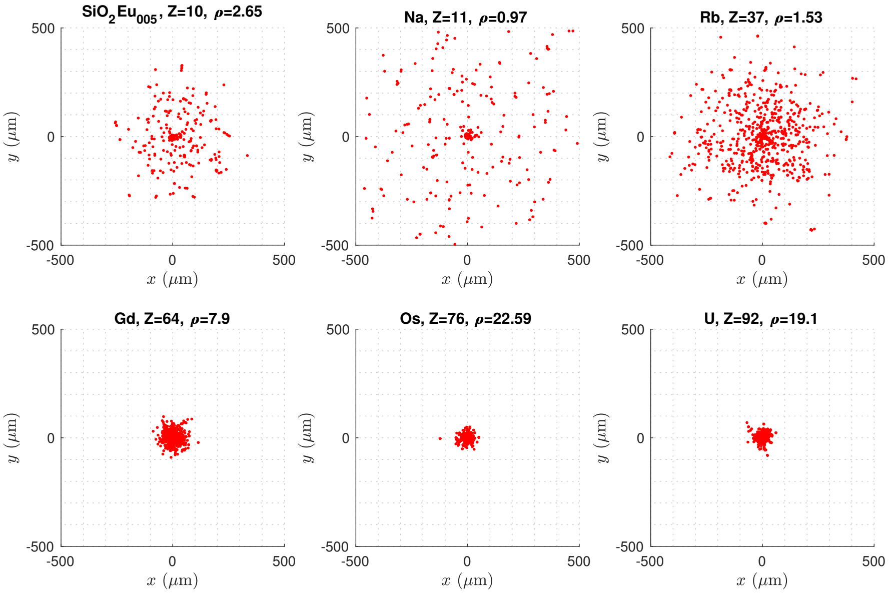

Figure 6.4: Plot of the cross section at $z = -8$ μm of the trajectories of 1000 electrons in six different supports.

Relation between DQE, blob size and backscatters

When plotted versus Z, the backscatters show a clear trend increasing from 14% of backscatters for $Z = 10$ to 56% at $Z = 90$ where the trend starts to level off. This makes sense, if the atomic number increases, so does the scattering cross section and hence the number of scatter events. In addition, the probability of a large scattering angle also increases, given by equation 4.9.

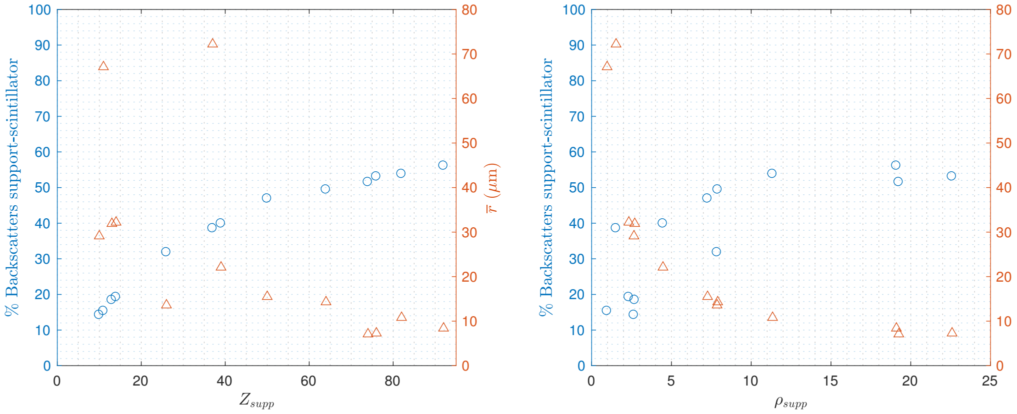

(a) Atomic number.

(b) Mass density.

Figure 6.5: Backscatters from the support to the scintillator and mean displacement of the electrons at $z = -8$ μm versus Z_{supp} (left) and ρ_{supp} (right).

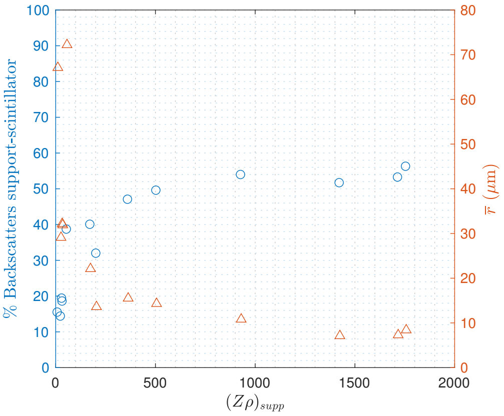

Figure 6.6: Backscatters from the support to the scintillator and mean displacement of the electrons at $z = -8$ μm versus $(Z\rho)_{supp}$

When an electron scatters more often, and the probability of a large scattering angle increases, it is much more likely to find its way back to the scintillator. Hence, the number of backscatters increases for increasing Z.

Although not as neat as the backscatters, the average displacement $\bar{r}$ shows a trend with the atomic number as well. Apart from one major outlier at $Z = 37$, Rb, the average displacement decreases for increasing Z. This outlier can be understood by realizing that the stopping power is directly proportional to the atomic number, and the stopping power quantifies how fast the electron loses its energy and thus how far it can reach. However the stopping power is also directly proportional to the mass density and it is the discrepancy between Z and ρ that causes the outliers. In figure 6.7 a plot of ρ versus Z can be found for all the simulated support materials. The outliers in this plot correspond to the outliers in figure 6.5a, e.g. Rb at $Z = 37$ has an extremely high average displacement although the atomic number is not particularly low, this is due to the fact that is has an unusual low mass density, causing the stopping power to be relatively low which results in a large displacement.

As shown by figure 6.5b, the average displacement is highly correlated to the mass density, whereas the backscatters show more variation as a function of the mass density. These outliers are again explained by the discrepancy between Z and ρ.

These insights can help to understand the parabolic behavior of DQE(0.5) and DQE(1) versus Z, displayed by figures 6.3a and 6.3b respectively. At low Z, the DQE is high because there are very few backscatters, less than 20% of the electrons scatter back to the scintillator. The displacement of those backscatters is high, but the effect on the DQE is limited. For intermediate atomic numbers, the average displacement is smaller, but still large enough to create a significant amount of blur. Combined with the fact that at this point the percentage of backscatters becomes considerable, the DQE suffers from both factors, and reaches a minimum. At large atomic numbers, the number of backscatters continues to increase, but the average displacement drops below 10 μm. An electron that scatters back within 14 μm relative to the point of impact, actually contributes to the signal rather than the noise, which causes the DQE to rise. At his point, a high percentage of backscatters becomes advantageous. This explains the parabolic trend of DQE(0.5). At full Nyquist, electrons that scatter back within 7 μm contribute to the signal. This is of course a smaller fraction of the electrons, which explains why the DQE does not increase as much at high Z compared to half Nyquist.

The same reasoning can be applied to the DQE(0.5) versus ρ plot, but more variation in the data is observed. At full Nyquist, the relation between DQE and ρ is no longer significant. Hence, at these frequencies the atomic number and thus the backscatters play a more important role than the average displacement.

When both variables are combined in a new variable by multiplying them, the new variable $Z \cdot \rho$ is to some degree correlated to both backscatters and blob size, as shown by figure 6.6. As a result, correlation is found at every frequency, and it has the highest R^2 at half Nyquist.

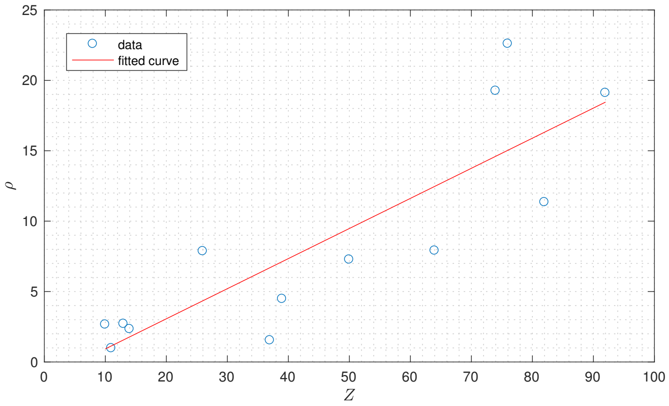

Figure 6.7: Plot of the mass density ρ versus the atomic number Z for all the support materials used in the simulations.

Implications for camera design

The current camera design uses a fiber optic that is for approximately 80% made out of glass (SiO_2) and 20% out of lead (Pb). Using the software developed by Taylor et al. (2012), the effective atomic number of this compound is $Z_{\text{eff}} \approx 26$. The effective mass density is calculated by taking the weighed average and gives $\rho = 4.4$ g/cm^3. Multiplying these numbers gives $Z \cdot \rho \approx 114$ g/cm^3. When placing these numbers in the simulation results, one will learn that this material performs comparable to the worst possible supports, e.g. Y with $\rho = 4.47$ g/cm^3. At half Nyquist, the DQE showed a parabolic trend to some degree with every variable, i.e. as a function of Z, ρ and $Z \cdot \rho$. The parameters of the currently used support can be found right near the bottom of each parabola. To improve performance at half Nyquist of higher, a material should be chosen with either a larger

Z and/or ρ or a lower Z and/or ρ. However, in practice a light material is likely to give better results, since heavy materials are often less transparent for photons. A low Z fiber optic could be a fiber optic of 100% glass. Although in practice some other elements have to be added to tune the refractive index and thus numerical aperture.
As a side note it should be mentioned that the fiber optic also serves as a protection for the photon sensor, shielding it from x-rays. For this, a heavy material like Pb is needed. A solution could be a so-called split FOP, a fiber optic plate composed of two layers, the top layer made of glass, the bottom layer made of glass with a certain percentage of lead. This way, the DQE perfomance is improved while maintaining the x-ray shielding. Based on the trajectory plots, a top layer of 300 μm is expected to be sufficient to give a considerable DQE(0.5) improvement of $40 - 60\%$.

6.2 Scintillator material properties

Frequency dependent DQE curves have been simulated for 21 materials, listed in table 6.3. The first column lists the chemical name of the material, the second column the (effective) atomic number, the third column the mass density and the fourth column the ratio of the atomic number and the mass density. The table is sorted on this ratio.
To enhance visibility, only 6 out of 21 DQE and MTF curves are plotted in figure 6.8a and 6.8b: Silicon (Si, $Z = 14$), Iron (Fe, $Z = 26$), Yttirum (Y, $Z = 39$), Cesium (Cs, $Z = 55$), Gadolinium (Gd, $Z = 64$) and Uranium (U, $Z = 92$). These materials are chosen such that the entire range of atomic numbers is covered.

Based on figure 6.8a, no obvious trends with respect to atomic number can be observed. Perhaps the only observation that can be made is that high Z materials ($Z > 64$) have a relatively high DQE at zero Nyquist and show a stronger decreasing trend with increasing frequency, whereas low Z materials show a rather flat DQE curve. Further analysis will verify whether these observations will hold when the remaining 15 materials are taken into account.
Figure 6.8b shows the MTF curves corresponding to the 6 materials mentioned before. As explained in section 3.2.3, the MTF is normalized at zero frequency. The high Z scintillators show increasingly poor signal transfer at high frequencies.
Results of the other materials can be included in the analysis by plotting the DQE(u) value at a certain frequency u versus the corresponding Z and ρ, analogous to the simulation results of the support material. Figure 6.10 shows six subfigures where the DQE at a specific frequency is plotted versus either the atomic number, the mass density of the scintillator, or the ratio between the two. The first row of subfigures shows the DQE versus the atomic number, Z_{scint}, while the second row shows the DQE versus the mass density ρ_{scint}, the third row displays the DQE versus Z_{scint}/ρ_{scint}.

Table 6.3: Properties scintillator materials, sorted on Z/ρ.

Material	Z	ρ (g/cm^3)	Z/ρ (cm^3/g)
YAG	13.9	4.6	3.0
Co	27	8.9	3.0
Fe	26	7.86	3.3
Os	76	22.59	3.4
Mn	25	7.21	3.5
SiO_2Eu_{005}	10	2.65	3.8
W	74	19.25	3.8
Gd_2O_2S	32	7.3	4.4
U	92	19.1	4.8
Y_2O_2	22	4.1	5.4
Si	14	2.33	6.0
Sn	50	7.265	6.9
Pb	82	11.34	7.2
ZnCdS	31	4.2	7.4
Gd	64	7.9	8.1
Y	39	4.47	8.7
Na	11	0.968	11.4
Sr	38	2.64	14.4
Ba	56	3.51	16.0
Rb	37	1.53	24.2
Cs	55	1.93	28.5

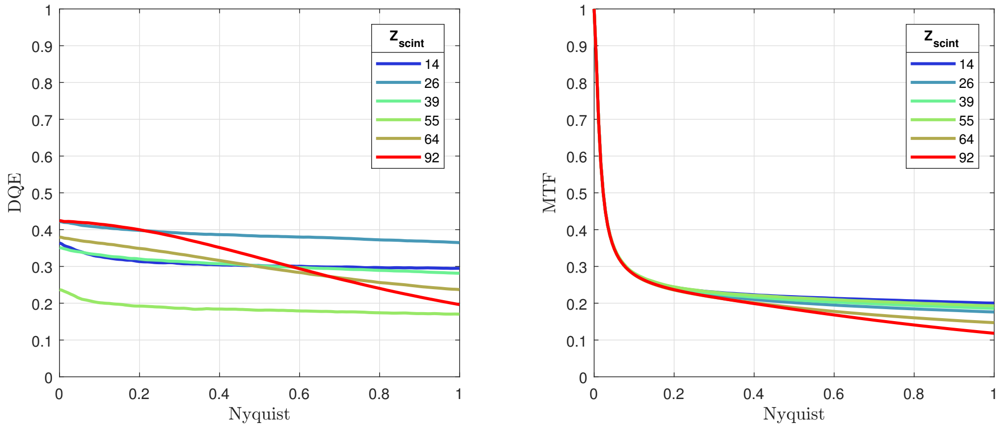

(a) DQE plot.

(b) MTF plot.

Figure 6.8: DQE and MTF vs. spatial frequency in terms of Nyquist frequency. Plotted for various 8 μm scintillators, no support, 10^4 electrons. Low Z scintillators are plotted in blue, turning green for intermediate atomic numbers, and red for high Z scintillators.

The first column presents DQE at half Nyquist and the second column at full Nyquist. The DQE at zero Nyquist versus each variable can be found in appendix C.2.

The error bars in figure 6.10 indicate the spread when the simulation is done four times. The red curve is a linear fit through the data points. The amount of correlation and the significance of the correlation can be quantified by regression analysis. Each plot in figure 6.10 if fitted with a linear regression model. The results can be found in table 6.4.

The results of the regression shows that the DQE is not correlated with the atomic number of the scintillator, nor is it with the mass density of the scintillator.

If the variation in DQE cannot be explained by either the atomic number of the scintillator or its mass density, perhaps a linear combination of the two might show a significant correlation with a high coefficient of determination. After all, these are the only parameters that are varied throughout the simulations. A regression fit of the following form could be used:

$$\mathrm{DQE}(u) = \beta_0 + \beta_1 Z_{scint} + \beta_2 \rho_{scint}. \tag{6.3}$$

However, a function in this form would assume that Z_{scint} and ρ_{scint} are independent, while there could be a correlation between the two. A plot of ρ_{scint} versus Z_{scint} in figure 6.9 reveals a significant linear correlation with a p-value of 0.00015 and $R^2 = 0.54$. This implies a multicolinearity of the variables Z_{scint} and ρ_{scint} with respect to DQE(u). This can be tackled by introducing a new variable that is a combination of the former. A common choice would be $Z_{scint} \cdot \rho_{scint}$, however, Z_{scint}/ρ_{scint} resulted in a better fit. Using a second order polynomial, the following function was used to fit the DQE(u):

$$\mathrm{DQE}(u) = \beta_0 + \beta_1 (Z_{scint}/\rho_{scint}) + \beta_2 (Z_{scint}/\rho_{scint})^2. \tag{6.4}$$

The DQE at half and full Nyquist is plotted versus Z_{scint}/ρ_{scint} in figure 6.10e and 6.10f respectively. The data is fitted with equation 6.4. The p-value is calculated using the F-test for multiple regression. At zero Nyquist, this resulted in a significant correlation with p-value$= 5.77 \cdot 10^{-8}$ and $R^2 = 0.84$. At half Nyquist, the correlation remains significant with p-value$= 1.84 \cdot 10^{-8}$ and $R^2 = 0.86$. At full Nyquist, the model becomes less accurate, but the correlation remains significant with p-value$= 0.0113$ and $R^2 = 0.39$. The p-value and coefficient of determination for every fit is listed in table 6.4.

Table 6.4: Results of the significance tests of the regression analysis expressed in the p-value and the coefficient of determination, R^2. These values correspond to the fitted data in figure 6.10 and C.3.

	Z		ρ		Z/ρ	
	p-value	R^2	p-value	R^2	p-value	R^2
DQE(0)	0.59	-	0.001	0.43	0.000	0.84
DQE(0.5)	0.53	-	0.058	-	0.000	0.86
DQE(1)	0.000	0.49	0.276	-	0.011	0.39

The trajectories of 100 electrons are plotted in figure 6.11 for scintillators corresponding to the DQE curves in figure 6.8a. The plots are sorted from low Z_{scint} (top figure) tot high Z_{scint} (bottom figure).

Together, these results show that the DQE has a significant relation with both the mass density and the atomic number of the scintillator through the introduction of the combined variable Z_{scint}/ρ_{scint}. To realize a high DQE, one should aim for a low Z_{scint}/ρ_{scint}. In the discussion section the colinearity and shape of DQE versus Z_{scint}/ρ_{scint} will be further assessed.

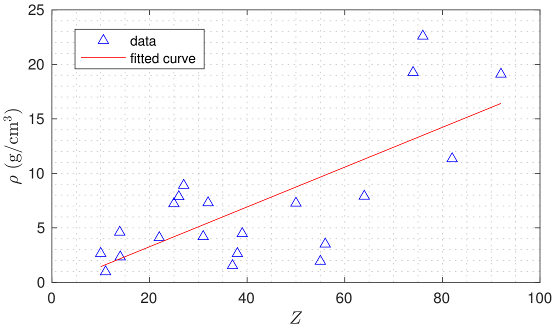

Figure 6.9: Plot of the mass density ρ versus the atomic number Z for all the elements used in the simulations.

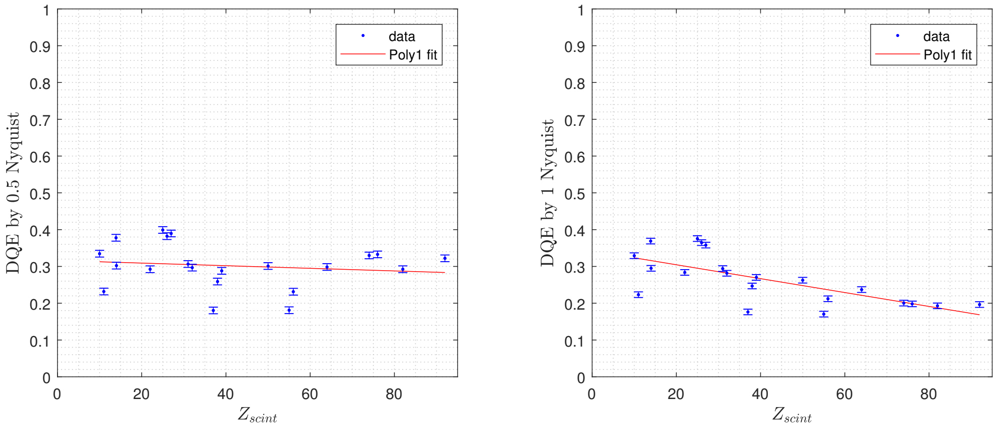

(a) DQE by half Nyquist vs. Z_{scint}.

(b) DQE by full Nyquist vs. Z_{scint}.

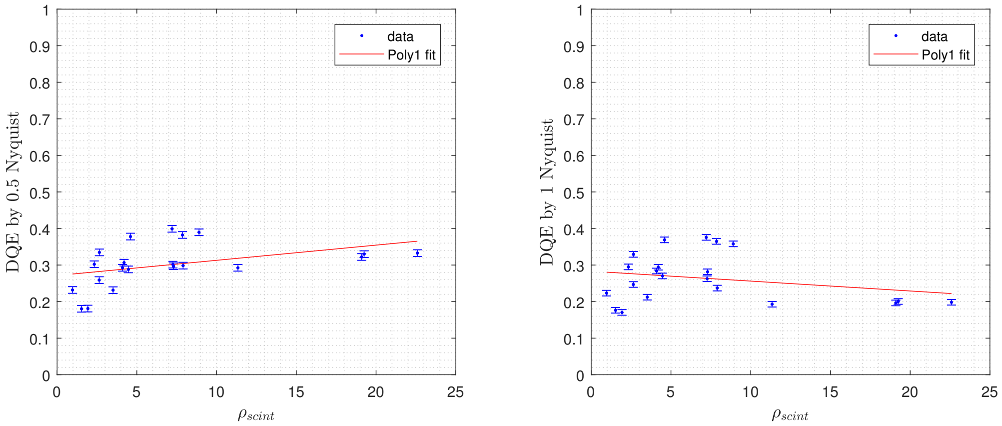

(c) DQE by half Nyquist vs. ρ_{scint}.

(d) DQE by full Nyquist vs. ρ_{scint}.

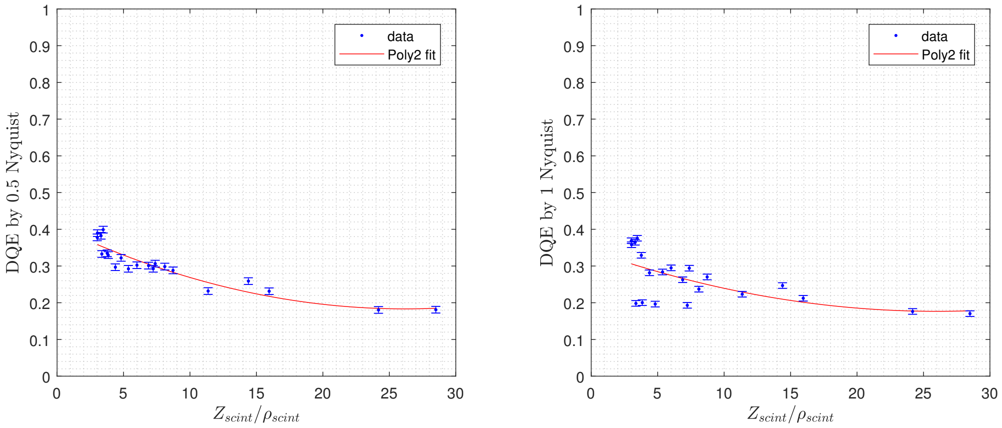

(e) DQE by half Nyquist vs. $(Z/\rho)_{scint}$.

(f) DQE by full Nyquist vs. $(Z/\rho)_{scint}$.

Figure 6.10: DQE by half and full Nyquist vs. Z_{scint} (row 1), ρ_{scint} (row 2) and $Z_{scint} \cdot \rho_{scint}$ (row 3). Plotted for an 8 μm scintillator, no support, 10^4 electrons.

6.2.1 Discussion on scintillator material

Results in this section demonstrated that the camera performance in terms of DQE was not correlated to a single variable, but a colinearity exists with both mass density and atomic number. This raises the question how this colinearity can be understood and why none of these variables alone shows a significant correlation.

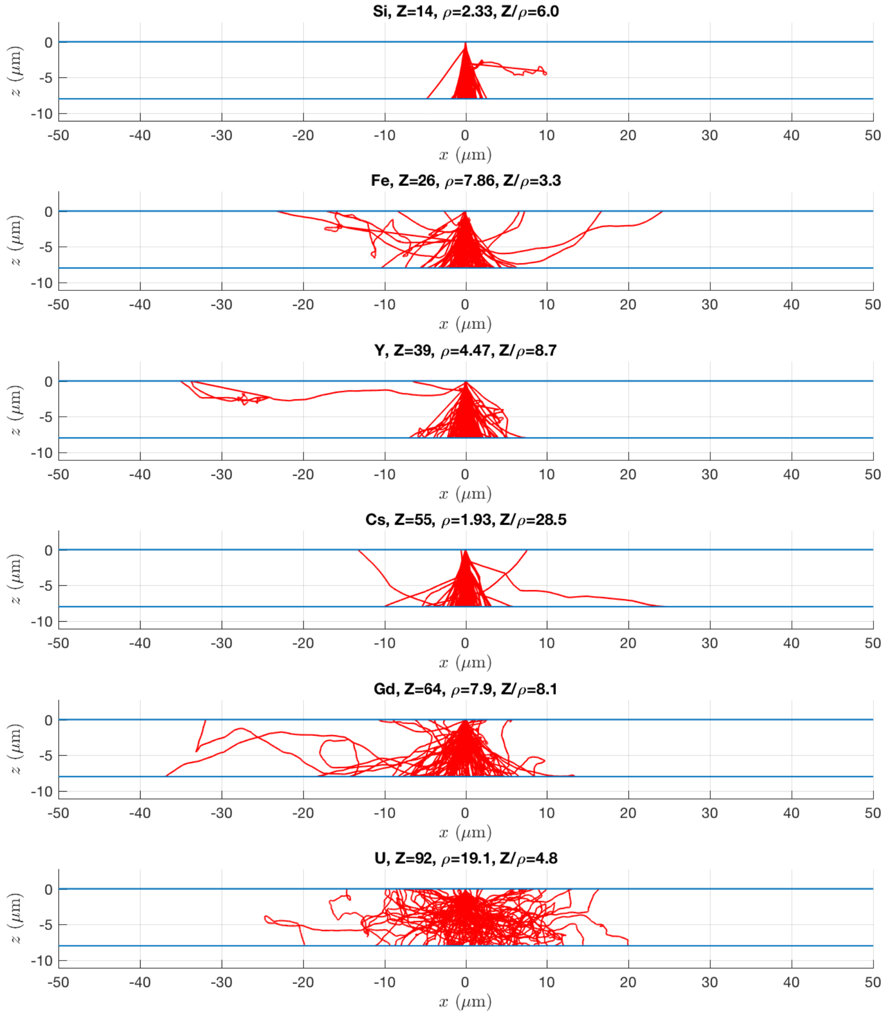

Figure 6.11: Plot of 100 electron trajectories in six different scintillators. From top to bottom: Si, Fe, Y, Cs, Gd and U. The region between the blue lines at $z = 0$ μm and $z = -8$ μm is the scintillator.

Relation between electron scattering and the atomic number and mass density

To understand how ρ_{scint} and Z_{scint} have an effect on electron scattering (elastic and inelastic), it serves to look at the equations that are involved with the single scattering model by Joy (1995), explained in section 4.2. The interaction of the electron with the scintilator can be broken down in elastic and inelastic scattering events. The trajectory is determined by the elastic scattering events, while the inelastic events induce the emission of photons. The trajectory is described by the distance between two elastic scattering events, and the scattering angle that an electron makes at such an event. The average distance an electron travels before an elastic scattering event occurs is given by the mean free path, which is given by equation 4.3. It is proportional to the screened Rutherford scattering cross section, σ_E, the atomic mass, A, and the mass density, ρ. This scattering cross section is given by equation 4.1, and is proportional to the atomic number squared, Z^2 and inversely proportional to the electron energy squared, E^2. Finally, the scattering cross section is also proportional to the screening factor α, which in turn depends on both Z and E. Taking all these relations into account, the mean free path is a function of Z, A, ρ and E. The atomic mass shows very similar correlations with DQE as the atomic number, which makes sense since most often they only differ by a factor of approximately two. This makes the atomic mass a dependent variable. This results in the relation $\lambda \propto Z, \rho, E$. If the electron energy is kept constant for the moment, a rapid decrease in λ is seen for increasing Z and ρ. This means more elastic scattering is taking place.

The next question would be in which direction does the electron scatter, i.e. how does the scattering angle relate to the material parameters. The polar scattering angle is given by equation 4.9 and depends on the screening factor α, which in turn depends on Z and E. Hence, $\phi \propto Z, E$, the scattering angle depends on the atomic number and the electron energy, not on the mass density.

However, the elastic electron scattering cannot be fully characterized without taking into account the inelastic scattering. The electron energy is an input parameter for both the scattering mean free path, λ, and the polar scattering angle, ϕ. The amount of energy that an electron loses over a path length s through inelastic collisions determines its energy at the end of the step, which is the input for the scattering parameters of the next step. Because of this, the elastic scattering events of the electron depend on the inelastic scattering events as well. This means that to fully understand the elastic scattering behavior of the electron, one should also take inelastic scattering into account, described by the stopping power. The stopping power is given by 4.21, and is proportional to the atomic number, atomic mass, mass density and electron energy, $\mathrm{d}E/\mathrm{d}s \propto Z, A, \rho, E$.

Hence, both elastic and inelastic electron scattering depend on atomic number and mass density. Only considering one parameter is not sufficient to explain the scattering behavior. This can be understood by looking at figure 6.9 where the mass density is plotted versus the atomic number. Though correlated, ρ and Z do not show a perfect linear relation, i.e. there exists spread around the linear fit. This is quantified by the coefficient of determination, $R^2 = 0.54$. This number means that 54% of the variance of the data with respect to the mean is explained by the fitting model. This makes both variables independent, which prevents one of the two from being able to fully characterize the scattering behavior.

Physical explanation of the observed DQE trend

Knowing how the model is related to the atomic number and the mass density, it is interesting to asses whether the trend that the DQE shows with Z_{scint}/ρ_{scint} can be understood. First, the trend at zero and half Nyquist, shown in figure C.3c and 6.10e respectively, will be analyzed. These figures show a clear trend where scintillators with a low Z_{scint}/ρ_{scint} ratio exhibit a high DQE. This ratio being low means either the atomic number is low, for example the YAG scintillator with an effective atomic number of 13.9. Or the mass density is high, like for Os with a mass density of 22.59 g/cm^3. Or something in between, which is the case for Fe with an atomic number of 26 and a mass density of 7.86 g/cm^3.

In order to answer the question how the atomic number and mass density could negatively influence the DQE, the ideal scattering conditions have to be defined. Knowing the physical relations, for which atomic number and mass density can ideal scattering conditions be expected. An ideal scintillator would introduce no elastic scattering, since elastic scattering causes blur. If the scintillator does introduce elastic scattering, then the scattering angle should be as low a possible, such that the electron deflection is negligible. On the other hand, the stopping power of the scintillator has to be reasonably high, since the stopping power is related to the gain. In a good scintillator, the gain should be high relative to the variance of the gain.

How should the material parameters be tuned in order to achieve these ideal scattering conditions? In order to suppress elastic electron scattering, the mean free path, λ, should be high. This can be achieved by a low Z and low ρ. The material with the largest λ is Na, which turns out to have the lowest $Z \cdot \rho$. Minimizing the scattering angle only involves the atomic number, Z. To yield a small scattering angle, Z should be low.

So far, designing a good detector simply involves choosing a scintillator with a Z and ρ combination that is as small as possible, e.g. Na. But according to the results presented, this material does not give the best performance. The elastic electron scattering conditions are good in a low Z and low ρ material like Na and Si. This is confirmed by the trajectory plots in figure 6.11, where the Si scintillator shows the smallest electron deflection and no backscattering electrons. However, a low atomic number and low mass density also means a low stopping power, which results in a low gain. For example, Na has the lowest gain of 15 photons/electron, while Os has the highest with 603 photons/electron. It is the ratio of the gain and the variance of the gain that defines the DQE at zero Nyquist through equation 6.5. Hence, a high DQE(0) asks for a high stopping power, which can be achieved by a high Z and ρ.

Another contributor to the variance of the gain is the variance in path length of the electron trajectory. This relates the variance in gain to electron scattering. More electron scattering introduces a larger variety of electron path lengths, some electrons might encounter little deflection, while others might travel a rather large distance through the scintillator before the fiber optic is reached. This introduces a variance in path lengths, and thus a variance in the number of photons an electron emits. As a result, it is for the sake of a low variance of the gain, to minimize electron scattering. This requires a low Z and ρ. As shown by figure C.3c, the best *gain/variance gain* ratio is achieved at low Z_{scint}/ρ_{scint}, i.e. high ρ. The introduction of gain in the discussion allows to understand why trajectory plots are useful to provide additional insight, but fail to explain entire trends. A trajectory plot gives some information about the elastic electron scattering, but does not show how many photons are emitted along a certain path. A low Z material can show perfect electron scattering properties, but if the gain is low, it will still have a poor DQE.

Obviously, some of these requirements are contradicting with each other. On one hand, a heavy high Z, high ρ material is required to establish sufficient stopping power, while on the other hand these heavy materials introduce elastic scattering, which results in a poor DQE. A compromise that results in good performance can be found by taking a material with a low Z, thereby keeping the scattering cross section small, and more importantly, keeping the scattering angle small. By choosing a high mass density, the stopping power remains high enough to achieve a decent gain. A high ρ means that the mean free path will be shorter, which results in more scattering. However, the scattering angle is unaffected, since it only depends on the atomic number. As a result, the amount of blurring remains limited. Hence, from a theoretical point of view, one could anticipate that a low Z and a high ρ would give the best DQE, which is confirmed by figure 6.10e where the DQE at half Nyquist decreases as Z_{scint}/ρ_{scint} increases. As discussed, a low ratio between the atomic number and mass density can be found through several combinations of parameters. At half Nyquist, it does not matter whether a low ratio is caused by a low Z, a high ρ or something in between. At full Nyquist however, the scintillators with low Z_{scint}/ρ_{scint} but high ρ, show a drop in DQE. These are Os, W, U and Pb. These materials have a high mass density and at full Nyquist their DQE dropped to 0.2. These materials have a relatively high Z and high ρ, causing more electron scattering. This might not have a large influence on the DQE at half Nyquist, but shows up at full Nyquist. Hence, in order to maintain a high DQE at full Nyquist, in addition to choosing a small Z_{scint}/ρ_{scint}, each of the parameters should be low too.

Comparison with realistic scintillators

How do these results compare to realistic scintillators? There are two important differences between these simulations and realistic scintillators. First, many of the parameters that distinguish realistic scintillators from one another, such as conversion efficiency, photon absorption mean free path and photon scattering mean free path are held constant. This means that for example while ZnCdS had a rather poor imaging performance based on its atomic number and mass density, it might in practice be a good scintillator because of a high conversion efficiency. However, the goal of these simulations is to study how the material properties of the scinitllator, such as Z and ρ affect the elastic and inelastic electron scattering and how the imaging performance is related to these parameters. This allows to make general statements about whether to use light or heavy materials as scintillators, not taking into account further scintillating properties as conversion efficiency and decay time. The second difference concerns the type of scintillator that is modeled. In these simulations, the scintillator is modeled as a single crystal, while most of the scintillators used for microscopy purposes are powdered scintillators. The consequences of choosing to model a single crystal, rather than a powdered scintillator will be discussed more extensively in the grain size discussion. For now, it suffice to note that these simulations aim to study the electron scattering behavior, rather than the photon scattering behavior. As will be explained, the electron scattering will only be affected by the grain size and fill factor at very small fill factors, *fill factor* < 0.6.

6.3 Scintillator thickness

A P43 scintillator is simulated with a thickness varying between $1\ \mu$m and $32\ \mu$m. The resulting DQE curves for the simulations without support are shown in figure 6.12a, where the thin scintillators are plotted in blue, turning green for scintillators with medium thickness and red for thick scintillators. Right from this figure one can observe that the DQE(u) increases for increasing thickness, but the curve tilts, effectively causing the DQE at high frequencies to decrease after a maximum is reached (for $t > 12\ \mu$m).

The MTF curves are closely related to the electron scattering, and the electron scattering is suppressed when the scintillator is thin. The MTF curves in figure 6.12b indeed show that the MTF curve suffers from an increasing thickness of the scintillator.

The DQE and MTF curves for the scintillator with a SiO_2Eu_{005} or Y support show a similar trend. Those results can be found in figure 6.13 and 6.14 respectively. The presence of a support causes a rapid decline in DQE at low frequency, observed earlier in the study of support materials. This is caused by the backscatters. Further characteristics are very similar, and mainly differ in magnitude.

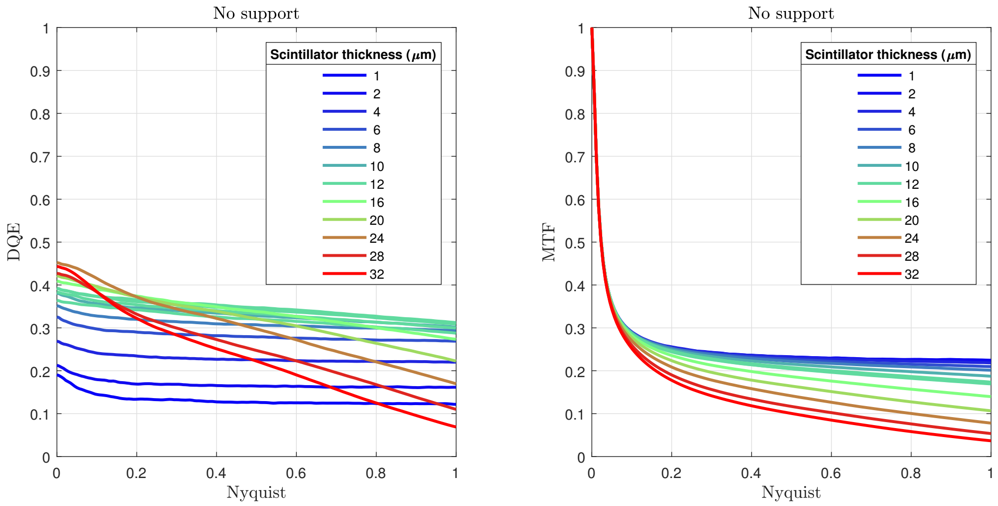

(a) DQE plot.

(b) MTF plot.

Figure 6.12: DQE and MTF vs. spatial frequency in terms of Nyquist frequency. Plotted for a P43 scintillator of varying thickness. No support, 10^4 electrons.

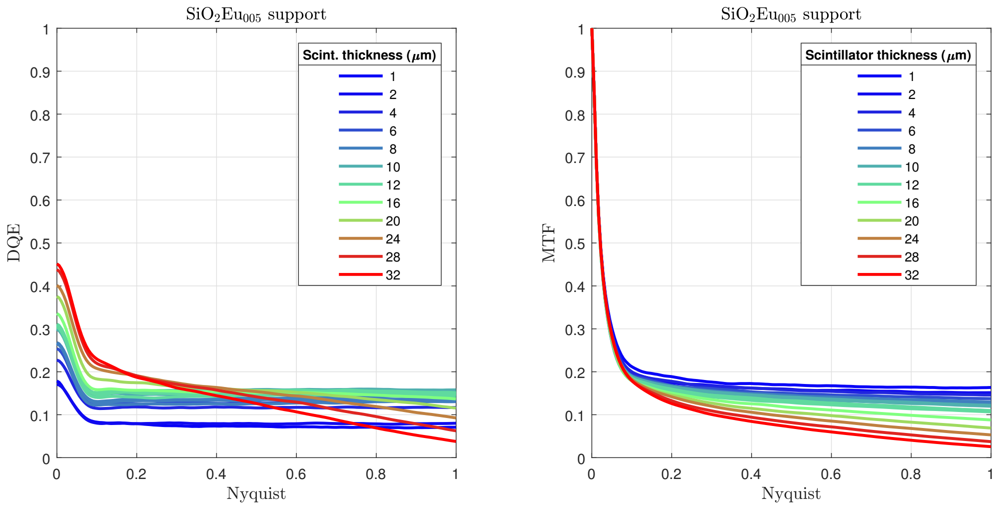

(a) DQE plot.

(b) MTF plot.

Figure 6.13: DQE and MTF vs. spatial frequency in terms of Nyquist frequency. Plotted for a P43 scintillator of varying thickness. SiO_2Eu_{005} support, 10^4 electrons.

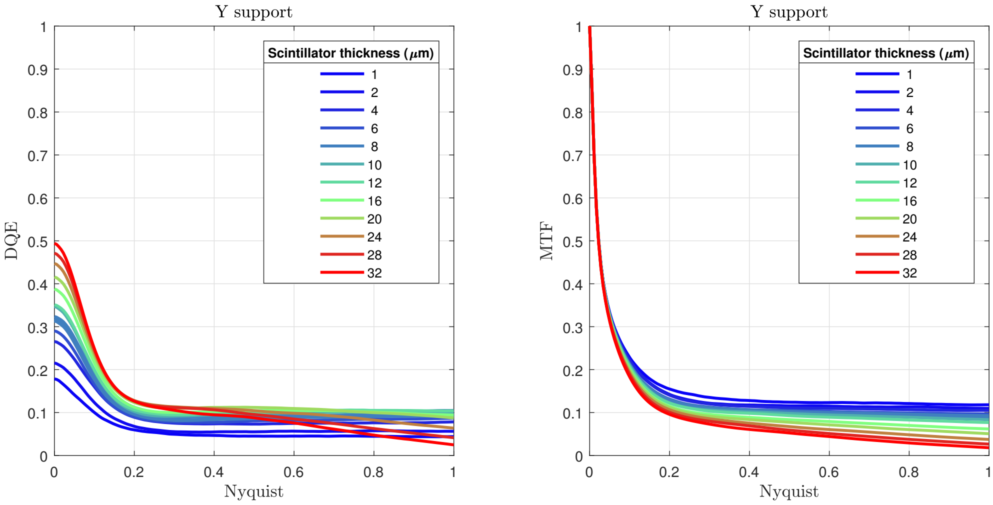

(a) DQE plot.

(b) MTF plot.

Figure 6.14: DQE and MTF vs. spatial frequency in terms of Nyquist frequency. Plotted for a P43 scintillator of varying thickness. Y support, 10^4 electrons.

DQE, scintillator thickness and spatial frequency form a three dimensional space. To make the results more insightful, a cross section is made at zero, half and full Nyquist frequency. This results in a plot of the DQE(u) with u being one of the mentioned frequencies versus the scintillator thickness for each of the three support possibilities (no support, SiO$_2$Eu$_{005}$ or Y). The results can be found in figures 6.15 and 6.16.

DQE(0) increases as a function of t. The rate at which it increases declines after $t = 10$ μm. For $t > 15$ μm the DQE(0) does no longer increase significantly. The simulations with support also show an increase of DQE(0) as a function of thickness, and show the same decline in rate at which it increases at $t = 10$ μm. For these simulations, the DQE(0) keeps increasing as t increases, in contrast to the simulation without support.

At half and full Nyquist frequency, the simulation without support shows the highest DQE over the entire range of thicknesses. The simulation with glass support performs second best, and the Y support performs worst. This is in accordance with the simulation results of the support materials, that showed that a light material like glass will perform better than a material with an atomic number between 20 and 70, such as Y. More importantly, the simulations without support show that the DQE(0.5) finds its maximum value between $t = 9$ μm and $t = 17$ μm, taking into account the error bar. The peak is rather broad though, and even more so for the simulations with support, where the optimum thickness covers a range between $t = 10$ μm and $t = 24$ μm.

At full Nyquist, the peak narrows, giving an optimal DQE(1) between $t = 8$ μm and $t = 13$ μm with no support, and a peak between $t = 9$ μm and $t = 15$ μm for the SiO$_2$Eu$_{005}$ or Y support.

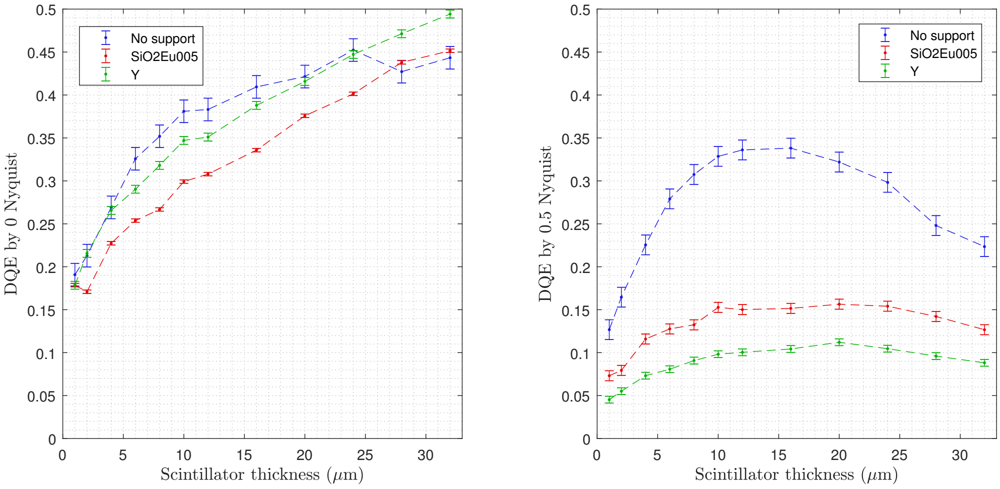

(a) DQE at zero Nyquist vs. scintillator thickness. (b) DQE at half Nyquist vs. scintillator thickness.

Figure 6.15: DQE at zero and half Nyquist vs. thickness of the scintillator. Plotted for a P43 scintillator. Various supports, 10^4 electrons.

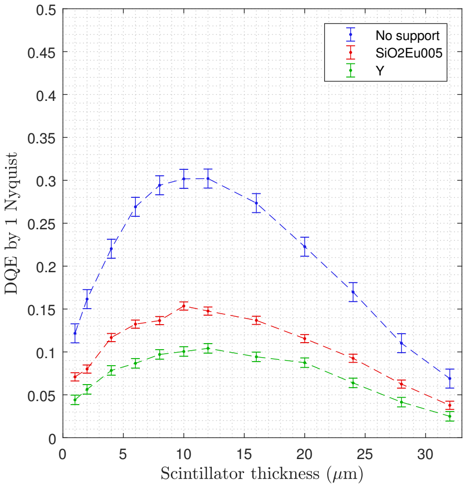

Figure 6.16: DQE at full Nyquist vs. thickness of the scintillator. Plotted for a P43 scintillator. Various supports, 10^4 electrons.

6.3.1 Discussion on scintillator thickness

Data analysis

In contrast to similar plots made earlier, this time the data is not fitted by a polynomial function. In these experiments the correlation is rather obvious since there is actually only one parameter varied, the thickness, whereas in the scintillator and support material simulations both the atomic number and mass density were varied. These simulations aimed to answer the question whether certain variables where correlated and if yes, to what extend. In the scintillator thickness simulatons, it is the shape of the relation that is of interest.

In addition, these results are not properly fitted by a linear regression model. In order to have a fit provide valuable information in terms of a p-value, the fit has to be linear. This includes the possibility of a parabolic trend where y can have a linear relation with the variable x_1^2 through the coefficient β_1. These results ask for non-linear regression which cannot asses the goodness-of-fit in a similar way.

Interpretation of relation between DQE(0) and scintillator thickness

The DQE versus t curve for the simulation without support shows an obvious trend at each frequency. At zero Nyquist the DQE seems to saturate at some point for increasing thickness. Several factors could explain this based on the two most important stochastic processes that take place in the scintillator. These two processes are electron scattering, which leads to a variance in electron path length and hence a variance in gain. And photon emission, which is a Poison process and therefore intrinsically gives a variance in the gain.

The Poison noise could become a significant factor when the scintillator is so thin only several photons are emitted. The actual impact of Poison noise on DQE(0) can be quantified. After all, the DQE at zero frequency is related to the stochastic nature of the amplification mechanism of the scintillator, which is a Poison process. The equation for DQE(0) was given in section 4.4, but for convenience shall be reprinted here:

$$\mathrm{DQE}(0) = \frac{1}{1 + \frac{\mathrm{variance}(\Lambda)}{\mathrm{mean}(\Lambda)^2}}, \tag{6.5}$$

where Λ is the gain in photons per electron.

The variance in the gain is determined by two factors: the variance in path length, which is due to scattering, and the Poison noise. Based on Poison statistics, the variance due to Poison noise should be in the order of $\sigma_{pois}^2 \approx \Lambda$. Note the approximate sign, the variance of a Poison process should approach Λ for an increasing number of observations, but it is a stochastic process which means that in the simulations the actual variance due to Poison noise might deviate from $\sigma_{pois}^2 = \Lambda$. However, knowing the gain, this gives an idea of the significance of the Poison noise. For example, at $t = 2$ μm the gain is $\Lambda = 12$ phot/elec and the variance in the gain is $\sigma_{\text{tot}}^2 = 574$ (phot/elec)^2. This means that the variance due to Poison noise is $\sigma_{\text{pois}}^2 = 12$ (phot/elec)^2, which accounts for 2% of the total variance in gain.

The total variance and the estimated variance due to Poison noise is plotted versus the scintillator thickness in figure 6.17. This figure demonstrates that the impact of Poison noise on the variance in the gain is very small, in particular at larger thicknesses. This makes sense since a thicker scintillator means a higher gain and hence a higher signal-to-Poison-noise ratio.

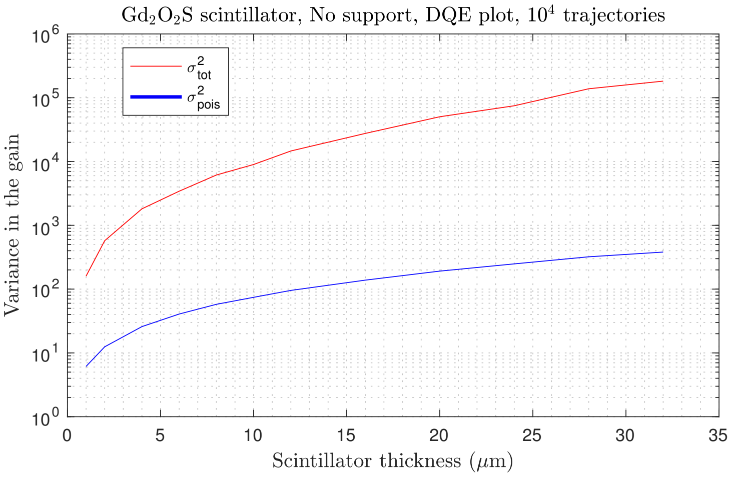

Figure 6.17: A plot of the total variance in the gain, σ^2_{tot} and an estimation of the magnitude of the variance in the gain due to Poison noise, σ^2_{pois}, versus the scintillator thickness. The Poison noise is negligible relative to the total variance in the gain.

Overall, these arguments allow to draw the conclusion that the initial increase of DQE(0) as a function of t is not caused by the decreased relative impact of Poison noise.

This conclusion implies that the trend shown by DQE(0) as a function of t can be explained by electron scattering. As t increases, the gain increases since the electrons travel a longer path in the scintillator. The variance in the gain increases as well, but not as fast as the gain itself, since for a scintillator that is very thin, the electrons have nearly 300 keV, and the scatter events result in a very small deflection. Hence the variance in gain due to a variance in path lengths is small, and the gain grows faster than the variance in the gain, resulting in an increasing DQE(0).

As t grows larger, the electrons dissipate more energy in the scintillator, increasing the probability of a scatter event and the angle at which they scatter. Larger deflections result in a larger variance of electron path lengths, and hence an increase in the variance of the gain. As a result, the rate at which DQE(0) increases as a function of t decreases.

Interpretation of relation between DQE(u) and scintillator thickness at half and full Nyquist

Moving over to half and full Nyquist, the DQE shows an increase as a function of t, until a maximum is reached and the DQE starts to drop. At low t the increase in DQE can be attributed to the increase in DQE(0). The DQE(u) is the product of a frequency dependent part and a frequency independent part, DQE(0). The definition is shown by equation 4.39. The frequency dependent part is rather flat, as can be seen in figure 6.12a, meaning the DQE curve is dominated by DQE(0). The DQE does not decrease at higher frequencies because if the scintillator is this thin, the electrons can hardly scatter, resulting in a small blob size that fits the sample area.

When the thickness increases, so does the electron blob size. At some point the blob will outgrow the area of one pixel, after which the DQE at full Nyquist will decrease as a function of t due too blurring. The DQE at half Nyquist will decrease when the blob outgrows two pixels. The latter happens at a larger thickness, which explains why the peak in the DQE(0.5) versus t curve is broader.

The effect of backscatters on the relation between DQE and scintillator thickness

The hypothesis for this part of the simulation was based on the assumption that the number of electrons that scatter back from the support to the scintillator would increase as a function of scintillator thickness. Figure 6.18 confirms this assumption. Both supports show an increase in backscatters between $t = 1$ μm and $t = 16$ μm, after which the number of backscatters stay constant, taking into account the error bars. The heavier Y support results in more backscatters, which is in line with earlier results (e.g. figure 6.5a).

The impact of the backscatters on DQE(0) is relatively limited. The DQE(0) curve for the simulations with support is slightly lower, because the backscatters introduce more variance in the path lengths inside the scintillator.

The impact of backscatters on the frequency dependent part of the DQE is a lot bigger. The drop in DQE(u) as a function of frequency that was shown in figure 6.13a and 6.14a can be recognized in the relation between DQE(0.5) and t, shown in figure 6.15b. Although decreased in magnitude, the characteristic behavior of the DQE at half and full Nyquist as a function of t remains intact. Furthermore, the optimal thickness does not change significantly.

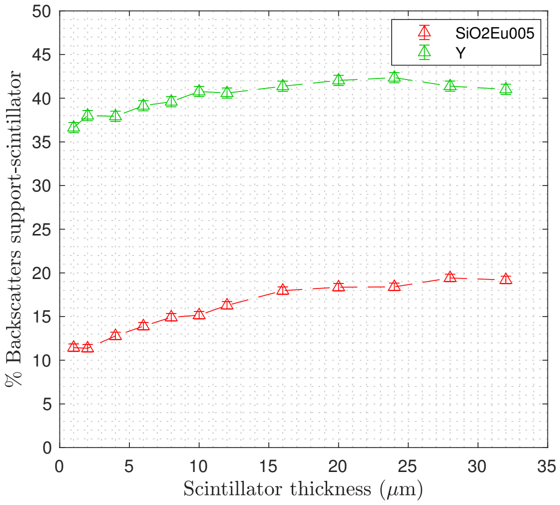

Figure 6.18: Backscatters from the support to the scintillator plotted against the thickness of a P43 scintillator.

Implications for camera design

The findings discussed in this section are advantageous for the process of designing a camera. When an engineer measures a new type of scintillator, it might want to measure different thicknesses in order to maximize the DQE at whatever frequency is of interest. If the engineer decides to try a new support material for this particular scintillator, the measurements to determine the optimal thickness will not have to be redone.

6.4 Numerical aperture

6.4.1 Varying conversion efficiency and scintillator thickness

The DQE(u) and MTF(u) curves for various numerical apertures are plotted in figures 6.19, 6.20 and 6.21 with a conversion efficiency of $\varrho = 0.05$, $\varrho = 0.13$ and $\varrho = 0.50$ respectively. The NA is varied between 0 and 2.3. For the simulation with $\varrho = 0.50$, a larger interval between the NA values is taken, resulting in fewer data points. This is because at this conversion efficiency, the simulation takes a very long time to complete.

Each conversion efficiency has in common that the DQE(u) increases as a function of NA. Furthermore, the DQE(u) profile is rather flat after an initial drop due to backscatters.

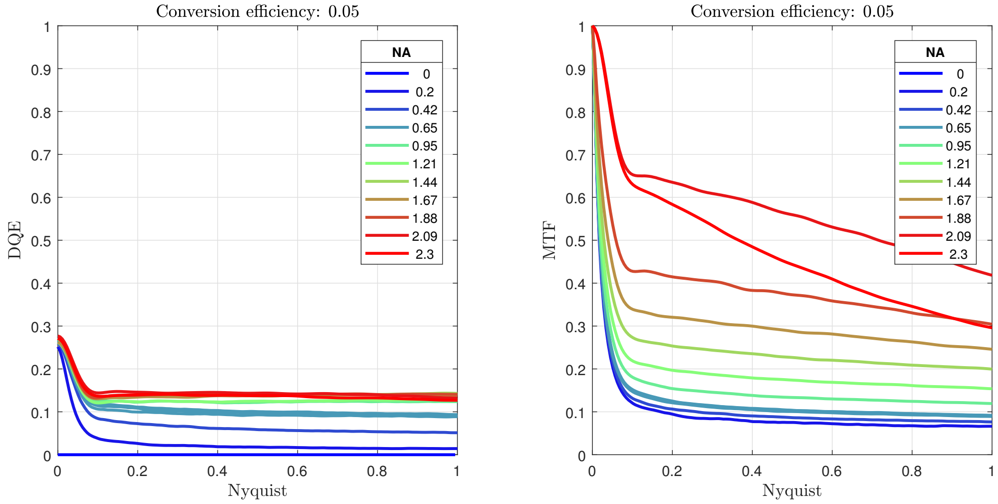

(a) DQE plot.

(b) MTF plot.

Figure 6.19: DQE and MTF vs. spatial frequency in terms of Nyquist frequency. Plotted for a P43 scintillator of 8 μm thickness with conversion factor 0.05. SiO$_2$Eu$_{005}$ support with varying NA, 10^4 electrons.

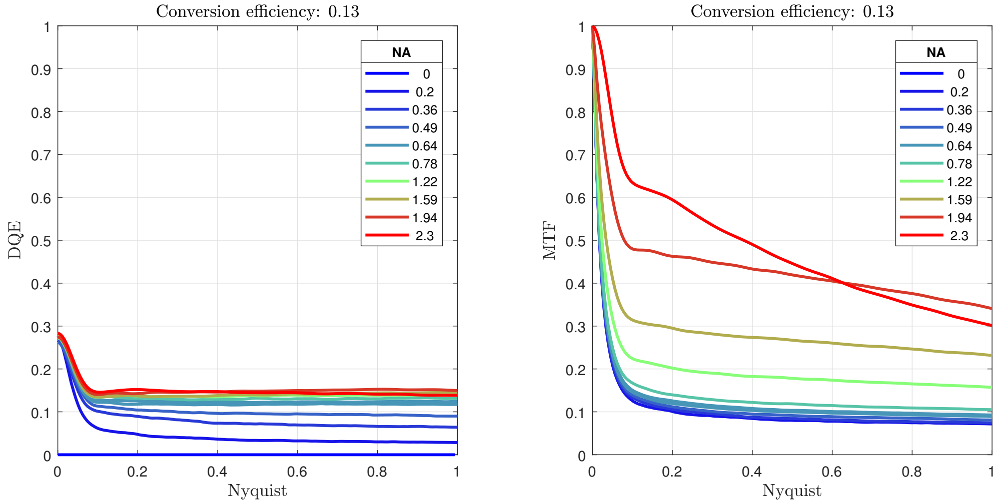

(a) DQE plot.

(b) MTF plot.

Figure 6.20: DQE and MTF vs. spatial frequency in terms of Nyquist frequency. Plotted for a P43 scintillator of 8 μm thickness with conversion factor 0.13. SiO$_2$Eu$_{005}$ support with varying NA, 10^4 electrons.

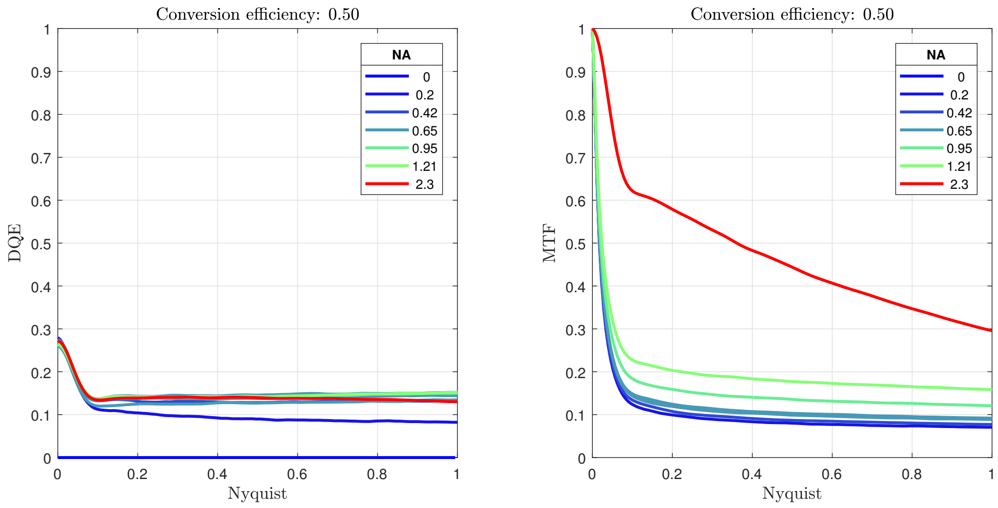

(a) DQE plot.

(b) MTF plot.

Figure 6.21: DQE and MTF vs. spatial frequency in terms of Nyquist frequency. Plotted for a P43 scintillator of 8 μm thickness with conversion factor 0.50. SiO_2Eu_{005} support with varying NA, 10^4 electrons.

Again, the cross sections of the DQE at zero, half and full Nyquist provide more insight, and are plotted in figures 6.22a, 6.22b and 6.23 respectively. At zero Nyquist each conversion efficiency exhibit an initial increase between NA$= 0$ and NA$= 0.2$, after which DQE(0) remains constant. Hence, for NA> 0.2 no correlation exists between DQE(0) and NA. This can be explained by assessing what causes the DQE(0) to change. As already discussed in the results section for the scintillator thickenss, the DQE(0) depends on the ratio between the variance in the gain, and the average gain squared, see equation 6.5. When increasing the numerical aperture, the gain and the variance in the gain increase as well, since for a larger acceptance angle, more photons will find their way to the photon sensor. However, the ratio between the two remains constant, and hence the DQE(0) remains constant. In order to change the ratio, noise has to be added. But the variance in the gain is determined by the electron trajectories, which are independent of NA, and by Poison noise. But as already demonstrated in section 6.3.1, the gain has to be very low ($\Lambda < 3$ phot/elec) in order for the Poison noise to become significant. This is likely the case below NA< 0.2.

At half and full Nyquist, a correlation is present. Each scintillator, with every scintillator having a different ϱ, shows an increase of DQE(u) as a function of NA, until a plateau is reached. When the conversion efficiency is higher, the plateau is reached at a smaller NA. The main difference between half and full Nyquist is the fact that at full Nyquist the DQE decreases slightly towards the maximum NA.

The increase of DQE at half and full Nyquist as a function of NA is in line with the hypothesis. As the acceptance cone becomes wider, fewer photons are internally reflected and subsequently accepted by the FOP elsewhere (like ray 3 in figure 4.3). This decreases the spatial spread of photons, which leads to an increase of the frequency dependent part of the DQE.

Contrary to the hypothesis, the DQE does not show a significant decrease towards the maximum NA, except at full Nyquist where the DQE shows a small decline. The hypothesis stated that accepting photons at nearly every angle, would include photons emitted at a large lateral distance. This was expected to have a negative impact on the DQE. However, this would only have a negative impact if a significant fraction of the photons otherwise would have been absorbed. If the alternative for directly being accepted by the FOP is to travel a large distance before being scattered and accepted by the FOP either way, a larger acceptance angle will not result in a decrease of the DQE.

Hence, photon absorption in a single crystal scintillator is a small effect with a very limited impact on the DQE, according to the simulation.

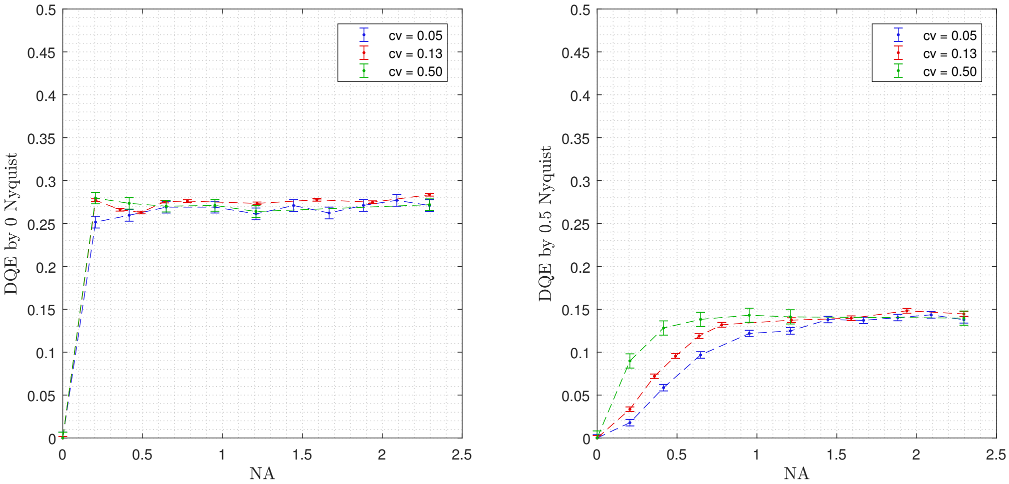

(a) DQE by zero Nyquist.

(b) DQE by half Nyquist.

Figure 6.22: DQE at zero and half Nyquist vs. NA for various conversion efficiency. Plotted for an 8 μm P43 scintillator. SiO_2Eu_{005} support, 10^4 electrons.

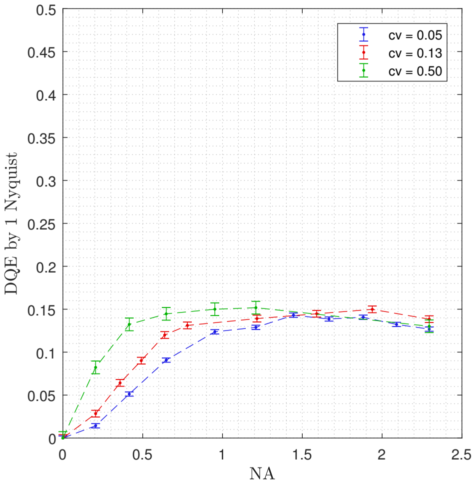

Figure 6.23: DQE at full Nyquist vs. NA for various conversion efficiency. Plotted for an 8 μm P43 scintillator. SiO_2Eu_{005} support, 10^4 electrons.

The penalty for having traveled a large lateral distance is only noticeable at full Nyquist. To understand this, a schematic figure is made to show the relation between NA and sample area. This can be found in figure 6.24, where t is the thickness of the scintillator, a is the width of the sample area and θ_a is the acceptance angle of the fiber optic. This figure shows that the fiber optic has a magnifying property, when the sample area is a, the sample area in fact collects photons coming from an area a' at $z = 0$. In this case $a' = a + 2t\tan\theta_a$. These extra photons introduce blur, but the amount of blur depends on t and θ_a, not on a. Hence the relative amount of blur, expressed by the ratio $2t\tan\theta_a/a$, is twice as large at full Nyquist ($a = 14$ μm) as it is at half Nyquist ($a = 28$ μm). This explains why a decline in DQE as a function of NA is observed at full Nyquist, but not at half Nyquist.

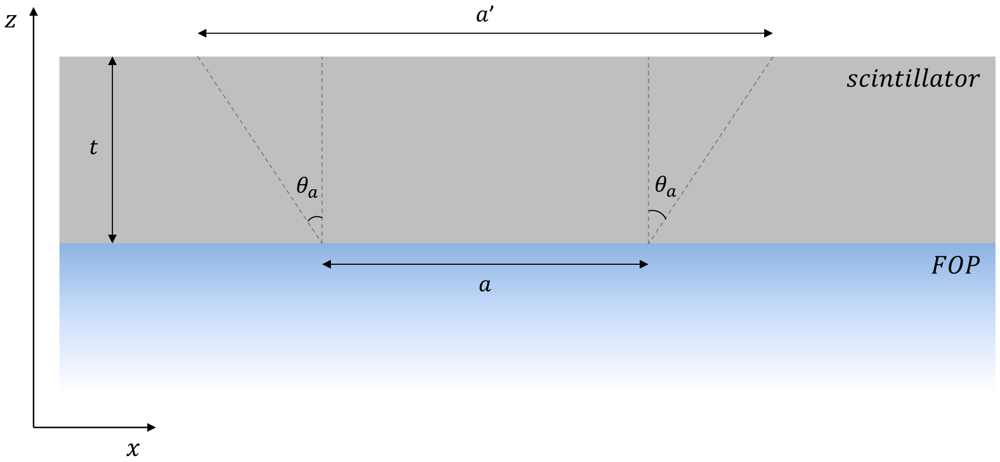

Figure 6.24: Schematic representation of the relation between sample size, NA and scintilltor thickness.

According to these arguments, the relative amount of blur introduced by a large NA would increase for a thicker scintillator. This is confirmed by the results of a simulation where the NA was varied for different scintillators, each with a different thickness. The DQE at full Nyquist is plotted versus NA for different thicknesses in figure 6.25. The optimum NA indeed shifts towards lower NA for increasing scintillator thickness. The variation in height of the maximum peak is in line with the results for varying scintillator thickness. Additional data like the DQE at other frequencies and MTF curves can be found in appendix C.3.

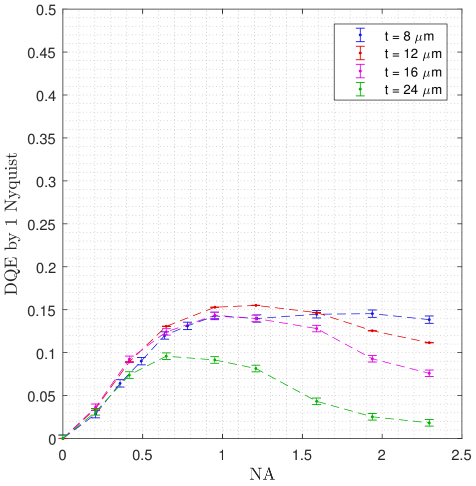

Figure 6.25: DQE at full Nyquist vs. NA for different thicknesses of the P43 scintillator. SiO$_2$Eu$_{005}$ support, 10^4 electrons.

6.5 Grain size

6.5.1 Fill factor

The DQE(u) curves for varying fill factor of an 8 μm P43 scintillator with 1 μm diameter grains are shown in figure 6.26a. The backscatters of the support cause a drop in DQE at low frequency. After this drop the DQE(u) curves remain flat as a function of frequency, as a result, the relation between DQE and the fill factor is identical at half and full Nyquist.

A cross section of the data allows to plot DQE at zero, half and full Nyquist versus the fill factor. The plots at zero and half Nyquist are shown in figures 6.27a and 6.27b. The figures show an increase of DQE as a function of fill factor at both frequencies, until at FF$= 0.6$ the DQE saturates.

To understand the trend shown by DQE as a function of fill factor, a sketch is shown in figure 6.28 of a scintillator with a high fill factor (left) and a low fill factor (right). DQE(0) is fully determined by the ratio of the gain and the variance of the gain. When the fill factor is low, some electrons might penetrate several phosphor grains while other might encounter none. This gives a relatively high variance in the gain. When the fill factor is high, the variance due to this effect is smaller. At this point, the electron scattering is the main cause of the variance in the gain. The simulations of the scintillator material showed that a high Z/ρ results in more electron scattering and hence a low DQE. The scintillator is composed of high Z scintillating grains and low Z fill material. When the fill factor increases, the material between $z = 0$ μm and $z = -8$ μm on average gains a higher Z/ρ. This increases electron scattering and might explain why the growth in DQE(0) as a function of fill factor declines.

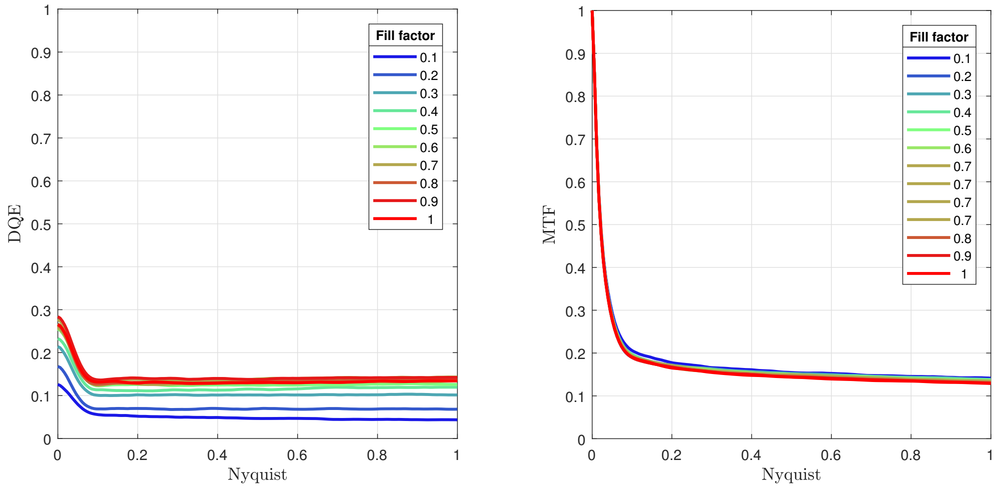

(a) DQE plot.

(b) MTF plot.

Figure 6.26: DQE and MTF vs. spatial frequency in terms of Nyquist frequency. Plotted for a P43 scintillator of 8 μm thickness. Grain size is constant at 1 μm, fill material is SiO_2Eu_{005} with varying fill factor. SiO_2Eu_{005} support, 10^4 electrons.

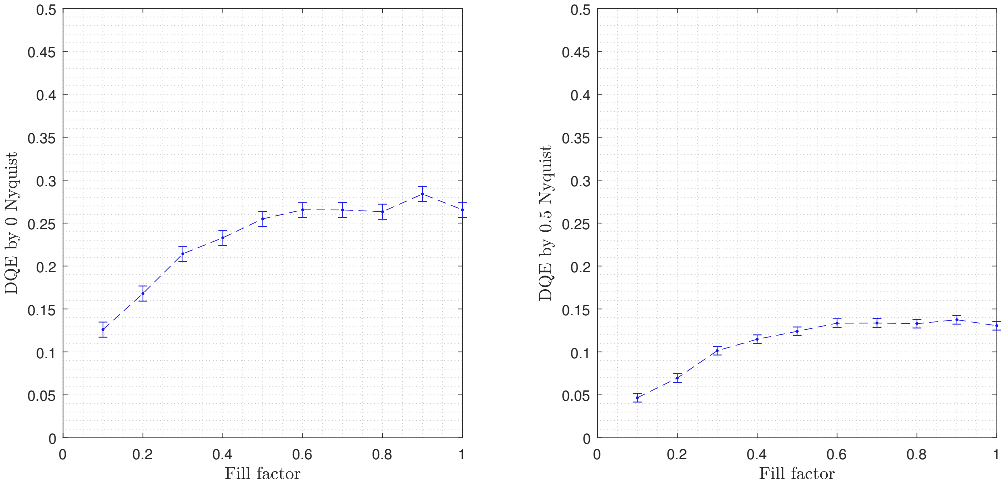

(a) DQE at zero Nyquist.

(b) DQE at half Nyquist.

Figure 6.27: DQE at zero and half Nyquist vs. fill factor with a granulated 8 μm P43 scintillator, grain size 1 μm and SiO_2Eu_{005} fill material. SiO_2Eu_{005} support, 10^4 electrons.

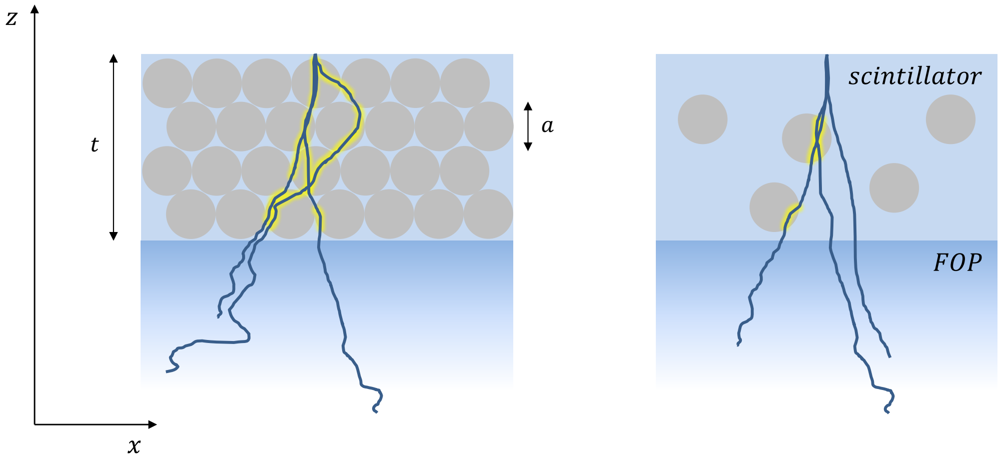

Figure 6.28: Scintillator with a high fill factor (left) and a low fill factor (right). The grey spheres are the phosphor grains. Where the electron trajectory intersects the phosphor grain, the trajectory shows a yellow glow, indicating the emission of photons. The relative variance in the gain is larger when the fill factor is low, while the gain itself decreases.

6.5.2 Grain size

The DQE curves for varying grain size show a similar shape to those for varying fill factor: an initial dip at low frequencies due to backscatters after which the DQE remains constant as a function of frequency. The shape is similar for every grain size, only the height of the DQE curves differs in case of FF$= 0.1$ (figure 6.29a). This again suggests that the difference between the grain sizes is should be found in DQE(0). At FF$= 0.7$, the DQE curves remain constant as the grain size is varied. This is shown in figure 6.30.

These relations can be understood by using arguments similar to the ones used to explain the fill factor. A visual representation of the effect of grain size on the gain is shown in figure 6.31. In this figure, the left scintillator has large grains, while the right scintillator has small grains. Both scintillators have the same fill factor. Obviously, the material distribution in the right scintillator is much more homogeneous. This leads to a smaller variance in the gain. In the scintillator with large grains, an electron could possibly travel almost entirely inside a phosphor grain, while others might travel a significant smaller proportion of their trajectory inside a grain. This increases the variance in the gain. Since the fill factor is equal, the average gain should be equal for every grain size. This is indeed confirmed by the data.

This effect is more pronounced at lower fill factors, since a low fill factors means an even lower homogeneity. At FF$= 0.7$ or higher, varying the grain size does not have a significant impact on the DQE.

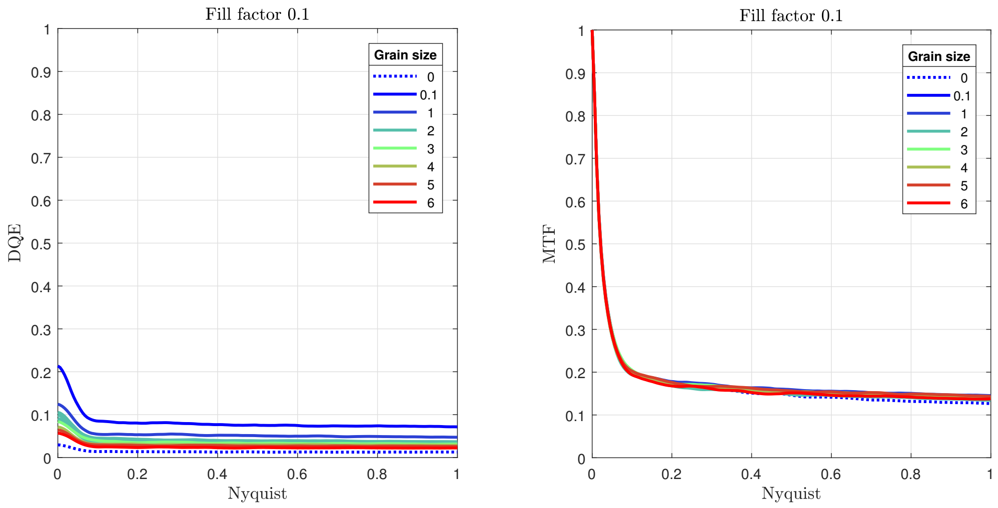

(a) DQE plot.

(b) MTF plot.

Figure 6.29: DQE and MTF vs. spatial frequency in terms of Nyquist frequency. Plotted for a P43 scintillator of 8 μm thickness. Grain size is varying, fill material is SiO_2Eu_{005} with constant fill factor of 0.1. SiO_2Eu_{005} support, 10^4 electrons.

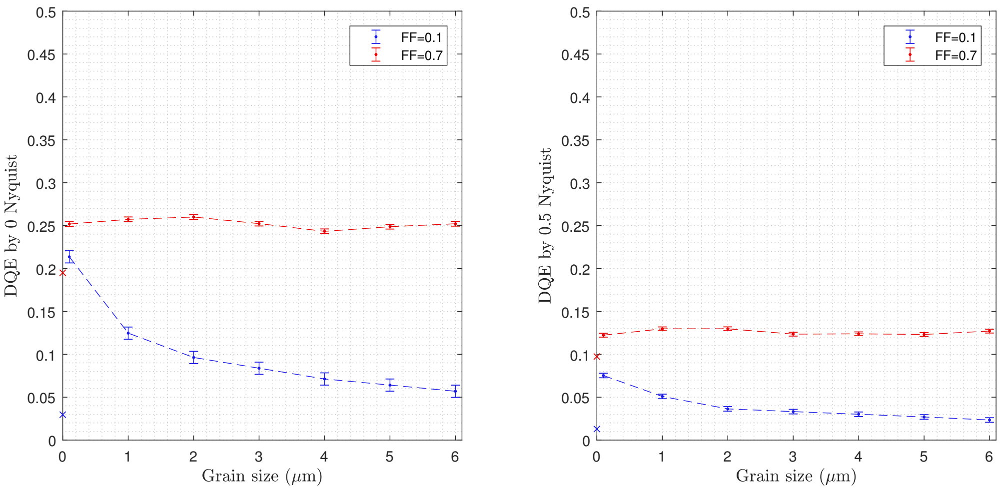

(a) DQE at zero Nyquist.

(b) DQE at half Nyquist.

Figure 6.30: DQE at zero and half Nyquist vs. grain size with a granulated 8 μm P43 scintillator, fill factors of 0.1 and 0.7 with SiO_2Eu_{005} fill material. SiO_2Eu_{005} support, 10^4 electrons. The cross at zero grain size indicates the DQE for a single crystal.

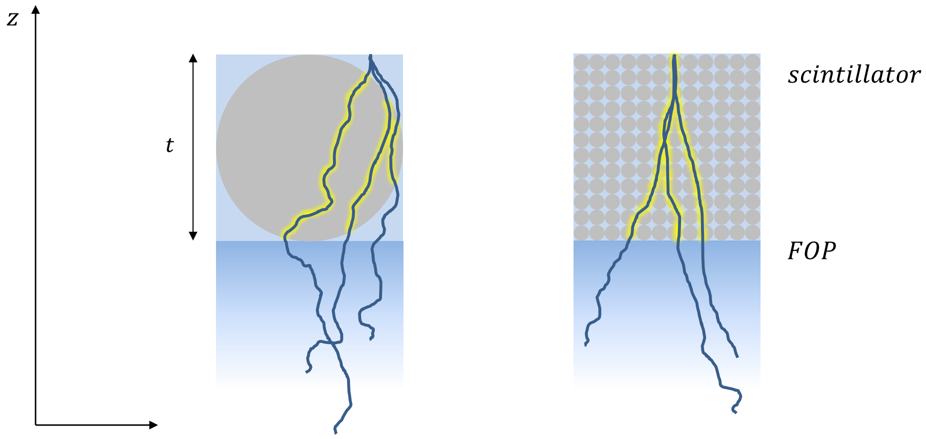

Figure 6.31: Scintillator with a large grain size (left) and a small grain size (right), both scintillators have equal fill factor. The grey spheres are the phosphor grains. Where the electron trajectory intersects the phosphor grain, the trajectory shows a yellow glow, indicating the emission of photons. The variance in the gain is larger when the grains are large. When the grains are small, the material is more homogeneous and the variance in the gain is smaller.

Software flaws

The data resulting from the grain size and fill factor simulations does show some ambiguities. For example, as stated by many papers [7, 8], the phosphor grains are often modeled as spheres. Spheres have a maximum packing density of 0.74 in terms of volume [33], but the software produces results for a finite grain size and FF > 0.74 nonetheless (see figure 6.30a and 6.30b)
Furthermore, one might think that zero grain size refers to a single crystal, yet it is possible to run a simulation with a finite fill factor and zero grain size. The resulting data points are marked with a cross in figure 6.30a and 6.30b.
This is where the lack of appropriate literature makes it hard to interpret these specific data points and to consider them reliable. Hence, the grain size simulations show results that are in line with the existing literature: the DQE is highest for small grain size and high fill factor. However, the parameters show some inconsistencies, which reduces the reliability of these specific results.

6.5.3 Impact of grains on other simulations

As mentioned, most of the simulations treated the scintillator as a single crystal. This was done for three reasons. First, grains would introduce a new level of complexity which would make it harder to interpret the simulation results. Secondly, as was pointed out earlier on this page in the section *Software flaws*, the simulations of grains showed some inconsistencies that reduce the reliability of the results. Furthermore, due to the lack of literature, it is unknown how the grains are exactly modeled. Thirdly, the powdered scintillators used for the CETA camera do not have a fill material between the grains. The grains are closely packed and have a small coating of glue, but for the most part have nothing but vacuum in between them. This could not be simulated by the software.
In electron microscopy, most scintillators are granulated. This raises the question if it is possible to apply the simulation results to the design of a camera with a powdered scintillator.
To answer this question, it is important to understand how a single crystal and a powdered scintillator exactly differ. A schematic figure of each type of scinillator is shown in figure 6.32. The main difference between the two is the scattering behavior of photons. In a single crystal, photons can

travel large distances before being scattered or absorbed by the crystal. Meyer & Kirkland (1998) [1] in fact consider the possibility that a photon is absorbed or scattered in the scintillator before being directly accepted by the FOP to be negligible (ray 1 in figure 6.32). Only photons that are emitted at a large angle and travel large distances because the scintillator acts as a wave guide, have a finite probability to be either absorbed or scattered. And as was concluded in section 6.4, photon absorption is a very small effect, since where it was expected to have an influence on the DQE, it had no effect. Hence, photons travel large lateral distances in a single crystal. In particular at low NA.

In powdered scintillators however, photon scattering and absorption are much more likely to occur. In this type of scintillator, photons are often modeled to deflect at every grain boundary and have a finite probability to be absorbed by every grain [7, 8]. As a result, the trajectory of a photon looks like ray 3 or 4 figure 6.32. The photons will no longer travel large lateral distances (ray 3), and the photons that are emitted near the top surface of the scintillator have a higher probability of being absorbed (ray 4). Both effects are related to the grain size. If the grains are smaller, more scattering and absorption occurs, meaning the photons will not be able to propagate very far from the point of emission. At the same time, smaller grains means photons emitted near the top surface of the scintillator are more likely to be absorbed before reaching the FOP.

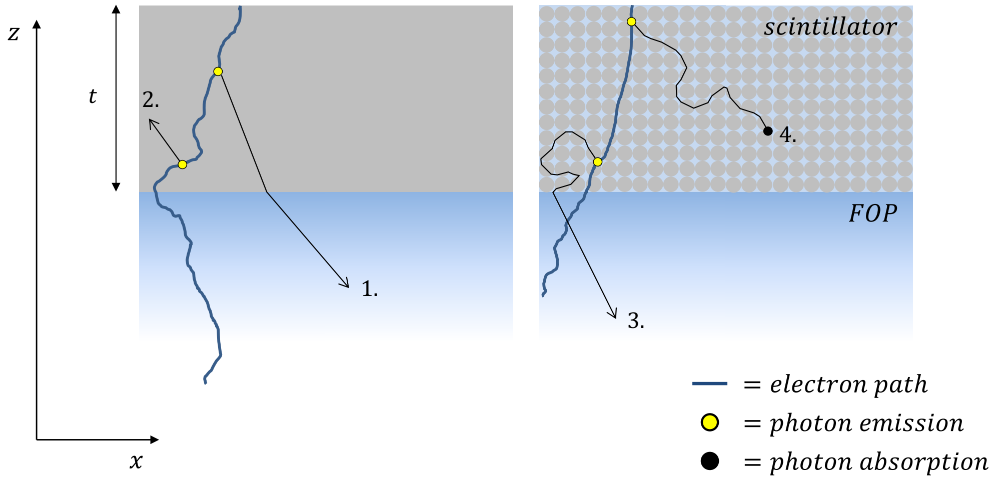

Figure 6.32: A single crystal scintillator (left) and a powdered scintillator (right). Both scintillators show the typical behavior of the photons. The single crystal allows the photons to propagate over large distances before being scattered or absorbed, while the powdered scintillator shows scattering at every grain boundary.

Scintillator thickness

Absorption of these photons might influence the relation between DQE and scintillator thickness. To study this, the DQE at zero, half and full Nyquist is plotted versus the scintillator thickness for a single crystal and powdered scintillator. The plots are shown in figures 6.33a, 6.33b and 6.34. At zero Nyquist, the two scintillators show no significant difference. With a fill factor of $\mathrm{FF} = 0.7$, the electron scattering is expected to be very similar. Furthermore, as was already demonstrated, the scintillator is homogeneous enough at $\mathrm{FF} = 0.7$ and $1\ \mu$m grain size to add no significant amount of variance to the gain. As a result, the $\mathrm{DQE}(0)$ is nearly the same for a single crystal and a powdered scintillator.

At half and full Nyquist, the optimum thickness shifted towards larger t. This is because photons

that are emitted near the top of the scintillator introduce blur that is proportional to the thickness of the scintillator. But since these photons are more likely to be absorbed and scattered in a granulated scintillator, the amount of blur is limited and the DQE is higher. The overall shape of the DQE versus t curve remains intact since the electron scattering is not altered much.
Hence, the exact value of the optimum thickness is different for both types of scintillators, but the trend is the same. The conceptual insights that resulted from the simulations keep their value.

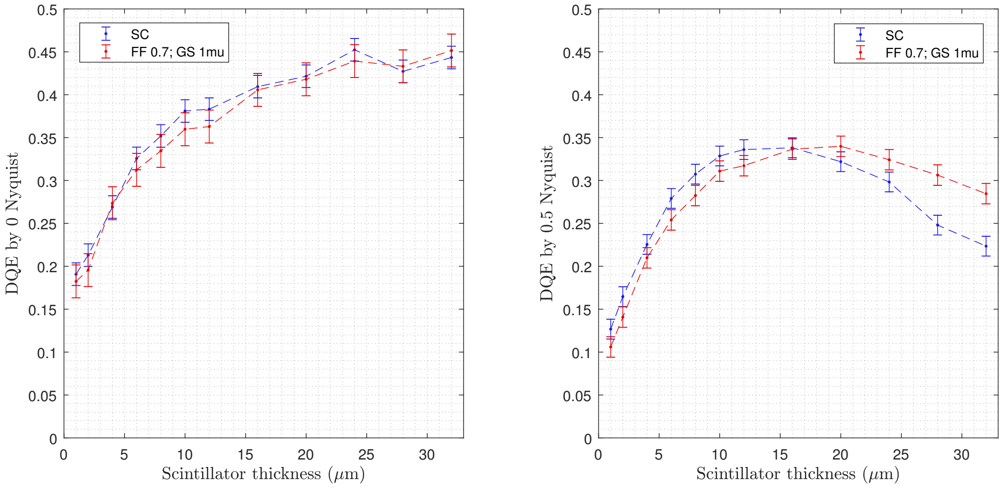

(a) DQE at zero Nyquist.

(b) DQE at half Nyquist.

Figure 6.33: DQE at zero and half Nyquist vs. thickness for a single crystal (SC) and powdered scintillator, fill factors of 1.0 and 0.7 respectively with SiO_2Eu_{005} fill material. No support, 10^4 electrons.

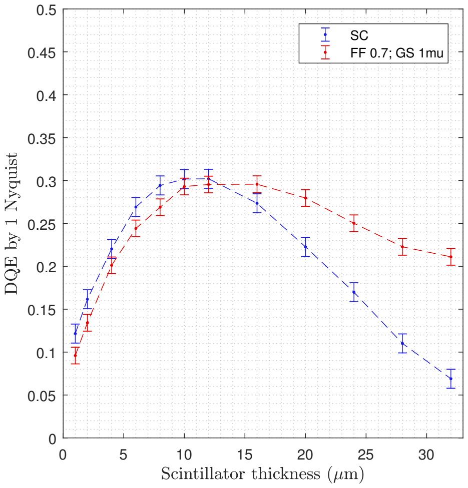

Figure 6.34: DQE at full Nyquist vs. thickness for a single crystal (SC) and powdered scintillator, fill factors of 1.0 and 0.7 respectively with SiO_2Eu_{005} fill material. No support, 10^4 electrons.

Scintillator and support material

The scintillator and support material simulations were focused on electron scattering, while the scintillator grains mainly affects photon scattering. But is has to be noted that the introduction of grains causes the average Z and ρ of the scintillator to change. Since SiO_2Eu_{005} was used as a fill material, which has a lower effective Z than any of the scintillator materials tested, the average Z of the scintillator would decrease. This would result in a small shift of the data, but the qualitative trend would remain the same.

Numerical aperture

These simulations are expected to suffer most under the introduction of grains in the scintillator. After all, the relation between DQE and NA relies heavily on the fact that a larger NA means a larger acceptance angle. A larger acceptance angles allows photons coming from a large distance to be accepted by the FOP. The angle under which the photon is emitted, θ, is equal to the angle under which the photon approaches the FOP, $\theta' = \theta$ (see the scintillator on the left in figure 6.32). However, a granulated structure causes the photon to scatter at every grain boundary (right scintillator in figure 6.32). As a result, the photon might be emitted at an angle θ, but can approach the FOP with an entirely different angle $\theta' \neq \theta$. Hence, the relation between the numerical aperture and the amount of blur due to lateral displacement of the photon is no longer valid.

In order to verify this hypothesis, simulation are run to compare the DQE of a single crystal and granulated scintillator for two different numerical apertures. The results can be found in figure 6.35. At NA $= 1.22$ (red curves), there is no significant difference between the single crystal and the granulated scintillator. At NA $= 0.36$ (blue curves), the granulated scintillator shows a slightly better DQE, but the difference is very close to the magnitude of the error bars shown by NA simulations earlier.

The fact that there is such a small difference in DQE where a significant impact of the grains was expected, reduces the overall confidence that the simulation software produces reliable results when it comes to grains. The specific impact of phosphor grains on the results of the NA simulations in a single crystal remains unknown. It seems unlikely that these results can be simply translated to a granulated scintillator system, since the photons behave fundamentally different.

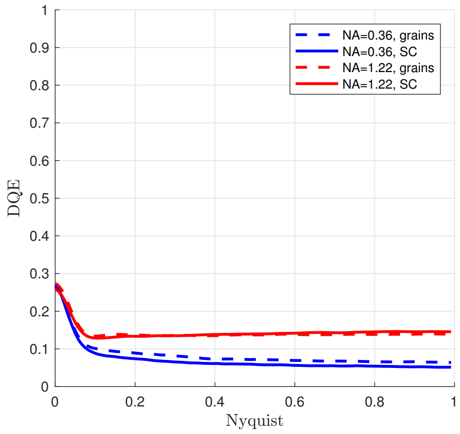

Figure 6.35: DQE at full Nyquist vs. thickness for a single crystal (SC) and powdered scintillator, fill factors of 1.0 and 0.7 respectively with SiO_2Eu_{005} fill material. No support, 10^4 electrons.

6.6 Experiments

The EDX data that can be found in appendix C.4 shows that the FOP's have a lot of elements in common. This is not surprising since every fiber optic is for the most part made of glass, and other elements are added to tune certain properties like NA, radiation hardness and x-ray shielding. An important indicator of the electron scattering behavior in the fiber optic is the presence of Pb. Some suppliers avoid the use of Pb and use the significantly lighter La and Ba. The exact composition of the fiber optic can be derived from the height of the peaks in the emission spectrum. Unfortunately some peaks are cut-off. This is why this analysis is focused on the mere presence of Pb, in order to get an indication of the effective Z and ρ. This is listed in table 6.5, together with other properties like radiation hardness (RH) and numerical aperture (NA).

The DQE curves for each support are shown in figure 6.36. The MTF curve and the results for the 200 keV measurements can be found in appendix C.5.1. One might note that these curves contain a lot more noise than the DQE curves of the simulations. This is due to artifacts introduced by the measurement setup. For example, the scintillator is slightly tilted or the FOP is not completely flat. A considerable part of the noise can be reduced by taking multiple images and calculate the average image. This was done during these measurements. Furthermore, the larger the exposure area, the more reliable the measurement. These FOP samples however where small compared to the CMOS sensor, limiting the maximum exposure area. In addition, the FOP's where varying in size and thickness, which adds another source of uncertainty. In particular the variance in DQE(0) between the FOP's is larger than expected. The DQE(u) curve scales with DQE(0), hence a large uncertainty in DQE(0) imposes a large uncertainty at every frequency. Hence, one should be cautious when drawing conclusions from these measurements.

Table 6.5: Table of the measured FOP's. The first column reads their label, the second column whether EDX data is available, the third column provides information on the numerical aperture and the fourth on whether the FOP is radiation hard. The fifth label indicates the presence of lead.

Label	EDX data	NA	RH	Pb
Eagle	Yes	2.3	No	Yes
Supplier 1	Yes	2.3	Yes	No
Supplier 2	Yes	2.3	No	Yes
Supplier 3	Yes	2.3	Yes	No
Supplier 4	Yes	2.3	Yes	No
Supplier 5	No	1.5	No	Unknown

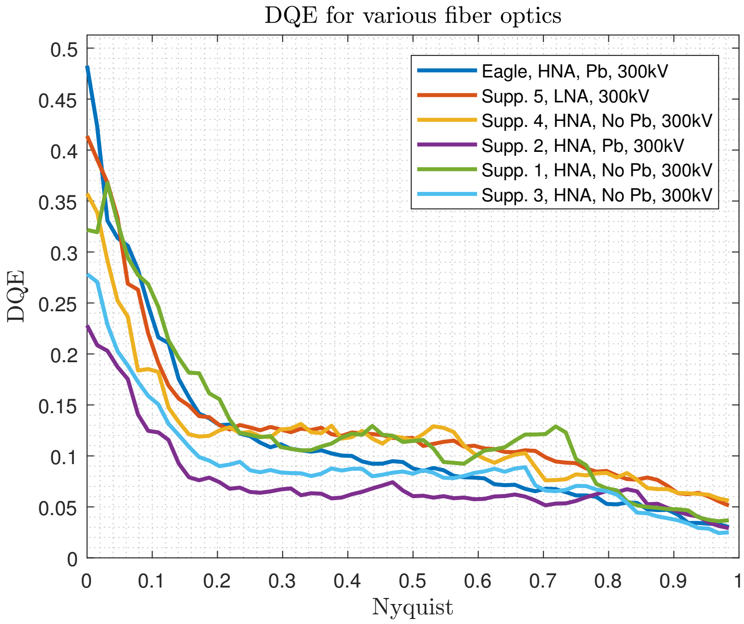

Figure 6.36: DQE of the measured FOP's at 300 keV.

In spite of the fact that the reliability of the data is limited, some qualitative observations can be made. Based on the simulation results, one would not expect to see a large difference in DQE for a FOP with NA $= 1.5$ and NA $= 2.3$. It is hard to make a good comparison between the DQE curve of the FOP with low NA and the curves with high NA, since no EDX measurement has been done on the low NA sample.

A comparison that can be made is between the FOP's with and without Pb. The FOP's without Pb consistently perform better than the FOP's enriched with Pb. The best performers are the FOP's deliverd by supplier 1, 4 and 5. None of them contains Pb, although this is not measured for supplier 5. Two out of the three worst performers contain Pb. Avoiding Pb in the FOP leads to a lower average atomic number. The simulations demonstrate that this leads to a performance improvement, and the experiments show results that are in accordance with these simulations.

Chapter 7

Conclusion

7.1 Simulations & experiments

Simulations and experiments have been carried out to study the possibilities of improving the indirect detection camera. Furthermore, these simulations aimed to develop a deeper understanding of the scattering process of electrons and photons in the scintillator and fiber optic plate (FOP).
Six sub-questions have been defined in section 1.3. Each sub-question is meant to isolate an aspect of the camera design. Simulations have been done for each particular design aspect. The camera performance is quantified with the spatial frequency dependent detective quantum efficiency, DQE(u). The conclusions that can be drawn from the simulation results are presented in the same order as the sub-questions were defined.

1. How is the chemical composition of the fiber optic plate related to the camera performance?

The camera performance shows a significant U-shaped correlation with the atomic number of the support, Z_{supp}, and the product of the atomic number and the mass density of the support, $Z_{supp} \cdot \rho_{supp}$. This means that in order to improve the camera performance, the effective atomic number of the fiber optic should be either very low ($Z_{supp} \sim$ 10), or very high ($Z_{supp} \sim$ 80). Since a high atomic number often results in a low optical transparency, a low atomic number for the fiber optic is the most promising possibility of improving the camera performance. One way of achieving this result would be omitting the use of lead in the fiber optic.
In practice, there are always materials added to the glass of the fiber optic to achieve the desired numerical aperture. But a fiber optic of 100% glass would in theory result in a performance improvement of $40 - 60\%$, when compared to a fiber optic with 20% lead. According to the simulations, a fiber optic with lead has DQE$(0.5) = 0.085 \pm 0.005$, while a pure glass fiber optic has DQE$(0.5) = 0.14 \pm 0.002$.

2. How is the chemical composition of the scintillator related to the camera performance?

The camera performance shows a significant correlation with the ratio of the atomic number and mass density of the scintillator, Z_{scint}/ρ_{scint}. The results show that the camera performs best when the Z_{scint}/ρ_{scint} ratio is low, i.e. $Z_{scint}/\rho_{scint} \sim$ 3, this would give DQE$(0.5) \approx 0.4$ according to the simulation without support. When this ratio increases, more blur is introduced and the camera performance will decrease. The currently used P43 scintillator has $Z_{scint}/\rho_{scint} = 4.4$, which under the simulated conditions gives DQE$(0.5) = 0.30 \pm 0.01$.
Although the relation between camera performance and scintillator material is an interesting insight, it is hard to translate this result to a practical recommendation. This is because there are a lot more parameters that restrict the choice of a scintillator. Each scintillator material has a specific

conversion efficiency, emission peak in the spectrum, decay time, and so on. All these aspects have to be taken into account when choosing the scintillator material. A scintillator can have a low Z_{scint}/ρ_{scint} ratio, but if it does not check all the boxes in terms of the properties just mentioned, it cannot be used as a substitute of the currently used P43 scintillator. During this study, no realistic scintillator has been found that could compete with the P43 scintillator when every aspect is taken into account.

3. How is the thickness of the scintillator related to the camera performance?

The camera performance shows correlation with the scintillator thickness with its maximum between $t = 10$ μm and $t = 24$ μm. As pointed out in the introduction section, these simulations are intended to discover trends and find directions in which camera improvements can be found. It is hard to predict based on the simulations whether increasing the scintillator thickness from the currently used $t = 8$ μm to e.g. $t = 12$ μm would give a considerable improvement. The peak is rather flat though, so it probably will not do any harm either.
A qualitative conclusion that can be drawn from the data is that the optimal thickness does not show a significant shift for different fiber optics. This is an important results because it means that once the scintillator is fully optimized in terms of its thickness, one is free to try different fiber optics without having to re-calibrate the optimal scintillator thickness.

4. What is the relationship between the optical properties of the fiber optic and the camera performance?

The camera performance shows an increase as a function of the numerical aperture, until it saturates at NA ≈ 1.2. This is for a standard P43 scintillator. Increasing the conversion efficiency causes the camera performance to saturate at a smaller numerical aperture. For thicker scintillators, the camera performance decreases at high numerical apertures.
However, the results of this simulation apply to a single crystal scintillator. A comparison with grain size simulations show inconsistent results. Therefore, it is not possible to confidently state that the results of this simulation can be applied to a granulated scintillator. The insights that followed from this simulation can therefore only be used when working with a single crystal scintillator.

5. How is the scintillator grain size and fill factor related to the camera performance?

These simulations have shown that the camera performance is best for small grain size or high fill factor. This is in accordance with the existing literature [7, 8]. Nonetheless, the data does show some ambiguities. For example a simulation result with a 100% fill factor while the theoretical maximum packing density of spheres is 74%. This reduces the reliability of these simulations, and is the reason why no design recommendation is derived from these simulations.
Based on the theory, the introduction of grains in the model is not expected to have a significant impact on the qualitative results of the other simulations.

6. How do the simulation results compare to experimental data?

The performance measurement of 6 different fiber optics showed that avoiding the use of lead in the fiber optic consistently gives a better performance. Two out of the three best performing fiber optics did not contain lead, while for the third fiber optic it was not measured. This increases the confidence in the conclusion that omitting lead gives a camera performance improvement.
Due to a lack of data concerning the chemical composition of the low numerical aperture fiber optic, it was not possible to verify the numerical aperture simulations.

7.2 Outlook

A next step could be to use the conclusions that were derived from the simulations in this study, and perform an experiment to see if the predicted performance improvement is indeed possible. Another possibility for a follow-up study could be to further develop the understanding of the photon scattering. This study focused on the electron scattering in the scintillator and the support. The model for photon scattering was known for a single crystal, not for granulated scintillators. It would be interesting to understand how photon scattering between the scintillator grains could be modeled. To perform simulations on this aspect, one would probably have to develop a new simulation. This would require a lot of effort, but at the same time opens up opportunities to study radically different camera designs that where not possible to simulate with the Monte Carlo software package used in this study.

References

[1] Meyer, R., & Kirkland, A. (1998). The effects of electron and photon scattering on signal and noise transfer properties of scintillators in CCD cameras used for electron detection. *Ultramicroscopy, 75*, 23-33.

[2] Wagner, R., & Voorhout, W. (2017). Nobelprijs voor de Scheikunde 2017. *Nederlands Tijdschrift voor Natuurkunde, 83*(12), 401-403.

[3] Kuijper, M., Van Hoften, G., Janssen, B., Geurink, R., De Carlo, S., Vos, M., . . . Storms, M. (2015). FEI's direct electron developments: Embarking on a revolution in cryo-TEM. *Journal of Structural Biology, 192*, 179-187.

[4] Joy, D. C. (1995). *Monte Carlo Modeling for Electron Microscopy and Microanalysis*. New York, United States: Oxford University Press.

[5] Nikl, M. (2006). Scintillation detectors for x-rays. *Measurement Science and Technology, 17*, 37-54.

[6] Lecoq, P., Annenkov, A., Gektin, A., Korzhik, M., & Pedrini, C. (2006). *Inorganic Scintillators for Detector Systems.* Heidelberg, Germany: Springer.

[7] Liaparinos, P. F., Kandarakis, I. S., Cavouras, D. A., Delis, H. B., & Panayiotakis, G. S. (2006). Modeling granular phosphor screens by Monte Carlo methods. *Med. Phys., 33*(12), 4502-4514.

[8] Poludniowski, G. G., & Evans, P. M. (2013). Optical photon transport in powdered-phosphor scintillators. Part 1. Multiple-scattering and validity of the Boltzmann transport equation. *Med. Phys., 40*(4), 1-11.

[9] Nikl, M. (2005). Energy transfer phenomena in the luminescence of wide band-gap scintillators. *Physics Status Solidi, 202*(2), 201-206.

[10] Rodnyi, P. A., Dorenbos, P., & Van Eijk, C. W. E. (1995). Energy Loss in Inorganic Scintillators. *Phys. Status Solidi, (b) 187*, 15-29.

[11] Boggs, S., & Krinsley, D. (2006). *Application of Cathodoluminescence Imaging to the Study of Sedimentary Rocks.* Cambridge, United Kingdom: Cambridge University Press.

[12] Shockley, W. (1961). Problems Related to p-n Junctions in Silicon. *Solid-State Electronics, 2*(1), 35-67.

[13] Elango, M. A. (1991). *Elementary Inelastic Radiation-Induced Processes*. New York, United States: American Institute of Physics.

[14] Rose, A. (1948). The Sensitivity Performance of the Human Eye on an Absolute Scale. *Journal of the Optical Society of America, 38*(2), 196-208.

[15] Rose, A. (1953). Quantum and Noise Limitations of the Visual Process. *Journal of the Optical Society of America, 43*(9), 715-716.

[16] Burgess, A. E. (1999). The Rose model, revisited. *Journal of the Optical Society of America, 16*(3), 633-646.

[17] Cunningham, I. A., & Shaw, R. (1999). Signal-to-noise optimization of medical imaging systems. *Journal of the Optical Society of America A, 16*(3), 621-632.

[18] Metz, C. E., & Doi, K. (1979). Transfer Function Analysis of Radiographic Imaging Systems. *Physics in Medicine & Biology, 24*(6), 1079-1106.

[19] Michelson, A. A. (1927). *Studies in optics*. Chicago, United States: The University of Chicago Press.

[20] Chatfield, C. (1989). *The Analysis of Time Series - An Introduction* (4th ed.). London, UK: Chapman and Hall.

[21] Saleh, B. E. A., & Teich, M. C. (1991). Fundamentals of Photonics. New York, United States: John Wiley & Sons, Inc.

[22] Dainty, J. C., & Shaw, R. (1973). *Image Science*. London, UK: Academic Press.

[23] Phillips, C. L., Parr, J. M., & Riskin, E. A. (2008). *Signals, Systems, and Transforms*. (4e ed.). Harlow, Groot-Brittannië: Pearson Education.

[24] Metropolis, N., & Ulam, S. (1949). The Monte Carlo Method. *Journal of the American Statistical Association, 44*(247), 335-341.

[25] Myklebust, R. L., Newbury, D. E., & Yakowitz, H. (1976). Use of Monte Carlo Calculations in Electron Probe Microanalysis and Scanning Electron Microscopy. *National Bureau of Standards, 460*, 105-128.

[26] Joy, D. C., & Luo, S. (1989). An Empirical Stopping Power Relationship for Low-Energy Electrons. *Scanning, 11*, 176-180.

[27] Meyer, R., & Kirkland, A. (2000). Characterisation of the Signal and Noise Transfer of CCD Cameras for Electron Detection. *Microscopy Research and Technique, 49*, 269-280.

[28] De Ruijter, W. J. (1995). Imaging Properties and Applications of Slow-Scan Charge-Coupled Device Cameras Suitable for Electron Microscopy. *Micron, 26*(3), 247-275.

[29] Zweig, H. J. (1965). Detective Quantum Efficiency of Photodetectors with Some Amplification Mechanisms. *Journal of the Optical Society of America, 55*(5), 525-528.

[30] Rabbani, M., Shaw, R., & Van Metter, R. (1987). Detective quantum efficiency of imaging systems with amplification and scattering mechanisms. *Journal of the Optical Society of America A, 4*(5), 895-901.

[31] Malitson, I. H. (1965). Interspecimen comparison of the refractive index of fused silica. *J. Opt. Soc. Am., 55*, 1205-1208.

[32] Taylor, M.L., Smith, R.L., Dossing, F., & Franich, R.D. (2012). Robust calculation of effective atomic numbers: The Auto-Zeff software. *Medical Physics 39*, 1769-1778.

[33] Conway, J. H., & Sloane, N. J. H. (1998). *Sphere Packings, Lattices and Groups* (3e ed.). New York, United States: Springer.

[34] James, F. (2012). *Statistical methods in experimental physics* (2nd ed.). New Jersey, USA: World Scientific.

Appendix A

Mathematical theorems

A.1 Fourier transform and convolution theory

The Fourier transform in two dimensions of a function $f(x,y)$ gives its spectrum. It is defined as [18]

$$\widehat{f}(u,v) = \mathcal{F}\{f(x,y)\} = \iint_{-\infty}^{\infty} f(x,y)\exp\left[-i2\pi(ux+vy)\right]\mathrm{d}x\mathrm{d}y. \tag{A.1}$$

The inverse Fourier transform is given by

$$f(x,y) = \mathcal{F}^{-1}\{\widehat{f}(u,v)\} = \iint_{-\infty}^{\infty} \widehat{f}(u,v)\exp\left[+i2\pi(ux+vy)\right]\mathrm{d}u\mathrm{d}v. \tag{A.2}$$

The convolution product of two functions $f(x)$ and $g(x)$ is written as

$$f(x) * g(x) = \int_{-\infty}^{\infty} f(\xi)g(x-\xi)\mathrm{d}\xi. \tag{A.3}$$

In two dimensions, the product reads

$$f(x,y) ** g(x,y) = \iint_{-\infty}^{\infty} f(\xi,\eta)g(x-\xi,y-\eta)\mathrm{d}\xi\mathrm{d}\eta. \tag{A.4}$$

The spectrum of the convolution of two functions is equal to the product of their spectra:

$$\mathcal{F}\{f(x,y) ** g(x,y)\} = \widehat{f}(u,v)\widehat{g}(u,v). \tag{A.5}$$

A.2 Parseval's theorem

If $f(x,y)$ is a function depending on variables x,y and $\widehat{f}(u,v)$ is its Fourier transform depending on the corresponding reciprocal variables, Parseval's theorem states that the integrals of their absolute squares are equivalent [21]:

$$\iint_{-\infty}^{\infty} |f(x,y)|^2\mathrm{d}x\mathrm{d}y = \iint_{-\infty}^{\infty} \left|\widehat{f}(u,v)\right|^2\mathrm{d}u\mathrm{d}v. \tag{A.6}$$

Appendix B

Documentation software

B.1 Simulation parameters

In this appendix all the simulation parameters are explained that are listed in the graphical user interface of the software, see figure 5.1. The parameters with an asterisk were not documented by Meyer and Kirkland (1998) [1].

Energy (keV) The energy of the incident electrons.

Incident angle The angle the incident electron beam makes relative to the normal of the scintillator.

Scintillator (μm) The thickness and material of the scintillator. The choice of material imposes the atomic number and mass density. The scintillation efficiency can be chosen manually.

Grain size The typical grain size in a powdered scintillator is 1-10 μm [8]. A zero grain size resembles a single crystal. Since the physical model behind granulated scintillators used by the software is not known, most of the simulations are executed with zero grain size. Although the P43 scintillator that is actually used is granulated and not a single crystal, this method allows to fully understand the results of the simulations. Whereas the introduction of grains turns the model into a black box with no knowledge of the used model. The consequences of modeling single crystals instead of powders will be covered by the discussion section.

Fill factor Ratio of scintillator grains and fill material. In literature also referred to as packing density.

Fill material Material in between the scintillator grains. Also known as binding material, implicating adhesive properties.

Coating (μm) Coating on top of the scintillator, usually aluminum. The aluminum coating serves as a conductive layer that prevent charge build-up.

Support (μm) The support refers to the material underneath the scintillator. The fiber optic, in this case.

Photon absor. mfp* Mean free path of photons before attenuated by the scintillator. Meyer and Kirkland have not provided literature on this parameter. Though photon absorption is crucial in modeling scintillators, simulations with absorption mfp varying from 10^{-9} meter to 10^{-3} meter have not shown significant differences. These simulations were done with a single crystal model ($\textit{grain size} = 0$). Because of this, the default value of this parameter was adopted for the simulations, $\textit{photon absor. mfp} = 0$. The same holds for the photon scatt. mfp.

Photon scatt. mfp* Mean free path of photons before scattered in the scintillator.

Refractive index*: n_{scint}, n_{supp}

Optical blurring radius*; $\alpha = 0^o$, $\alpha = 30^o$

Conversion factor The efficiency by which the energy of the primary electron is converted into photons. This corresponds to the scintillation efficiency ϱ, given by equation 2.4.

Aperture semiangle The aperture semiangle of the fiber optic is related to the numerical aperture. This angle corresponds to θ_t in figure 2.8. The angle can be calculated using equation 2.15. For most simulations, NA$= 1$ is taken. With a P43 scintillator with refractive index of $n = 2.3$ [7], this results in a semiangle of 26^o.

Width of aperture edge*

Photon energy (eV) For the photon energy, the default value is chosen, 2.2 eV. This is very close to the photon energy peak in the emission spectrum of a P43 scintillator. A P43 scintillator has an emission peak at 540 nm [5], which is equal to 2.3 eV.

Upper surf. refl. ratio Fraction of photons reflected at the top surface of the scintillator with an angle within the acceptance cone. In the actual camera design, an aluminum coating is applied to the top surface of the scintillator. In most of the simulations, this is left out to simplify the model and make the results easier to interpret. However, the reflective ratio is chosen to be 1 either way.

Lower surf. refl. ratio Fraction of photons reflected at the bottom surface of the scintillator with an angle within the acceptance cone. This does not include photons that encounter total internal reflection, since those photons have an angle outside the acceptance cone. This fraction is chosen to be 0.

Focus plane z (μm) The plane of focus of the fiber optic. The bottom of the scintillator is chosen to be the plane of focus, following Meyer and Kirkland (1998) [1].

k sampling distance (1/mm) Sampling distance is measured in frequency, and determines the number of data points in the DQE(k) plot. It has to be between 0.05 mm^{-1} and 10 mm^{-1}. More data points results in a longer computation time. However, one should have enough data points to acquire information of the DQE around zero, half and full Nyquist. A sampling distance of 0.2 mm^{-1} has proven to be a good trade-off between number of data points and computation time.

max. k (1/mm) The maximum frequency is the Nyquist frequency given by equation 3.36. Given that the pixels of the CMOS sensor are 14 μm large, the Nyquist frequency is 35.71 mm^{-1}.

Fraction of photons scattered diffuse This fraction refers to f_s, defined by equation 4.29. When a photon is emitted it can either be emitted under an angle that allows it to be directly accepted by the support, or it can be internally reflected at the scintillator-support interface. When the latter occurs, the scintillator acts as a wave guide, until the photon isotropically scatters. The fraction of photons scattered diffuse is the ratio between the two possibilities, and depends on the refractive indexes of the support and scintillator. In the case of a glass support (SiO_2, $n = 1.44$ [31]) and a P43 scintillator (Gd_2O_2S, $n = 2.3$ [5]) this ratio is $f_s = 3.54$.

Mean radius of diffuse spreading (μm) The lateral distance that the photons displace through diffuse spreading is exponentially distributed. The mean is manually chosen. Meyer and Kirkland (1998) [1] chose a mean radius 500 μm for a single crystal YAG scintillator, this value is adopted for these simulations.

 # Trajectories Number of simulated electrons. More electrons give a better result. The MTF and DQE curves contain less noise and are easier to reproduce. However, more electrons result in a higher computation time. For DQE simulations, 10^4 electrons are simulated. To get a sense of the accuracy of these simulations, the data points of interest are simulated 4 times with 10^4 electrons. The errorbar indicates the spread in these outcomes.

Appendix C

Data

C.1 Support material

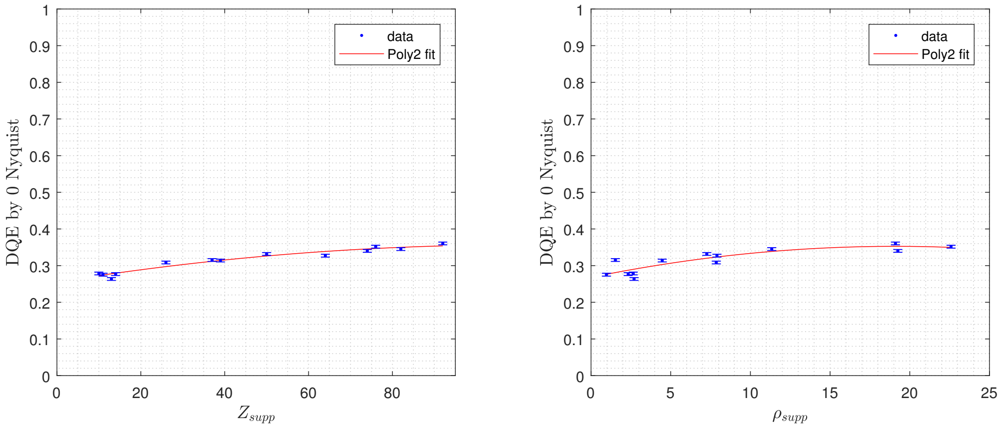

(a) DQE by zero Nyquist vs. Z_{supp}.

(b) DQE by zero Nyquist vs. ρ_{supp}.

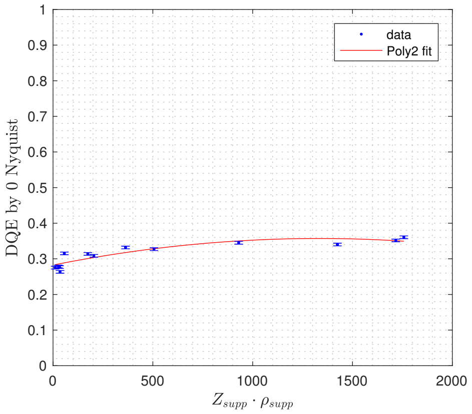

(c) DQE by zero Nyquist vs. $(Z/\rho)_{supp}$.

Figure C.1: DQE by zero Nyquist versus the atomic number, mass density and atomic number times the mass density of the support material.

C.2 Scintillator material

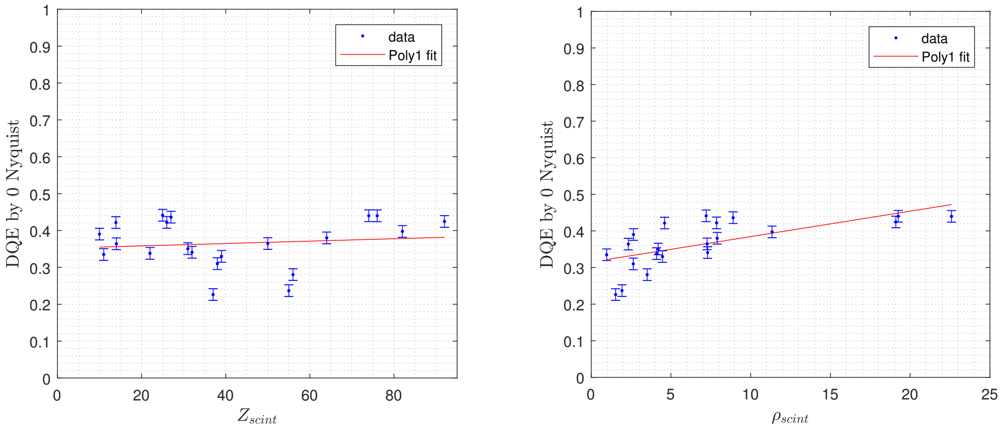

(a) DQE by zero Nyquist vs. Z_{scint}.

(b) DQE by zero Nyquist vs. ρ_{scint}.

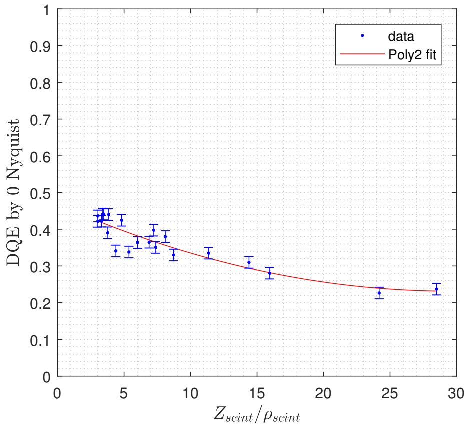

(c) DQE by zero Nyquist vs. $(Z/\rho)_{scint}$.

Figure C.3: DQE by zero Nyquist versus the atomic number, mass density and atomic number times the mass density of the support material.

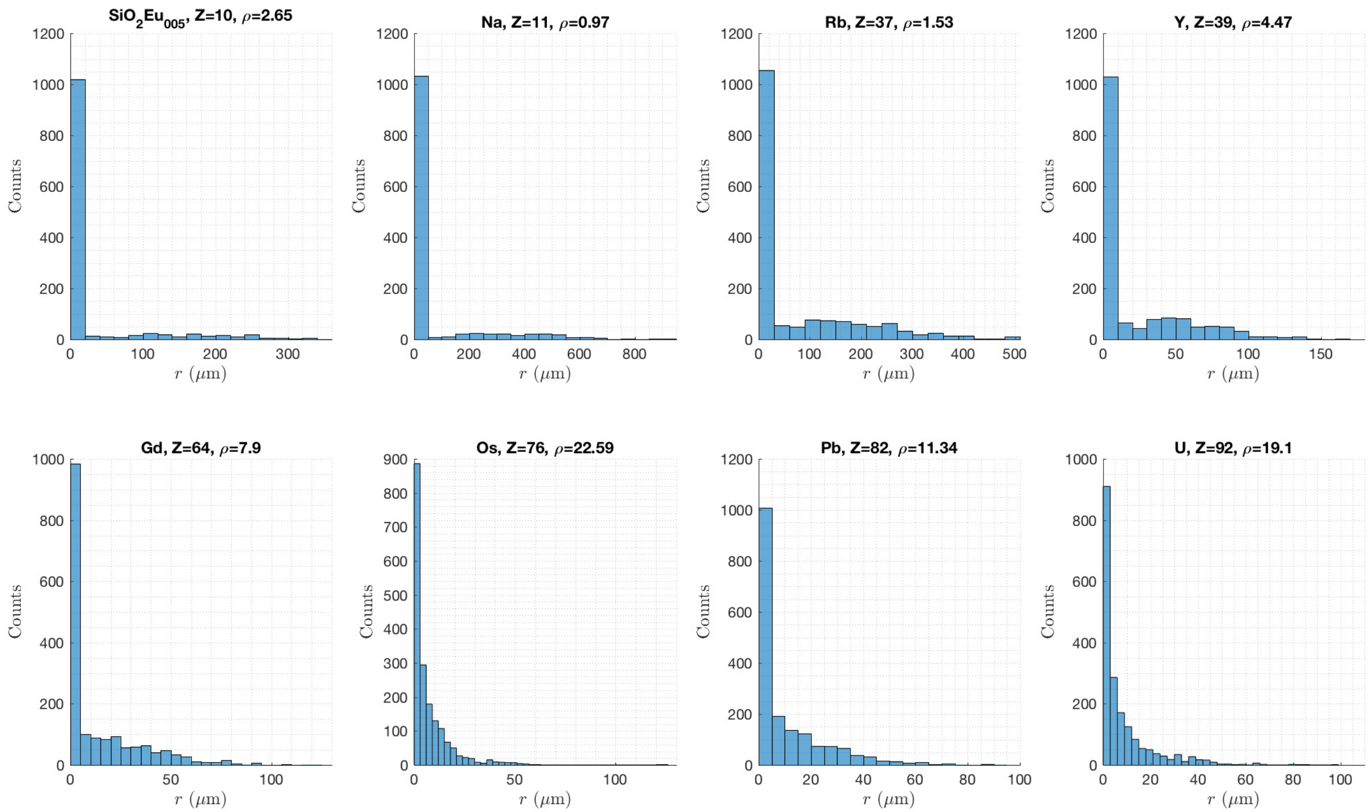

Figure C.2: The distribution of the displacement of the electrons in the xy-plane at $z = -8$ μm (scintillator-support interface) for eight different supports, based on the simulation of 1000 electrons.

C.3 Numerical aperture dependence for different scintillator thicknesses

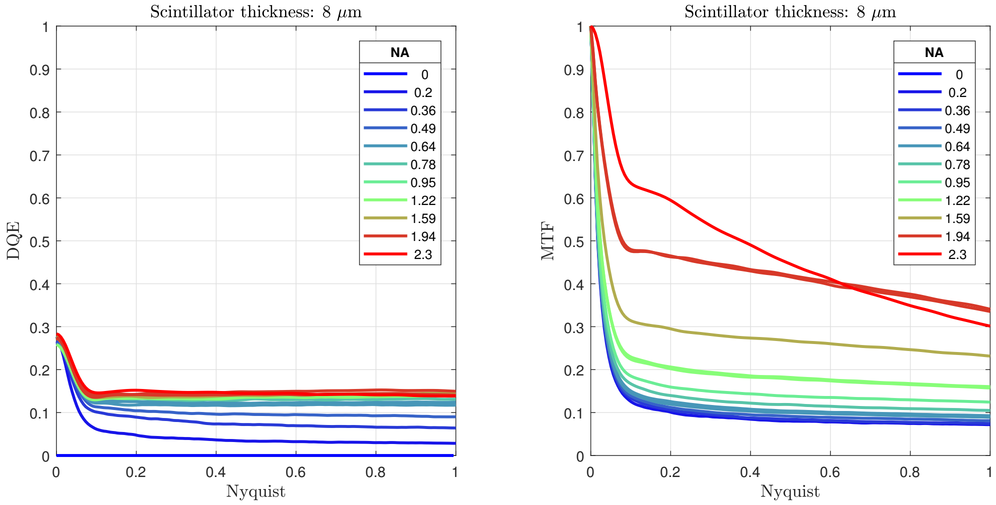

(a) DQE plot.

(b) MTF plot.

Figure C.4: DQE and MTF vs. spatial frequency in terms of Nyquist frequency. Plotted for a P43 scintillator of 8 μm thickness. SiO_2Eu_{005} support, 10^4 electrons.

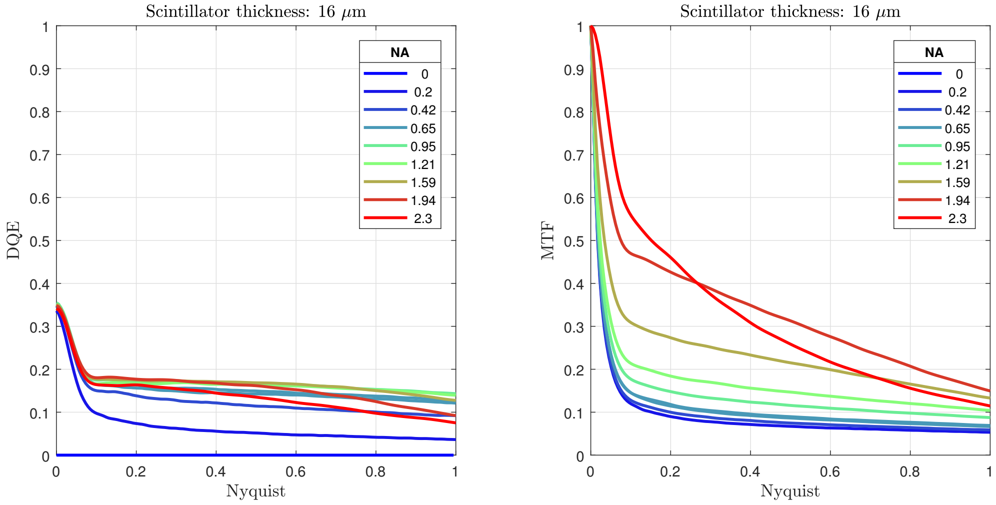

(a) DQE plot.

(b) MTF plot.

Figure C.5: DQE and MTF vs. spatial frequency in terms of Nyquist frequency. Plotted for a P43 scintillator of 16 μm thickness. SiO_2Eu_{005} support, 10^4 electrons.

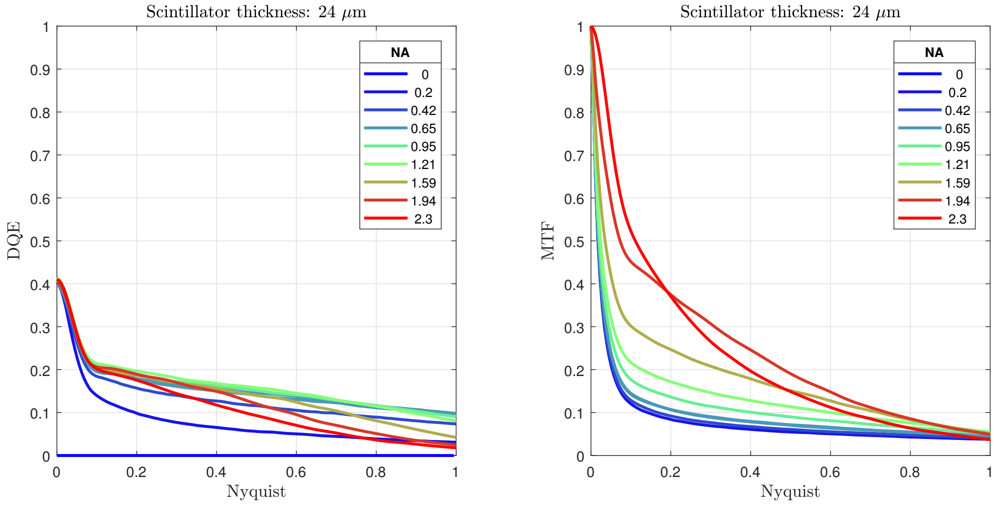

(a) DQE plot.

(b) MTF plot.

Figure C.6: DQE and MTF vs. spatial frequency in terms of Nyquist frequency. Plotted for a P43 scintillator of 24 μm thickness. SiO_2Eu_{005} support, 10^4 electrons.

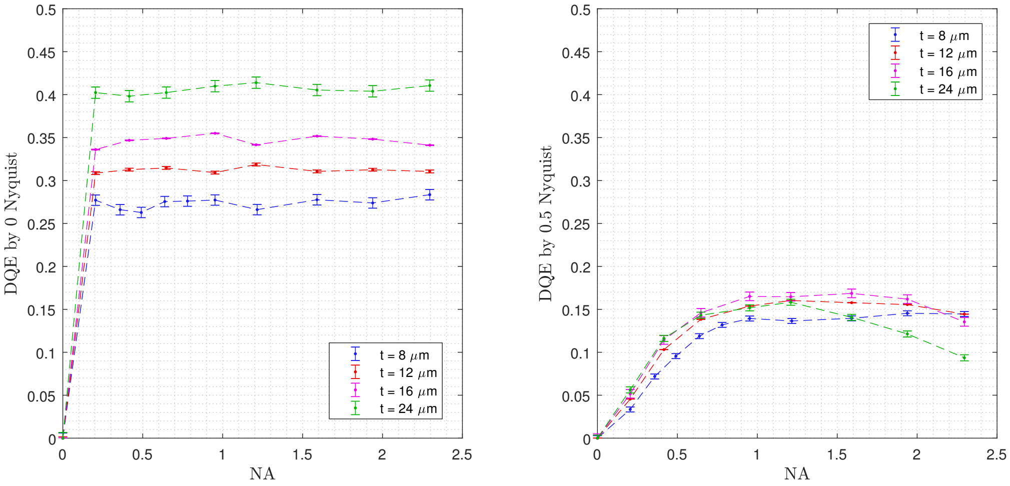

(a) DQE at zero Nyquist.

(b) DQE at half Nyquist.

Figure C.7: DQE at zero and half Nyquist vs. NA for different thicknesses of the P43 scintillator. SiO_2Eu_{005} support, 10^4 electrons.

C.4 Experimental data

C.5 EDX data

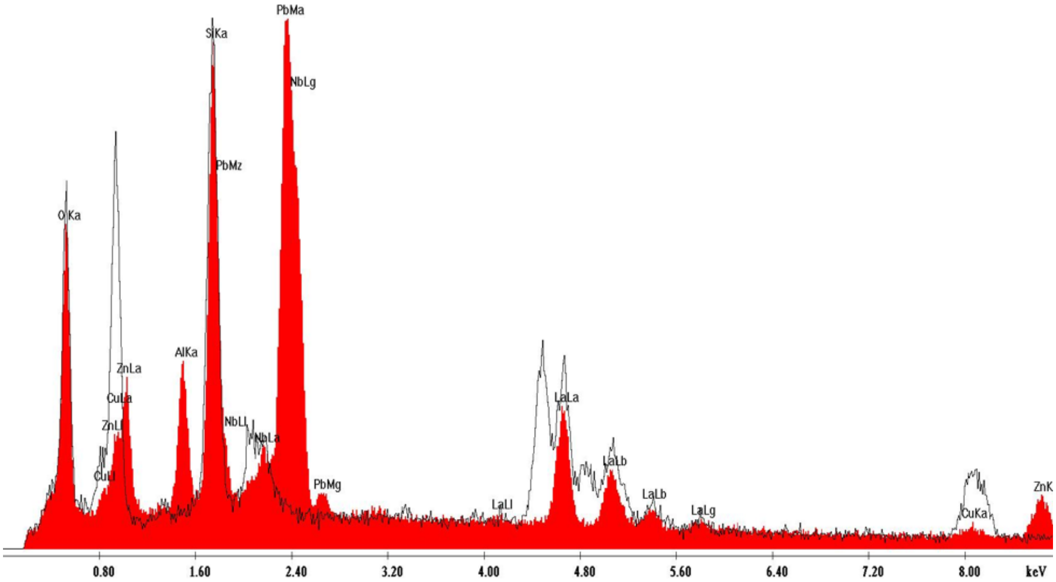

Figure C.8: EDX data for Eagle FOP with high numerical aperture.

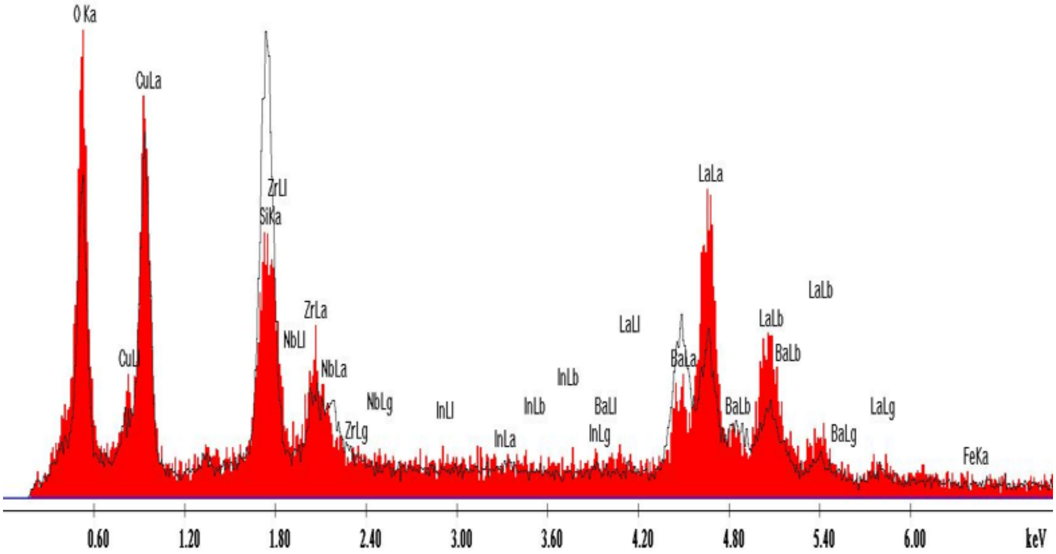

Figure C.9: EDX data for radiation hard FOP by supplier 1.

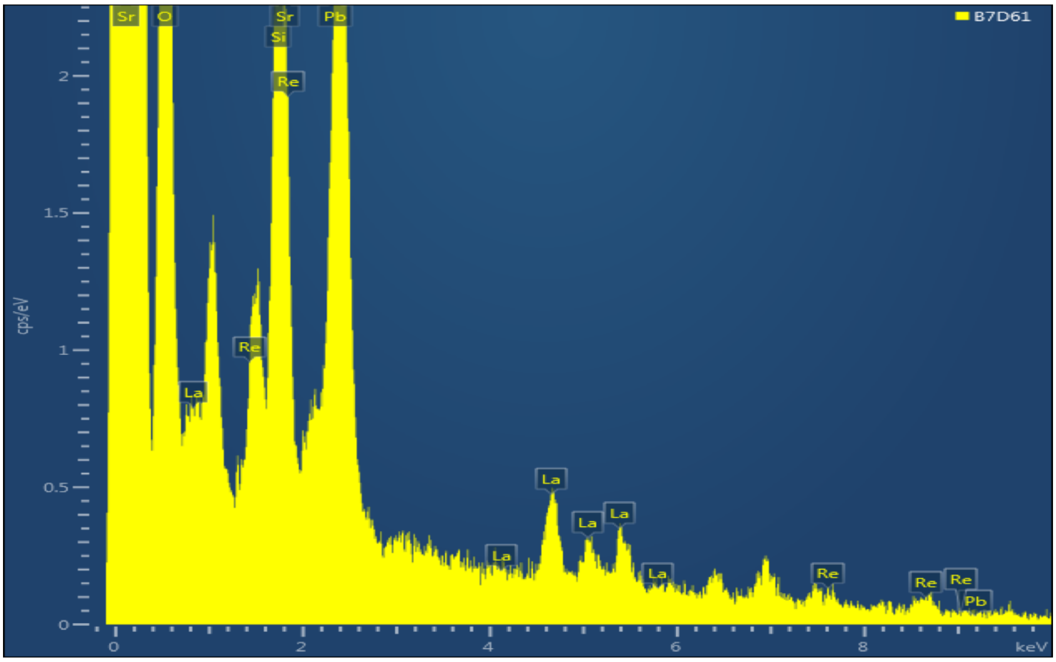

Figure C.10: EDX data for FOP by supplier 2.

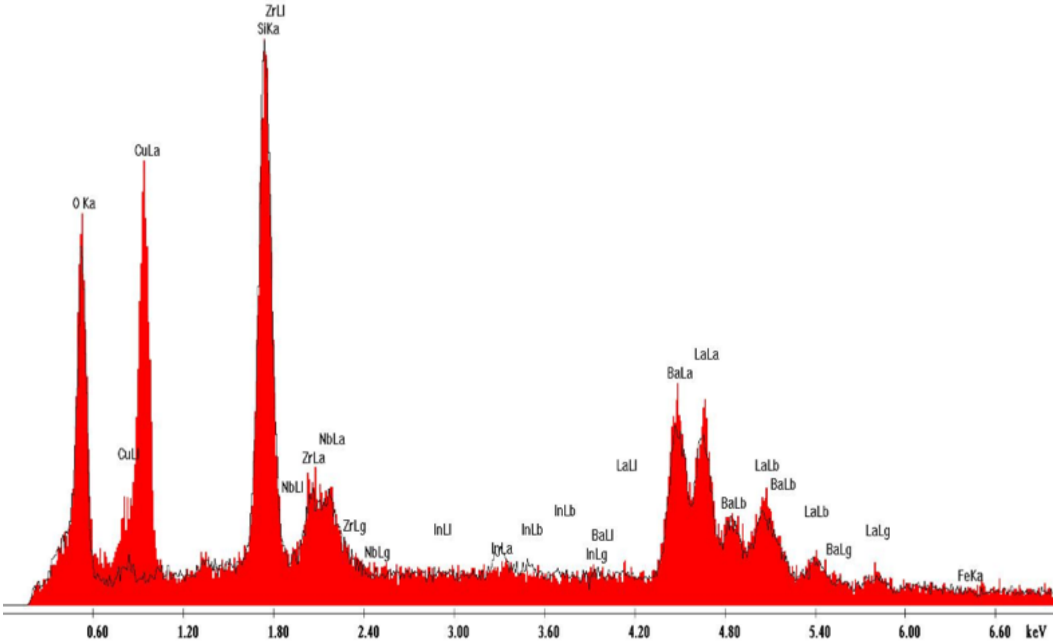

Figure C.11: EDX data of FOP by supplier 3.

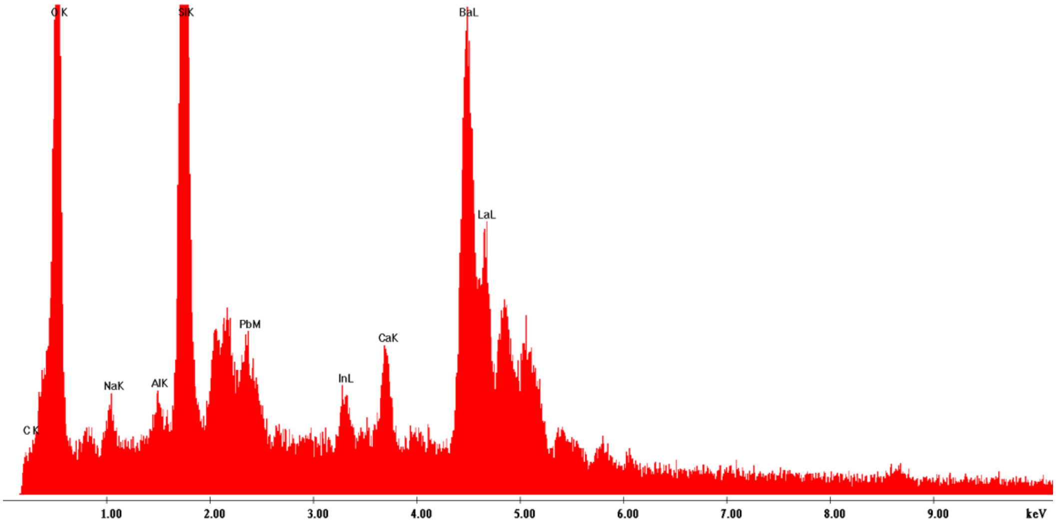

Figure C.12: EDX data of split FOP by supplier 4.

C.5.1 Experimental MTF and DQE measurements

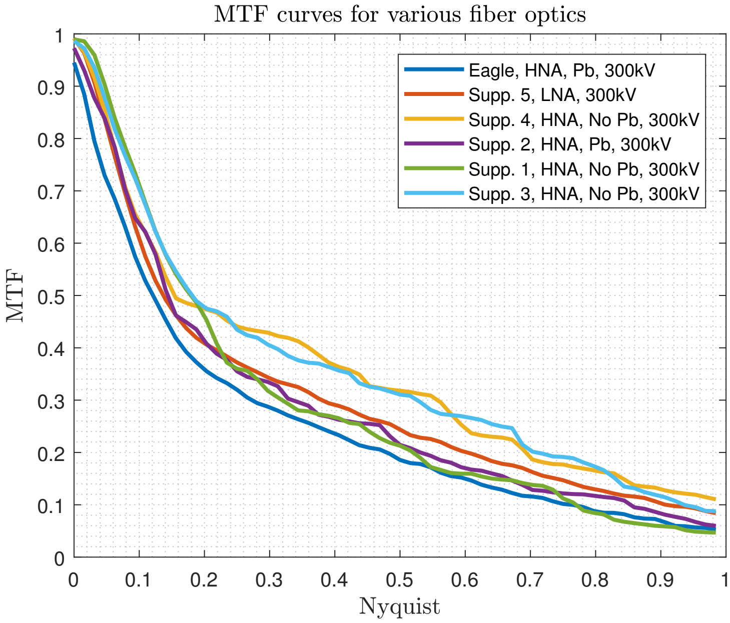

Figure C.13: MTF(u) curve of the FOP measurements at 300 keV.

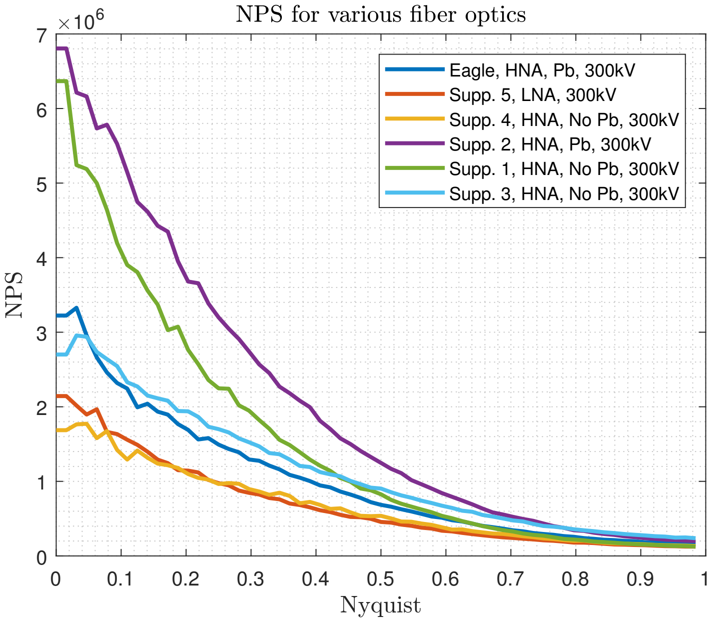

Figure C.14: NPS(u) of the FOP measurements at 300 keV.

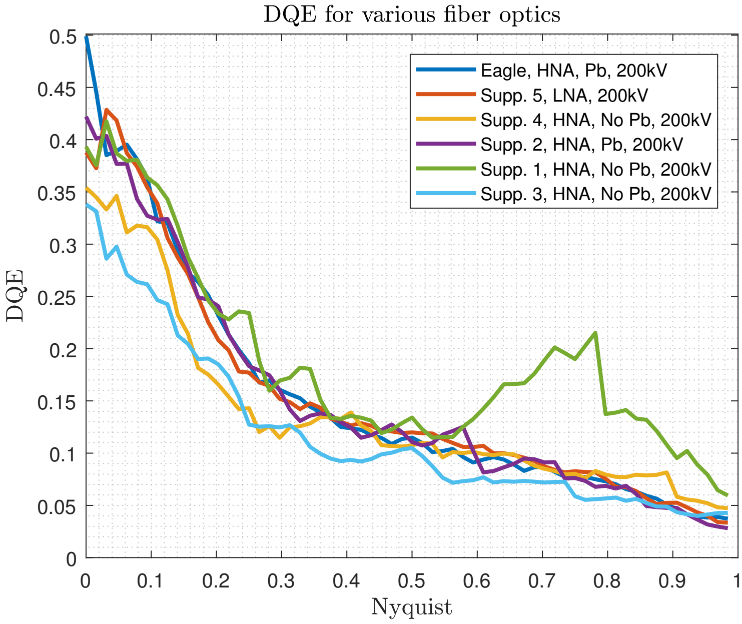

Figure C.15: DQE(u) curve of the FOP measurements at 200 keV.

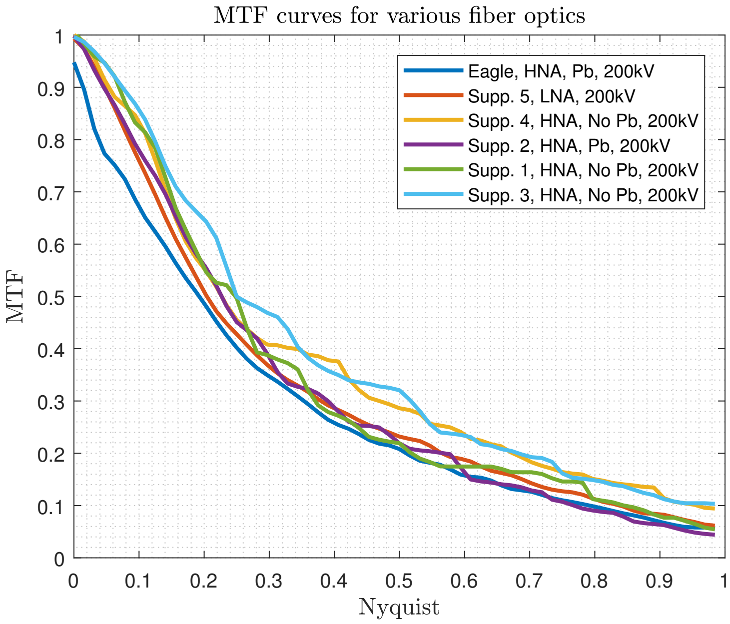

Figure C.16: MTF(u) curve of the FOP measurements at 200 keV.

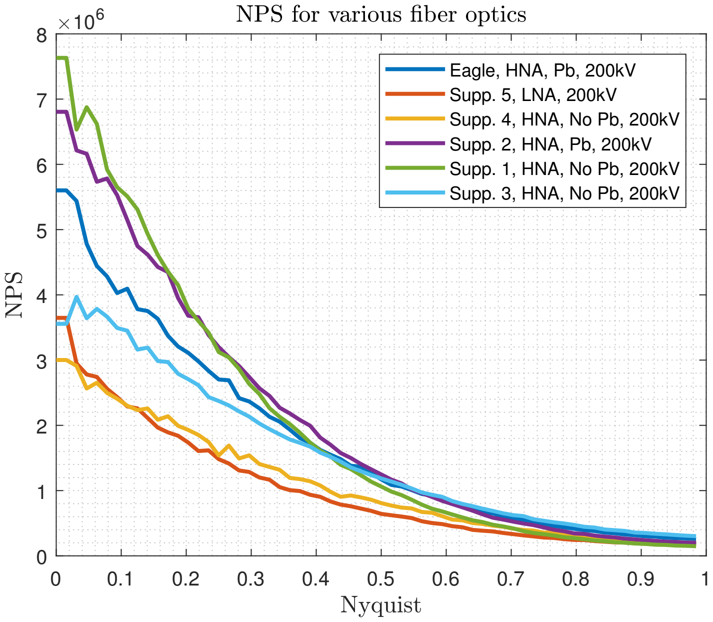

Figure C.17: NPS(u) of the FOP measurements at 200 keV.